UNIVERSITAT POLITÈCNICA DE VALÈNCIA

Department of Mechanical and Materials Engineering

Ph.D. Thesis

Study of the mechanical behavior of cortical bone microstructure by the finite element method

---

Presented by: MSc. Camila Arango Villegas

Supervised by: Dr. Eugenio Giner Maravilla

Dr. Ana Vercher Martínez

Valencia, May, 2016

Ph.D Thesis

STUDY OF THE MECHANICAL BEHAVIOR OF CORTICAL BONE MICROSTRUCTURE BY THE FINITE ELEMENT METHOD

Presented by: Msc. Camila Arango Villegas

Supervised by: Dr. Eugenio Giner Maravilla

Dr. Ana Vercher Martínez

QUALIFYING TRIBUNAL

President: Dr. _____

Vocal: Dr. _____

Secretary: Dr. _____

Valencia, May, 2016

Abstract

Cortical bone tissue is the responsible of giving support and structure to vertebrates. For that reason, understanding and analyzing its behavior is needed from each different hierarchical level that composes it. The lower the structural scale is, the greater the complexity and scarcity of studies in literature. These studies are relevant for understanding, preventing and solving important health problems that affect human beings.

From a mechanical point of view is interesting to evaluate and apply engineering numerical tools to analyze complex materials as biological tissues, increasing the state of the art in different disciplines that can be applied in numerous fields as material science, biomechanics, numerical methods, medicine and more.

In this Thesis the mechanical behavior of cortical bone at microstructural level is analyzed, with finite element models of its basic structure, the osteon. The microstructure of osteons, composed of mineralized collagen fibrils in layers with different orientations disposed concentrically around blood vessels is considered in the models for the calculation of elastic properties and failure criteria definition.

For obtaining elastic properties, the use of micromechanical finite element models is considered, with heterogeneous composition for both mineralized col-

lagen fibrils (at nanostructural level) and lamellar level (at sub-microstructural level).

The failure analysis for realistic geometries is applied after comparing different models that involve, on one hand the growth of microcracks with contact conditions and on the other, degradation of elastic material properties by user subroutines of the finite element code, the latter being the one that brings better results from a computational cost viewpoint. Therefore an interesting alternative is here presented that can be used to evaluate the damage propagation at three-dimensional level, which with other methods as X-FEM can be computationally unaffordable.

Composite materials failure criteria are applied to osteon analysis and the results are related with experimental tests from bibliography, showing the relevance of shear stresses between lamellae for failure initiation and propagation. In a two-dimensional study it is also shown the important role of osteocyte lacunae in the failure initiation, what is interesting from a cellular mechanotransduction approach.

Resumen

El tejido óseo cortical es el encargado de dar soporte y estructura a los vertebrados. Existe por tanto una necesidad de conocer y analizar mecánicamente su comportamiento desde los distintos niveles jerárquicos que lo componen, siendo mayor la complejidad y más escasos los estudios disponibles en la literatura cuanto más pequeña es la escala estructural que se analiza. Estos estudios son relevantes para comprender, prevenir y solucionar problemas de salud importantes que afectan al ser humano.

Desde el punto de vista mecánico es interesante evaluar y aplicar herramientas numéricas ingenieriles para el análisis de materiales más complejos como son los biológicos, incrementando el estado del arte en distintas disciplinas que pueden ser aplicadas en numerosos campos como la ciencia de los materiales, la biomecánica, los métodos numéricos o la medicina, entre otras.

En esta Tesis se analiza el comportamiento mecánico del hueso cortical a nivel microestructural, donde se modela mediante el método de los elementos finitos su unidad básica, la osteona. Para la obtención de las propiedades elásticas se considera en los modelos la microestructura compuesta por capas de colágeno mineralizado con diferentes orientaciones, dispuestas de manera concéntrica alrededor de los canales vasculares.

Se incluye además la utilización de modelos micromecánicos de elementos finitos que tienen en cuenta la composición heterogénea tanto para el nivel del fibrilo de colágeno mineralizado (nivel nanoestructural) como para el nivel de lamela (nivel sub microestructural).

El análisis del fallo para geometrías realistas se aplica tras comparar varios modelos que involucran por un lado el crecimiento de grietas mediante condiciones de contacto y por otro, degradación de las propiedades elásticas del material mediante subrutinas de usuario del código de elementos finitos, siendo este último el que mejores resultados presenta desde el punto de vista del coste computacional. De esta manera se presenta una alternativa interesante que permite evaluar la propagación del daño a nivel tridimensional, lo que con otros métodos como el X-FEM puede ser computacionalmente inabordable.

Se aplican criterios de fallo utilizados para materiales compuestos en ingeniería estructural a las osteonas y los resultados se relacionan con los de los ensayos experimentales disponibles en la bibliografía, mostrando la relevancia de las tensiones de cortadura entre lamelas para la iniciación y propagación del daño. En un estudio bidimensional, también se muestra la participación importante en la fase de inicio de daño de las lagunas de osteocitos lo que es interesante desde un enfoque de mecanotransducción celular.

Resum

El teixit ossi cortical és l'encarregat de donar suport i estructura als vertebrats. Existeix per tant una necessitat de conèixer i analitzar mecànicament el seu comportament des dels diferents nivells jeràrquics que ho componen, sent major la complexitat i més escassos els estudis disponibles en la literatura com més xicoteta és l'escala estructural que s'analitza. Aquests estudis són rellevants per a comprendre, prevenir i solucionar problemes de salut importants que afecten a l'ésser humà.

Des del punt de vista mecànic és interessant avaluar i aplicar eines numèriques ingenieriles per a l'anàlisi de materials més complexos com són els biològics, incrementant l'estat de l'art en diferents disciplines que poden ser aplicades en nombrosos camps com la ciència dels materials, la biomecànica, els mètodes numèrics o la medicina, entre altres.

En aquesta Tesi s'analitza el comportament mecànic de l'os cortical a nivell microestructural, on es modela mitjançant el mètode dels elements finits la seua unitat bàsica, la osteona. Per a l'obtenció de les propietats elàstiques es considera en els models la microestructura composta per capes de col·làgen mineralitzat amb diferents orientacions, disposades de manera concèntrica al voltant dels canals vasculars.

S'inclou a més la utilització de models micromecànics d'elements finits que tenen en compte la composició heterogènia tant per al nivell del fibril de col·làgen mineralitzat (nivell nanoestructural) com per al nivell de lamela (nivell submicroestructural).

L'anàlisi de la fallada per a geometries realistes s'aplica després de comparar diversos models que involucren d'una banda el creixement de clavills mitjançant condicions de contacte i per un altre, degradació de les propietats elàstiques del material mitjançant subrutines d'usuari del codi d'elements finits, sent aquest últim el que millors resultats presenta des del punt de vista del cost computacional. D'aquesta manera es presenta una alternativa interessant que permet avaluar la propagació del dany a nivell tridimensional, la qual cosa amb altres mètodes com el X-FEM pot ser computacionalment inabordable.

S'apliquen criteris de fallada utilitzats per a materials compostos en enginyeria estructural a les osteones i els resultats es relacionen amb els de els assajos experimentals disponibles en la bibliografia, mostrant la rellevància de les tensions de cisallament entre lameles per a la iniciació i propagació del dany. En un estudi bidimensional, també es mostra la participació important en la fase d'inici de dany de les llacunes d'osteòcits el que és interessant des d'un enfocament de mecanotransducción cel·lular.

Dedicated to my parents

Acknowledgments

Después de un periodo de tantos años y de tantas cosas vividas siento que mis palabras se quedarán cortas para toda la gratitud que tengo hacia todas las personas que de alguna manera me han ayudado y apoyado para terminar esta Tesis.

Empezaría por agradecer a mi director, Eugenio Giner por la orientación, enseñanzas y ayuda prestadas y por la oportunidad que me ha dado de poder trabajar en esta universidad donde he aprendido grandes lecciones tanto en el aspecto profesional como personal, que sin duda dejarán una huella imborrable para toda mi vida. Gracias también a Ana Vercher por su colaboración y su valiosa ayuda en la estimación de las propiedades elásticas de los modelos utilizados en esta tesis.

Special thanks to Dr. Himadri S. Gupta of Queen Mary University of London for the fortune that was to me to be part of your group for a few months and having so much patience with me, thank you for introducing me to the extraordinary world of X-Ray synchrotron that without any doubt has been one of the most important experiences of my life.

Gracias a Fabio M. Peña de la Universidad Autónoma de Manizales por haberme introducido con su sabiduría al mundo de los elementos finitos y de la investigación científica y darme la fuerza inicial para hacer este doctorado, eres un gran ejemplo para mí y siempre estaré agradecida contigo.

A todos mis compañeros de departamento y del aula de becarios durante tantos años y a los más cercanos: Santi G., José Manuel N., Luca G., Xavi, Onofre M., Carla

G., Andrés R., Mabel T., Enrique N., Octavio A., Jose M., Javi C., Eva V., Angels. A Eva Sánchez, por tantas cosas compartidas, apoyo y ánimos en tantos momentos y a Estivaliz L. porque además del apoyo moral me ayudaste con mucha paciencia a solucionar serios problemas con Abaqus. A Ricardo B. gracias por su colaboración en el Capítulo 7 de esta Tesis. A Marga V. mil gracias por ser tan especial, tu apoyo ha sido muy importante para terminar esta tesis, te admiro profesional y personalmente; a Fede O. por tu paciencia y valiosísima ayuda durante todo este tiempo y gigas de trabajo. Me gustaría también mencionar a Antoine A. porque aunque compartimos muy poco tiempo fue suficiente para dejarme el recuerdo de una persona magnífica que nunca olvidaré.

En general tendré siempre mucha gratitud y el mejor recuerdo de la Universidad Politécnica de Valencia, del Centro de Investigación en Ingeniería Mecánica y de Javier Fuenmayor que sin duda es un hombre ejemplar y una suerte para mí haberlo conocido.

A mi familia adoptiva de Valencia por ser uno de los regalos más bonitos de mi vida, por darme la fuerza que algunas veces tanto he necesitado y por muchos momentos verdaderamente inolvidables: Mónica G., Maka, Chiara P., Carlos O., Enrique de R., Angelika F., George B., Rafa y Miyu. A Sabela R., Sofía M., Ismael S., Pablo G., Pepa L. y Conxa M. por tantas cosas compartidas, por ser mis hermanos para toda la vida, los amo.

A mis amigos de Colombia que siguen acompañándome a pesar de la distancia, especialmente a Leidy Z. por acompañarme siempre e incondicionalmente y ser mi apoyo por tantos años, te quiero mucho. A Javier A. por su valiosa compañía durante tanto tiempo.

Por último pero no menos importante, a mi familia en Colombia por darme todo el apoyo que he necesitado siempre y a mis papás por ser la luz que está siempre en mi camino; a mis hermanos, cuñados y sobrinos que siempre han estado presentes en cada cosa que hago y cada logro que obtengo es realmente su logro. Gracias a mi mamá por enseñarme a soportar de la mejor manera la distancia, a Yoyo por apoyarme siempre en todo de una manera tan incondicional, a mis sobrinos por existir y por darme cada vez nuevas razones para ver la vida de una mejor manera.

Moltes gràcies.

Contents

Chapter 1

Introduction

"If bone is the answer, then what is the question?"
Rik Huiskes

1.1 Introduction and aim

The study of bones has a great importance on scientific investigation. In the past two decades the quantity of people involved and contributions to literature have exponentially increased achieving important discoveries with a high social impact. Although because of its complexity at multiple approaches, there are many fields in which more insight and knowledge is still necessary to understand its behavior.

Nowadays, the diagnostic, prediction and risk control of bone fracture have a socioeconomic and life quality impact, especially taking into account important diseases as osteoporosis. Additionally, it has been proved that diagnostic tests exclusively based on bone mineral density (BMD) (the most common at present) are not enough in order to characterize the risk of fracture. That is why recently less simplistic indicators

based on other factors as bone structure morphology and some mechanical properties as elastic modulus at microstructural level have been suggested.

Therefore the aim of this Thesis is the development of numerical models to predict the elastic properties and the progressive failure of cortical bone tissue by the finite element method in order to find an equilibrium between the computational cost and the obtained failure simulation.

The micromechanical models developed in this Thesis have into consideration two principal aspects: on one hand the microstructural characteristics that define cortical tissue (spatial distribution, elastic properties, morphology, etc.) and on the other, the simulation of damage propagation through property degradation of the tissue under mechanical loads. The presence of microcracks and lacunae it is also simulated by using advanced finite element techniques. These models enable the reproduction with higher accuracy of the elastic and strength behaviors for this kind of tissues and characterize the mechanical microstructural response.

1.2 Organization of the Thesis

The main structure of this Thesis consists of nine chapters. The first five chapters correspond to: first, the introduction and description of the experimental tests found in the literature that motivated this work and second the calculation and description of the material properties used in the numerical models presented in the final chapters.

Chapter 2 contains an introduction to microstructural composition of bones and description of the hierarchical levels considered in this Thesis.

Chapter 3 is about a numerical homogenization developed with the finite element method for the calculation of the elastic properties at sub-microstructural level as well as the properties used for micro-structural models. The relevance and implication of these resultant properties for the fulfilment of thermodynamic restrictions is also analyzed.

In Chapter 4 the strength properties used in the FE models are described. These are obtained both from literature and from proposed relationships of fracture mechanics for not reported data.

Chapter 5 is an introduction to finite element analysis applied to cortical bone failure. Also a damage background is presented; some relevant works of the state of the art for this Thesis are referred from literature and finally there is an explanation of dominant failure criteria used for the analysis of a single osteon.

In Chapters 6, 7 and 8 the 2D and 3D respectively computationally efficient finite element models with failure implementation through damage propagation of cortical bone are detailed aiming at reducing the computational cost of an explicit crack model. The 2D models of Chapter 6 include geometries from half a single osteon with circumferential shape and lacunae to more realistic geometry models based on micrographs from literature. A three point bending load case of ovine bone is simulated and the correspondent mechanical tests performed in the context of this Thesis are described in Chapter 7.

In Chapter 8 models with a more detailed geometry are analyzed and the resulting damage patterns are compared with epi-fluorescence micrographs available in bibliography. The conclusions of the Thesis are presented in Chapter 9.

Chapter 2

Introduction to hierarchical levels of bone

The skeletal system is very important for vertebrate bodies both metabolically and biomechanically (Cowin [2001]). It is composed of individual bones and the tissues that connect them. Bones are the principal constituents of the system differing from the rest of tissues in stiffness and hardness. These characteristics are derived from constituents as inorganic salts that mineralize a collagen fibril matrix and multiple non collagenous proteins. The stiffness and hardness of bones permits skeleton to keep its shape, protecting smooth tissues in craniums, thorax and pelvic cavities. It also gives protection to bone marrow and transmits forces from muscular contraction from one part of the body to others during movement. The mineral content works as ion supply, particularly of calcium that in addition of being fundamental to bone structure, allows the contraction of muscles as the heart.

One of the particularities and exceptional characteristics of bone is that it can regenerate itself, reshaping and adapting its mass and properties to changes and mechanic requirements from bodies. The bone structure even at its global level is very complex and it can be considered as a composite from many hierarchical levels (Cowin [2001]; Rho *et al.* [1998]; Taylor *et al.* [2007]). In order to understand the mechanical prop-

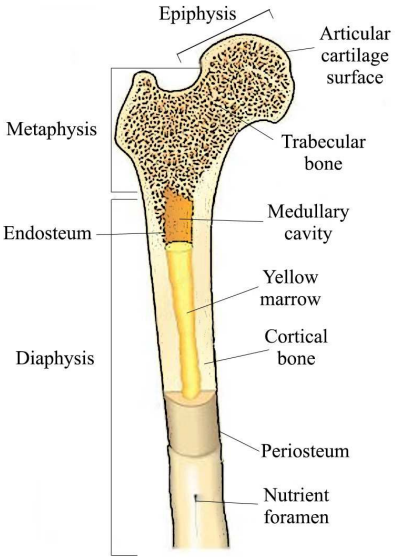

Figure 2.1: Long bone structure.

erties of bone tissues it is important to recognize each of its phases, also knowing the mechanical properties of its constituents, leading to the complexity of its study.

In the next sections the fundamental composition of cortical bone from macroscopic to microstructural level (the context of this Thesis) is described.

2.1 Macrostructural level

Among different types of bone, long bones are responsible of weight support during activities giving structure and mobility. A typical adult long bone structure (Fig. 2.1) consists of a cylindrical axis in the middle, called diaphysis and two rounded extremes called epiphysis. Connecting these two parts is the metaphysis. The extremes of long bones are covered by articular cartilage.

Bones are composed of two principal types of tissues: cortical (compact) bone and trabecular (porous) or cancellous bone (Fig. 2.1). The diaphysis is composed principally of cortical bone that protects the bone marrow, the epiphysis and metaphysis are composed of both cortical and trabecular tissues. The percentage of each one of these parts depends on the function of the bone although approximately 80% of adult skeleton mass corresponds to cortical bone that constitute the external walls of bones. The cortical bone shell can reach a thickness between several tenths of a millimeter (in vertebrae) and several millimeters (in the mid-shaft of long bones) (Launey *et al.* [2010]) and it is responsible of protection and support. Trabecular bone is more vascularized and contains the red bone marrow where hematopoiesis (blood cell production) is generated.

2.2 Microstructural level (10-500 μm)

When bone begins to be formed, its first structure is formed by concentric fibers with low mineral content. This structure is called primary osteon. The osteon is the basic structural unity of cortical bone (Fig. 2.2). When this process of formation and mineralization ends, there is a need of adapting to the mechanical demands changing the shape and configuration when it is needed. That is achieved by new concentric structures overlapping the original tissue, called secondary osteons.

Secondary osteons are composed of layers called lamellae with thicknesses between 3-7 μm (Cowin [2001]; Rho *et al.* [1998]) that are arranged concentrically around blood vessels canals, called Haversian canals, that is the reason this level is also called Haversian system. The final structure is close to a cylindrical shape with diameter between 100-300 μm.

2.3 Sub-microstructural level (1-10 μm)

The sub-microstructural level begins at lamellae composed by arrays of mineralized collagen fibrils specifically oriented, being this orientation different from subsequent adjacent sublayers (Akiva *et al.* [1998]) as shown in Fig. 2.3. The orientations of

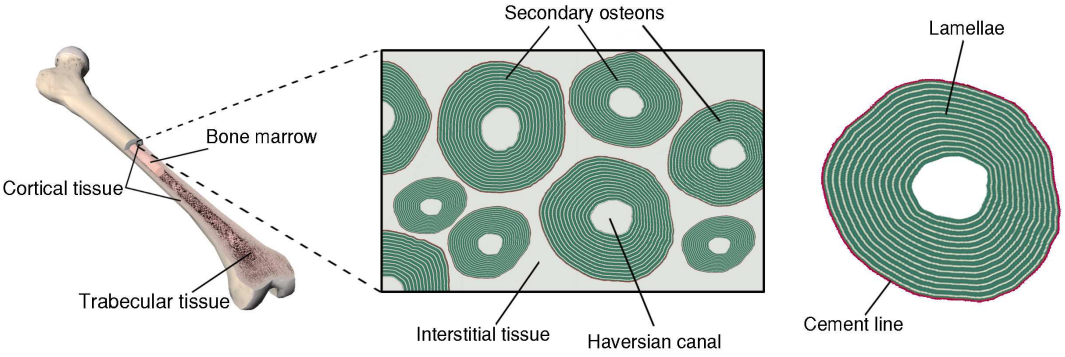

Figure 2.2: From left to right different scales of long bones. Left: bone at macroscale composed of cortical and trabecular tissues. Middle: microscale of a transversal section of cortical bone, composed of osteons and interstitial tissue. Right: an osteon composed of concentric lamellae and surrounded by a cement line.

these arrays differ in each sublayer, in such a way that a complex rotated plywood-like structure is formed (Weiner *et al.* [1999]).

Between osteon lamellae, there are the so-called osteocyte lacunae, where important cells (osteocytes) in the remodeling process of bone (Cowin [2001]) are located. Numerous works have proved the important role of osteocytes (Cowin [2001]; Cowin *et al.* [1991]; Klein-Nulend *et al.* [2012]; Cox *et al.* [2011]) relating cellular biology with fracture mechanics focused on the networking between cells acting as sensors and starters of bone remodeling.

2.4 Nanostructural and sub-nanostructural levels (less than 1μm)

At nanostructural level, bone is composed of fibers where mineralized collagen fibrils (Fig. 2.3) are grouped. Type-I mineralized collagen fibrils are the building blocks of the lamellae and are composed of tropocollagen molecules and hydroxyapatite minerals periodically arranged. It is well known that the collagen fibril orientation

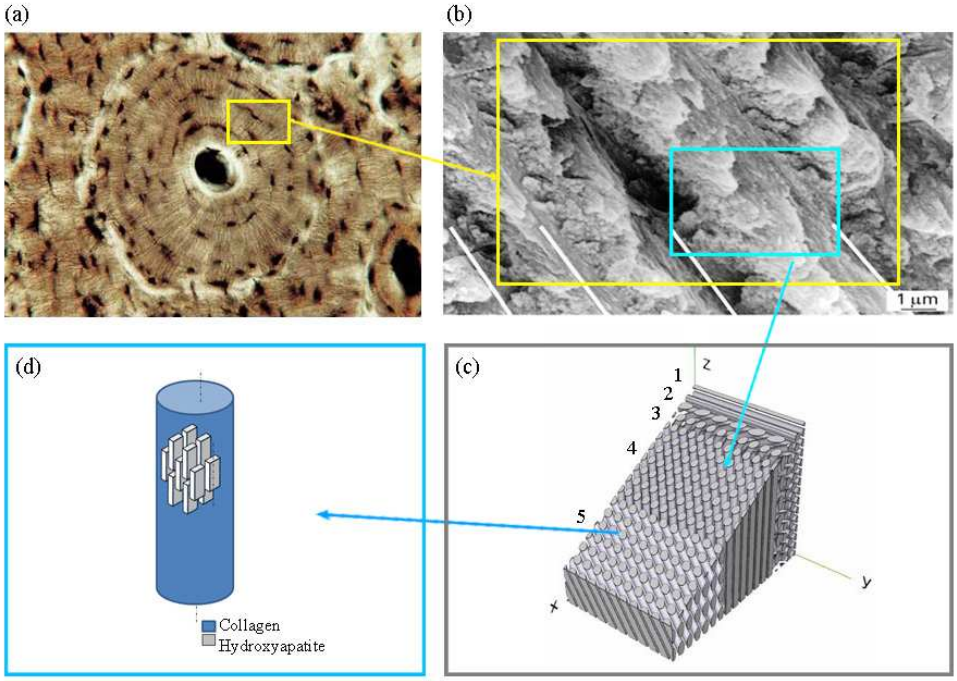

Figure 2.3: (a) Micrograph of an osteon, (b) sub-microstructural level (lamellae and sublayer variations are observable between white lines) (Wagner and Weiner [1992]), (c) lamellar fibrils structure scheme and different sublayer numeration according to Weiner *et al.* [1999], (d) mineralized collagen fibril structure scheme (Vercher *et al.* [2014]).

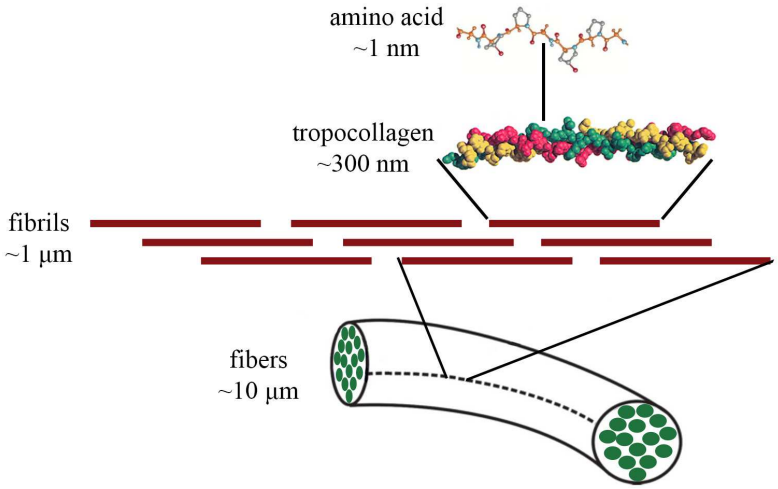

Figure 2.4: Schematic view of some of the hierarchical features of collagen, ranging from the amino acid sequence level at nanoscale up to the scale of collagen fibers with lengths on the order of 10 μm.

pattern in the lamella is an important feature because mechanical properties depend on bone structure at the very small scale.

At a molecular scale, collagen type I (Fig. 2.4) and carbonate apatite crystals are the basic constituents of mineralized collagen fibrils. The mineral is largely impure hydroxyapatite $Ca_{10}(PO_4)_6(OH)_2$ containing constituents such as carbonate, citrate, magnesium, fluoride, and strontium incorporated into the crystal lattice or absorbed onto the crystal surface (Cowin [2001]). The organic matrix consists of 90% collagen and about 10% of various non-collagenous proteins (Cowin [2001]). Each fibril is made up of three polypeptide chains about 1000 amino acids long. These are wound together in a triple helix. A triple-helical molecule is thus cylindrically shaped, with an average diameter of about 1.5 nm, and lengths of 300 nm (Weiner and Wagner [1998]).

The orientation of collagen fibrils varies in successive layers. Reisinger *et al.* [2011] developed a detailed analysis of elastic properties of the microstructure using a finite element model in which the elastic constants of lamellar bone have been calculated using homogenization theories from a previous work (Reisinger *et al.* [2010]). Because of the complexity of bone at small scales these models are developed in order to

understand the mechanical behavior and that is the reason why these authors analyze several collagen fibril orientation patterns. They conclude that the model proposed by Weiner *et al.* [1999], based on a 5-layered structure in an individual lamella (Fig. 2.3), is in good agreement with experimental results. Therefore this model is taken as a reference in this Thesis.

Chapter 3

Elastic properties of cortical bone

3.1 Introduction

The lamellar configuration of bone has always been a controversial topic, and various models have been proposed for the structure of bone lamellae. In the last decade of 17th century, Clopton Havers was a pioneer anatomist and one of the most notable histologists of all time who first described what we now call the Haversian canals. Gebhardt [1905] was the first to suggest that all lamellae are dense fibrous layers in which collagen fibers lie parallel; the difference between successive lamellae consists solely in the orientation of the fibrils, which may vary through an angle of 0–90°. In all other models subsequently proposed, the lamellar pattern of the bone is assumed to depend on the alternation of layers of heterogeneous structure. Later, Ascenzi and Bonucci [1967, 1968] held the idea of a unidirectional collagen fibril orientation in each lamella, basing their results on polarized light microscopy (PLM) of secondary osteons. Subsequently, Wagner and Weiner [1992] also suggested a unidirectional fibril orientation in each lamella. These authors calculated elastic constants of an

individual lamella by using several composite material models (Padawer and Beecher [1970]; Lusis *et al.* [1973]; Halpin [1992]).

Regarding microstructural and nanostructural levels, Zysset *et al.* [1999] propose a nanoindentation technique to quantify the elastic properties of lamellar bone and compared these properties between osteonal, interstitial and trabecular microstructures from the diaphysis and the neck of the human femur. Rho *et al.* [1998] present a literature review of the mechanical properties of bone with an emphasis on the relationship between the complexity of the hierarchical structure and its mechanical properties, highlighting that an accurate model should include the molecular interactions or physical mechanisms involved in the transfer of load across the bone material subunits, which makes the rule of mixtures a moderately successful formulation.

Although the vast majority of authors in bibliography support the idea of lamellar structure with the alternation of fibrils at different directions inside lamellae, Marotti *et al*. have remarkable works based on scanning electron microscopy (SEM) where a different model that is not in agreement with that assumption is proposed. In their works, lamellar bone is proposed as an alternation of dense-acellular lamellae (collagen rich) and loose-cellular lamellae (collagen poor), all exhibiting an interwoven texture of collagen fibers (Marotti and Muglia [1994]; Marotti *et al.* [2013]).

It seems that the first investigators who analyzed a lamella as a two-phase composite material were Currey [1962] and Bonfield and Li [1967]. More recent investigations consider a lamella as a layered structure where a collagen fibril orientation pattern exists (Weiner *et al.* [1999]; Akiva *et al.* [1998]; Giraud-Guille [1988]; Wagermaier *et al.* [2006]). The bibliography about elastic properties of platelet or ribbon reinforced composites is scarce. According to Halpin [1992], the following equations are used to calculate certain elastic constants:

$$\frac{\overline{p}}{p_m} = \frac{(1 + \zeta\eta V_f)}{(1 - \eta V_f)} \tag{3.1}$$

$$\eta = \frac{(p_f/p_m - 1)}{(p_f/p_m + \zeta)} \tag{3.2}$$

where:
$\overline{p}$: composite properties E_{11}, E_{22}, G_{12}, G_{23}, ν_{12}, ν_{23}
p_f: reinforcement properties E_f, G_f, ν_f
p_m: matrix properties E_m, G_m, ν_m
V_f: reinforcement volume fraction
ζ: constant that is a function of reinforcement geometry, packing and loading conditions.

1, 2, 3 subscripts are the directions of the reference local system as shown in Fig. 3.1. The volume fraction of the reinforcement platelet V_f is given by:

$$V_f = \frac{LWT}{(L + d_L)(W + d_W)(T + d_T)} \tag{3.3}$$

where L is the platelet longitude, W is the width and T is the thickness. d_L, d_W and d_T are the distances between platelets: longitudinal, transversal on plane and transversal out of plane, respectively as shown in Figs. 3.1 and 3.12.

The factor ζ can be considered as a reinforcement measure that is function of boundary conditions. In Halpin [1984], the following expressions for calculating ζ for different elastic properties are proposed:

$$\zeta_{E_{11}} = 2(L/T) + 40V_f^{10} \tag{3.4}$$

$$\zeta_{E_{22}} = 2(W/T) + 40V_f^{10} \tag{3.5}$$

$$\zeta_{G_{12}} = ((L + T)/2T)^{\sqrt{3}} + 40V_f^{10} \tag{3.6}$$

$$\zeta_{G_{23}} = \frac{1}{4 - 3\nu_m} \tag{3.7}$$

$$\zeta_{\nu_{12}} = \infty \tag{3.8}$$

$$\zeta_{\nu_{23}} = 0 \tag{3.9}$$

From Eq. 3.1 we can obtain the following properties: E_{11}/E_m, E_{22}/E_m, G_{12}/G_m, G_{23}/G_m, ν_{12}/ν_m and ν_{23}/ν_m. However we cannot obtain expressions to calculate: ζ for out of plane Young's modulus, E_{33}, shearing modulus, G_{31}, or Poisson's ratio ν_{31}. Therefore according to Akiva *et al.* [1998] in this work we assume that $\zeta_{E_{33}} = 2T/(L+W)$, $\zeta_{G_{31}} = \zeta_{G_{23}}$ and $\zeta_{\nu_{31}} = \zeta_{\nu_{23}}$.

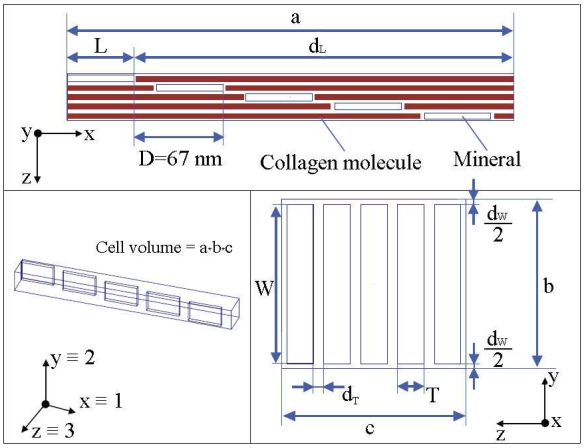

Figure 3.1: Unit cell volume $a \times b \times c$ and principal dimensions of the domain (in each view, proportions are preserved).

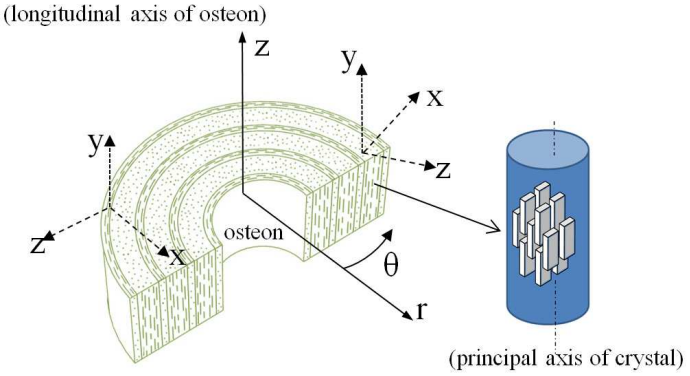

Figure 3.2: Cylindrical coordinate system (r, θ, z) is used as a global coordinate system, and a local auxiliary coordinate system (x, y, z) is defined at any point, being (x, y, z) coincident with (θ, z, r), respectively.

On the other hand, the elastic compliance matrix for an orthotropic material, $\mathbf{S}^l$ is given by:

$$\mathbf{S}^l = \begin{pmatrix} \frac{1}{E_{11}} & \frac{-\nu_{21}}{E_{22}} & \frac{-\nu_{31}}{E_{33}} & 0 & 0 & 0 \\ \frac{-\nu_{12}}{E_{11}} & \frac{1}{E_{22}} & \frac{-\nu_{32}}{E_{33}} & 0 & 0 & 0 \\ \frac{-\nu_{13}}{E_{11}} & \frac{-\nu_{23}}{E_{22}} & \frac{1}{E_{33}} & 0 & 0 & 0 \\ 0 & 0 & 0 & \frac{1}{G_{23}} & 0 & 0 \\ 0 & 0 & 0 & 0 & \frac{1}{G_{31}} & 0 \\ 0 & 0 & 0 & 0 & 0 & \frac{1}{G_{12}} \end{pmatrix} \tag{3.10}$$

where superindex l makes reference to the local coordinate system (1,2,3), see Fig. 3.1, where $\mathbf{C}^l = (\mathbf{S}^l)^{-1}$ is the orthotropic stiffness matrix. In Eq. 3.10 the nine independent elastic constants of the material can be calculated with Halpin-Tsai equations described above. Therefore it is posible to characterize the elastic behaviour of the fibril if it is considered as an orthotropic material. More recent studies of the configuration of crystals inside fibrils show an anisotropic behavior. That is why the objective of next sections of this Thesis is to obtain the constitutive matrix of the fibril by a FE model using homogenization procedures.

3.1.1 Lekhnitskii transformation

The following equation corresponds to the mineralized collagen fibril compliance matrix. It is expressed in the local coordinate system (x, y, z) that is directly related with the global cylindrical system (θ,z,r) (see Fig. 3.2):

$$\mathbf{S}^g = \mathbf{q}^T \mathbf{S}^l \mathbf{q} \tag{3.11}$$

where $\mathbf{q}$ is the transformation matrix corresponding to Lekhnitskii equations (Lekhnitskii [1963]):

$$\mathbf{q} = \begin{pmatrix} \alpha_1^2 & \alpha_2^2 & \alpha_1^3 & -2\alpha_2\alpha_3 & -2\alpha_3\alpha_1 & -2\alpha_1\alpha_2 \\ \beta_1^2 & \beta_2^2 & \beta_1^3 & -2\beta_2\beta_3 & -2\beta_3\beta_1 & -2\beta_1\beta_2 \\ \gamma_1^2 & \gamma_2^2 & \gamma_1^3 & -2\gamma_2\gamma_3 & -2\gamma_3\gamma_1 & -2\gamma_1\gamma_2 \\ -\beta_1\gamma_1 & -\beta_2\gamma_2 & -\beta_3\gamma_3 & \beta_2\gamma_3+\beta_3\gamma_2 & \beta_1\gamma_3+\beta_3\gamma_1 & \beta_1\gamma_2+\beta_2\gamma_1 \\ -\gamma_1\alpha_1 & -\gamma_2\alpha_2 & -\gamma_3\alpha_3 & \gamma_2\alpha_3+\gamma_3\alpha_2 & \gamma_1\alpha_3+\gamma_3\alpha_1 & \gamma_1\alpha_2+\gamma_2\alpha_1 \\ -\alpha_1\beta_1 & -\alpha_2\beta_2 & -\alpha_3\beta_3 & \alpha_2\beta_3+\alpha_3\beta_2 & \alpha_1\beta_3+\alpha_3\beta_1 & \alpha_1\beta_2+\alpha_2\beta_1 \end{pmatrix} \tag{3.12}$$

where α_i, β_i and γ_i are the director cosines that relate the auxiliary local system of coordinates (x, y, z) with respect to the local oriented system (1,2,3).

In this Thesis and past publications of the research group (Vercher *et al.* [2014]; Vercher-Martínez *et al.* [2015]; Giner *et al.* [2014]), the fibril orientation pattern proposed by Weiner *et al.* [1999] is considered. These authors base their study on several TEM and SEM micrographies concluding that a lamellar unit is an asymmetric structure formed by five sublayers in which fibrils change their orientation. These authors infer from several studies that the variation of the sublayer thickness is directly related to the strength capabilities of the bone.

In this chapter the different hierarchical level definition of elastic properties is described. First, the unitary cell of a mineralized collagen fibril with staggered configuration of crystals inside the matrix. Second, followed by the next lamellar level that is composed of arrays of mineralized collagen fibrils. Finally the osteon composed of lamellae grouped into two types and surrounded by cement lines and interstitial tissue.

3.1.2 Unitary cell of a composite material

In order to characterize an heterogeneous material, a unitary cell model can be used (Suquet [1987]; Hohe [2003]; Pahr and Zysset [2007]). If periodic boundary conditions are considered, the response of the unit cell will be representative of the whole structure. Following Reisinger *et al.* [2011], periodic boundary conditions must fulfill two conditions: the stress field must be periodic, $\sigma_{ij}^{+} = \sigma_{ij}^{-}$ (see Fig. 3.3 for the nomenclature of representative volume element faces), and the shapes of opposite sides of the unit cell must be identical allowing strain-periodic displacement field. Six independent unitary strain fields are applied in order to obtain the corresponding column i of the stiffness matrix, $\mathbf{C}_{*i}$.

The Lamé–Hooke constitutive equation, is given by:

$$\sigma = \mathbf{C} \cdot \epsilon \tag{3.13}$$

where $\sigma = (\sigma_{xx}\ \sigma_{yy}\ \sigma_{zz}\ \tau_{yz}\ \tau_{zx}\ \tau_{xy})^{\mathrm{T}}$ is the stress vector, C is the stiffness matrix and $\epsilon = (\epsilon_{xx}\ \epsilon_{yy}\ \epsilon_{zz}\ \gamma_{yz}\ \gamma_{zx}\ \gamma_{xy})^{\mathrm{T}}$ is the strain vector imposed, i.e.:

Load case 1: $\epsilon^1 = (1\ 0\ 0\ 0\ 0\ 0)^{\mathrm{T}}$, then $\mathbf{C}_{*1} = \sigma^1$.

Load case 2: $\epsilon^2 = (0\ 1\ 0\ 0\ 0\ 0)^{\mathrm{T}}$, then $\mathbf{C}_{*2} = \sigma^2$.

...

Load case 6: $\epsilon^6 = (0\ 0\ 0\ 0\ 0\ 1)^{\mathrm{T}}$, then $\mathbf{C}_{*6} = \sigma^6$.

where σ^i is the equilibrium stress vector corresponding to the strain field ϵ^i. Stress components are obtained from the finite element model.

Periodic boundary conditions have to be applied in order to ensure that the analyzed hexahedron is a representative volume of the entire domain and displacement gradients along the corresponding external surface must be equal. In this work, equations proposed by Hohe [2003] are used. In addition, it is necessary to fully constrain the model to avoid rigid solid motions and, therefore, the central node of the finite

element model is constrained. The 3D finite element model was made with hexahedral elements and the constraint equations were applied in the commercial code Ansys by the command `Constraint Equation`.

The three-dimensional periodicity of the volume implies the following relationships:

$$u^{1+} = u^{1-} + a\epsilon_1^i \tag{3.14}$$
$$v^{1+} = v^{1-} + \frac{1}{2}a\epsilon_6^i \tag{3.15}$$
$$w^{1+} = w^{1-} + \frac{1}{2}a\epsilon_5^i \tag{3.16}$$
$$u^{2+} = u^{2-} + \frac{1}{2}b\epsilon_6^i \tag{3.17}$$
$$v^{2+} = v^{2-} + b\epsilon_2^i \tag{3.18}$$
$$w^{2+} = w^{2-} + \frac{1}{2}b\epsilon_4^i \tag{3.19}$$
$$u^{3+} = u^{3-} + \frac{1}{2}c\epsilon_5^i \tag{3.20}$$
$$v^{3+} = v^{3-} + \frac{1}{2}c\epsilon_4^i \tag{3.21}$$
$$w^{3+} = w^{3-} + c\epsilon_3^i \tag{3.22}$$

where u, v and w are nodal displacements in the three directions; 1, 2 and 3 are the hexahedral surfaces to which the nodes belong.

In order to verify the implemented equations, we had previously analyzed it with an isotropic material. The previous equations are applied for each one of the six canonical cases and the resultant deformation of the unitary cell is shown in Fig. 3.4.

Hexahedral dimensions are a, b, c and the opposite surfaces are indicated with signs "$+$" and "$-$" respectively. It is important to restrict the model in order to avoid rigid solid displacements. Hence all degrees of freedom of the central node are constrained. Rotations are avoided by the periodic boundary conditions imposed (Vercher *et al.* [2014]).

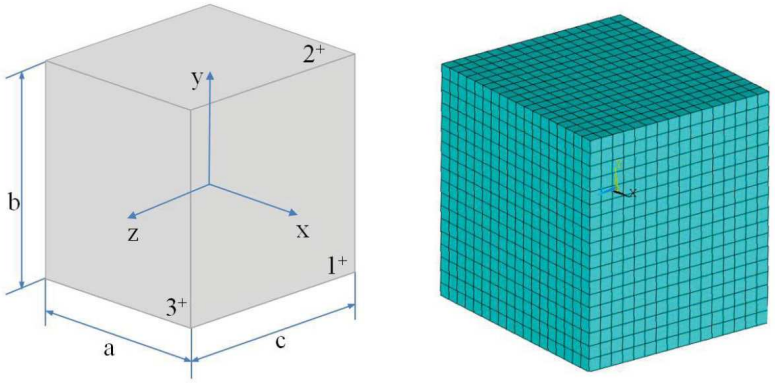

Figure 3.3: Schematic illustration of a representative cell and finite element model for an isotropic material.

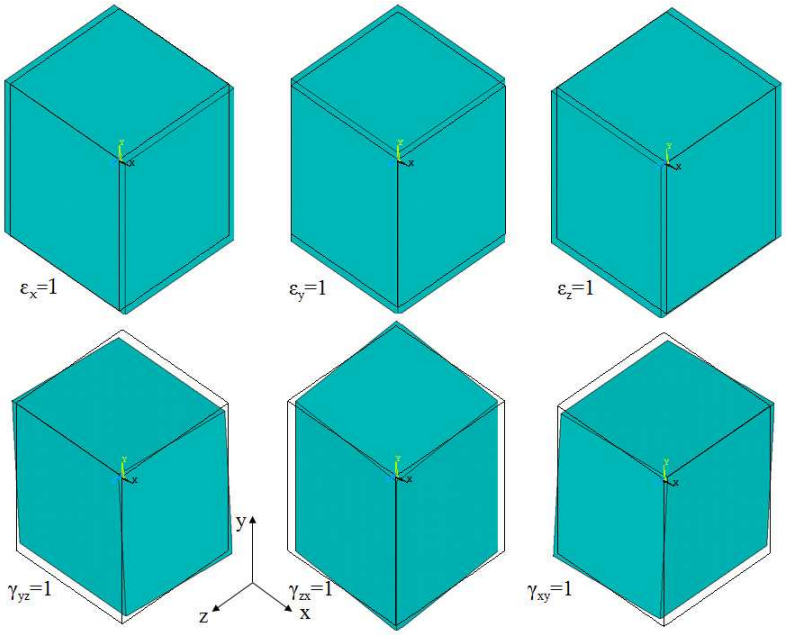

Figure 3.4: Deformed shape of each unitary strain field, applied to calculate the homogenized stiffness matrix of an isotropic material (Vercher *et al.* [2014]).

3.2 Elastic properties at nanostructural and sub-nanostructural levels

3.2.1 Unitary cell of a mineralized collagen fibril

After obtaining the expected results with the homogenization procedure described in Section 3.1.2 for an isotropic material, we proceeded with the collagen fibril structure. Fibrils have a diameter about 80-200 nm and its length is not a well known parameter due to distinction difficulties in micrographs caused by a tendency to coalescence. This associated structure of aligned fibrils forms a larger structure called fiber (Weiner *et al.* [1999]). As explained in Section 2.3, each fibril is composed of tropocollagen molecules forming a triple helix of approximately 300 nm of longitude and other non collagenous proteins which volume fraction is less than 10% (Yuan *et al.* [2011]). Bone crystals tend to form platelet shapes and there is a big dimension range in bibliography: 15–150 nm length, 10–80 nm width and 2–7 nm of thickness (Rubin *et al.* [2002]). Water is the third component in fibrils and although its presence is relevant, in the following calculations its influence is not estimated. Instead we consider it by using wet-collagen elastic properties.

Collagen molecules are staggered at a periodic axial distance D=67 nm and the molecule longitude is approximately of $4.4 \times D = 294.8$ nm (Rho *et al.* [1998]; Orgel *et al.* [2001]). From electronic micrographs and X–ray images reported in bibliography (Cowin [2001]; Wagner and Weiner [1992]; Weiner *et al.* [1991]; Nalla *et al.* [2003]) is evident that mineral platelets follow a staggered configuration in the axial direction of the fibril and also it is apparent from numerous studies that crystals form their nucleus between collagen molecules gaps and then compress the collagen molecules as they grow (Cowin [2001]). At radial (or transversal) direction the distribution or pattern is still uncertain in bibliography (Yuan *et al.* [2011]).

Inspired in many authors, in this work the crystal configuration is considered as a parallel layered structure in the fibril radial direction (Wagner and Weiner [1992]; Weiner *et al.* [1991]; Landis [2007]; Erts *et al.* [1994]). Nevertheless in the work by Yuan *et al.* [2011] it is established that the configuration of crystals in parallel layers is only valid at a small scale. At large scale, the collagen molecules are arranged in a

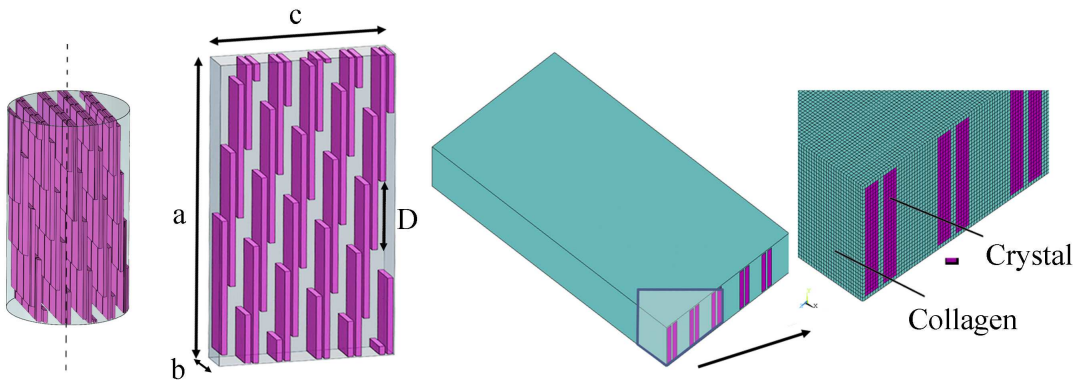

Figure 3.5: Representative volume element of a typical fibril structure modelled using finite elements by imposing periodical boundary conditions.

concentric pattern (Fig. 3.6) (Hulmes *et al.* [1995]). In this way the mineral platelets would grow concentrically around fibril (Jäger and Fratzl [2000]).

For the unitary cell of a mineralized collagen fibril, the crystals have been modeled as platelets with $L \times W \times T$ dimensions. In Fig. 3.1 it can be observed the staggered pattern in the axial direction and crystals are assumed parallel in radial direction of the fibril. An hexahedral of dimensions $a \times b \times c$ is then analysed. The geometrical model has been meshed with hexahedral solid elements. In Fig. 3.5 a detail of the model is shown. The constitutive matrix is obtained by applying boundary conditions described in Vercher *et al.* [2014] and the six unitary independent strain canonical cases.

The platelet dimensions considered are $L = 132.07$ nm (from Eq. 3.3), $W = 30$ nm and $T = 5$ nm, with a volume fraction of 0.3 (Vercher *et al.* [2014]; Vercher-Martínez *et al.* [2015]; Giner *et al.* [2014]). The distance between crystals in the longitudinal direction d_L, has been calculated by d_L=$4.4D - L$ because the periodic unit in this direction must be equal to the molecule longitude. The other distances d_W and d_T are 2 nm (see Fig. 3.1).

In fact the crystals not only nucleate between molecule gaps but probably also longitudinally across the molecule, although, this distribution is not well established in

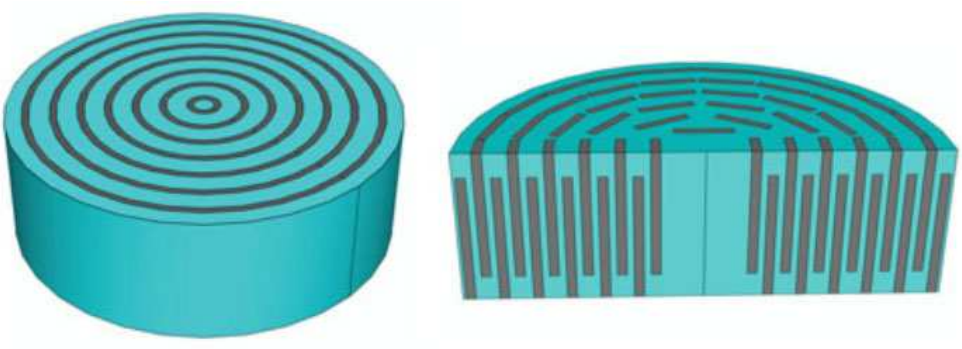

Figure 3.6: Mineralized collagen fibril structure proposed by Yuan *et al.* [2011] Left: 3-D axial symmetric structure (without considering individual platelets for the mineral phase); right: the 3-D complex model.

literature. We have considered the isotropic properties and dimensions reported in the work by Reisinger *et al.* [2011]: $E_{col} = 5$ GPa, $E_{ap} = 110.5$ GPa, $\nu_{col} = 0.3$ (Cusack and Miller [1979]) and $\nu_{ap} = 0.28$ (Yao *et al.* [2007]) and the periodical arrangement of the representative hexahedral shown in Fig. 3.5 with size: a = 294.8 nm, b = 32 nm and c = 154 nm.

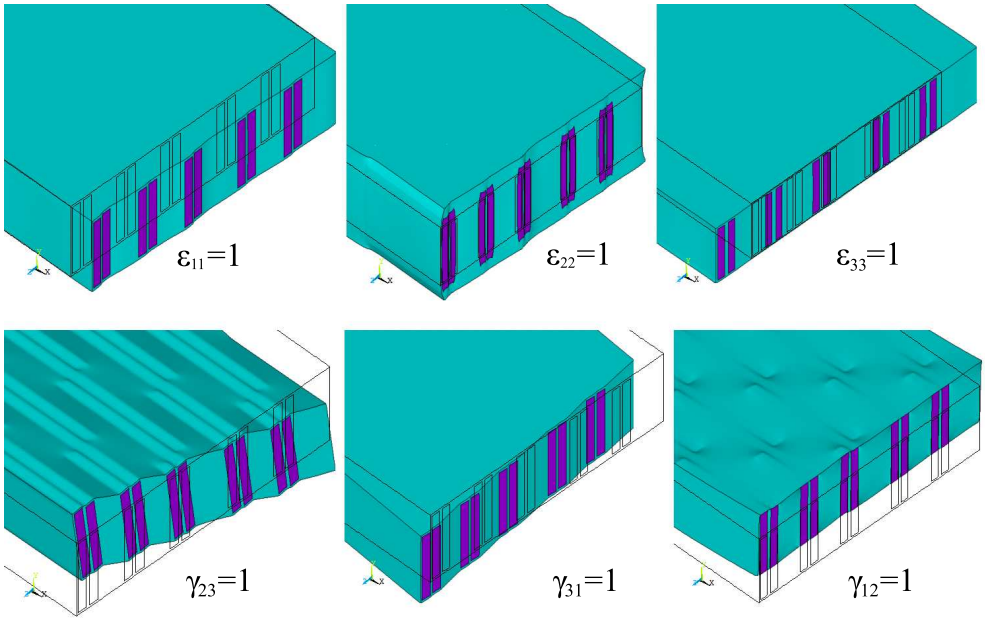

Figure 3.7: Deformed shape detail of each unitary strain field, applied to calculate the homogenized stiffness matrix of a mineralized collagen fibril with Vf = 0.3.

3.2.2 Numerical homogenization model of a mineralized collagen fibril

After applying the six canonical cases described in the previous section, the homogenized constitutive matrix of mineralized collagen fibril obtained C_{fib}, is the following:

$$\mathbf{C}_{\text{fib}} = \begin{pmatrix} 31.790 & 7.008 & 4.115 & 0 & 1.066 & 0 \\ & 25.050 & 3.666 & 0 & 0.162 & 0 \\ & & 9.706 & 0 & 0.001 & 0 \\ & & & 2.789 & 0 & 0.219 \\ & sym & & & 2.888 & 0 \\ & & & & & 7.74 \end{pmatrix} \text{GPa} \tag{3.23}$$

The obtained results show a monoclinic behaviour as was expected because the staggered pattern of the crystals has just one symmetry plane. The compliance matrix for the fibril has been calculated in the local coordinate system (1,2,3) shown in Fig. 3.1 by $S^l = (\mathbf{C}^{fib})^{-1}$. The elastic properties obtained with Eq. 3.23 are listed in Table 3.1. In Table 3.2 the simulation results are compared with other works which differ in geometrical and elastic property definition of collagen and mineral, some of them also include the presence of water which is not considered in this work. The last values are obtained with the same procedure explained in this Chapter but with different properties obtained by Martínez-Reina *et al.* [2010] and Rubin *et al.* [2003] for the first results and by Cusack and Miller [1979] and Yao *et al.* [2007] for the latter.

Fig. 3.7 shows a detail of the deformed shape of the fibril unitary volume where the stresses and strain components have been checked as equal at opposite faces.

The previous procedure can be used for any parameters of size and distribution of mineral and collagen if thermodynamical restrictions are satisfied. In this Thesis the properties used are from reported data on bibliography. Nevertheless in Vercher-Martínez *et al.* [2015], we provide numerical values and trends for all the elastic

Table 3.1: Elastic properties obtained by Eq. 3.23.

E_{11}	28.42 GPa
E_{22}	22.67 GPa
E_{33}	8.84 GPa
ν_{12}	0.228
ν_{23}	0.301
ν_{31}	0.105
G_{12}	7.73 GPa
G_{23}	2.78 GPa
G_{31}	2.85 GPa

Table 3.2: Elastic properties of mineralized collagen fibril reported values.

Author	E_{col}	E_{min}	ϕ_{min}	E_{fib}
Barkaoui *et al.* [2014]	2.5 GPa	120 GPa	0.24	0.9 GPa
Bar-On and Wagner [2013b]	1 GPa	100 GPa	0.3	4 GPa
Yoon and Cowin [2008]	1.26 GPa	114 GPa	0.25	3.4 GPa
Bar-On and Wagner [2013b] $_{\text{(H-T)model}}$	1 GPa	100 GPa	0.3	15 GPa
Akkus [2005]	2.9 GPa	74 GPa	0.3	17.69 GPa
Reisinger *et al.* [2010]	5 GPa	110.15 GPa	0.3	18 GPa
Present Thesis	1.2 GPa	114 GPa	0.3	14.67 GPa
Present Thesis	5 GPa	110.15 GPa	0.3	28.42 GPa

constants of the mineralized collagen fibril as a function of the volume fraction of mineral. In our results, we verify the large influence of the mineral overlapping on the mechanical response of the fibril and we highlight that the lateral distance between crystals is relevant to the mechanical behavior of the fibril and not only the mineral overlapping in the axial direction.

3.2.3 Effect of longitudinal and lateral overlap

In Fig. 3.8 an example of variation of cristal lengths inside unitary cell volumes models of mineralized collagen fibrils is shown, where width (W) and thickness (T) dimensions remain constant. In Fig. 3.9 we can see the influence of mineral overlapping on the Young's modulus for different elastic properties and volume fraction of constituents. Collagen and mineral have been assumed isotropic and two sets of material properties, widely used in the literature, have been considered.

The properties referenced as "Prop1" are taken from the work by Martínez-Reina *et al.* [2010]: $E_{col} = 1.2$ GPa, $E_{ap} = 114$ GPa, $\nu_{col} = 0.35$ and $\nu_{ap} = 0.28$. The properties denoted as "Prop2" are taken from Reisinger *et al.* [2011] and were used in previous works (Vercher *et al.* [2014]): $E_{col} = 5$ GPa, $E_{ap} = 110.5$ GPa, $\nu_{col} = 0.3$ and $\nu_{ap} = 0.28$.

Fig. 3.9 shows an abrupt change in the slope of E_x and then, the curve intersects the transverse Young's modulus, E_y for both sets of material properties. This trend is also noticed in Gao *et al.* [2003] and Bar-On and Wagner [2013b,a]. From the intersecting point rightwards, the mineralized collagen fibril begins to benefit from the mineral stiffness. It is important to notice that the constituent properties have a quantitative (but not qualitative) influence on the results, principally in the results of E_x. A change in the slope of E_y and E_x is observed. We note in passing that this should be carefully analyzed if the materials were not isotropic.

In Fig. 3.11, Young's moduli evolution is represented as a function of the volume fraction of mineral, by varying the lateral space between platelets. For the sake of clarity, only the results for the platelet length of $L = 66$ nm are depicted. It is noticeable that again a steep change occurs in the behavior of E_x.

By reducing the lateral space between platelets, the mineralized collagen fibril can exhibit a higher stiffness in the axial direction of the fibril as a consequence of the platelet alignment. However this behavior is also dependent on the platelet length: there exist lengths for which this phenomenon never occurs (Vercher-Martínez *et al.* [2015]).

From Figs. 3.9 and 3.11 it can be observed that both mineral length and lateral distance between layers have an important role in the elastic behavior of the fibril. In this sense, in Vercher-Martínez *et al.* [2015] it is shown that both variables are closely related.

3.3 Elastic properties at lamellar level

It is important to remark that the constitutive matrix Eq. 3.23 of the mineralized collagen fibril obtained previously is expressed in a local coordinate system (with $\psi_1 = \psi_2 = 0$) and, in order to associate it with a cylindrical osteon system (r, θ, z) (see Figs. 3.12 and 3.13), the following cases should be considered:

- Firstly, the crystal can rotate an angle ψ_1 with respect of the osteon radial axis. Note that the unidirectional fibril orientation is approximately parallel to the principal c axis of its crystals, as is described on Akiva *et al.* [1998], see Fig. 3.12.
- Secondly, the apatite crystal can rotate an angle ψ_2 over its own c axis, as it is represented in Fig. 3.12.

Table 3.3 shows the cosines of the angles that the local auxiliary coordinate system (x,y,z) with respect to the oriented coordinate system (1,2,3) are listed. The equations of Akiva *et al.* [1998] were used to obtain these values where two rotations ψ_1 and ψ_2 have been considered.

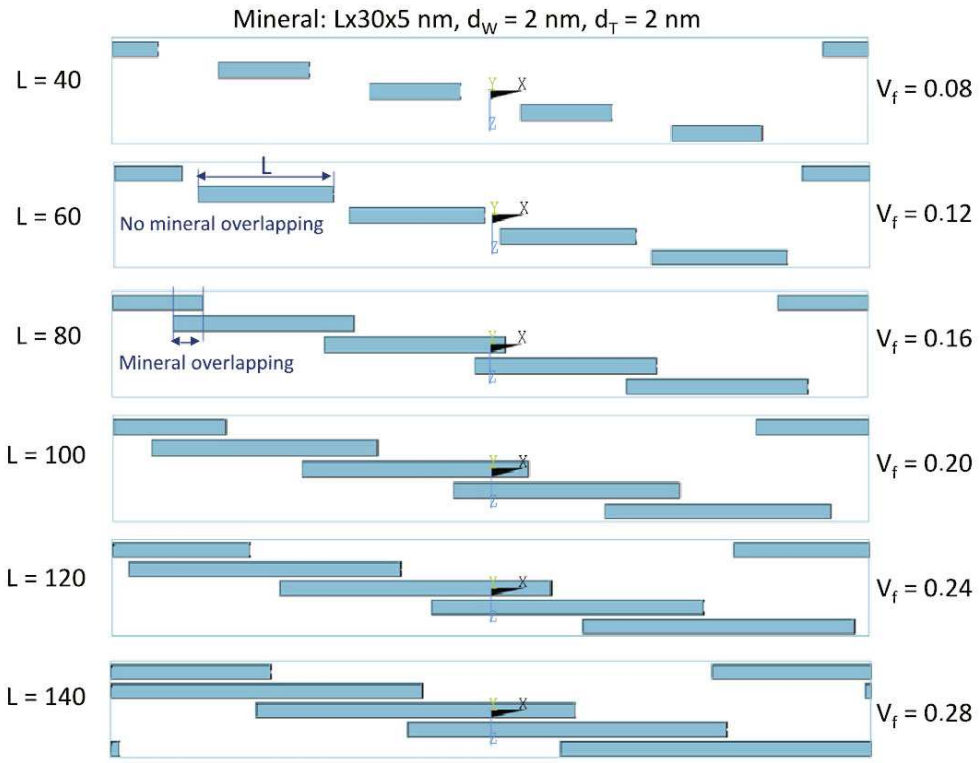

Figure 3.8: Example of some cell volumes analyzed with different mineral lengths, from L = 40 nm to L = 140 nm with increments of 20 nm. Dimensions W, T and d_W remain constant. In this figure, d_T = 2 nm. The mineral is represented in blue and collagen in white (Vercher-Martínez *et al.* [2015]).

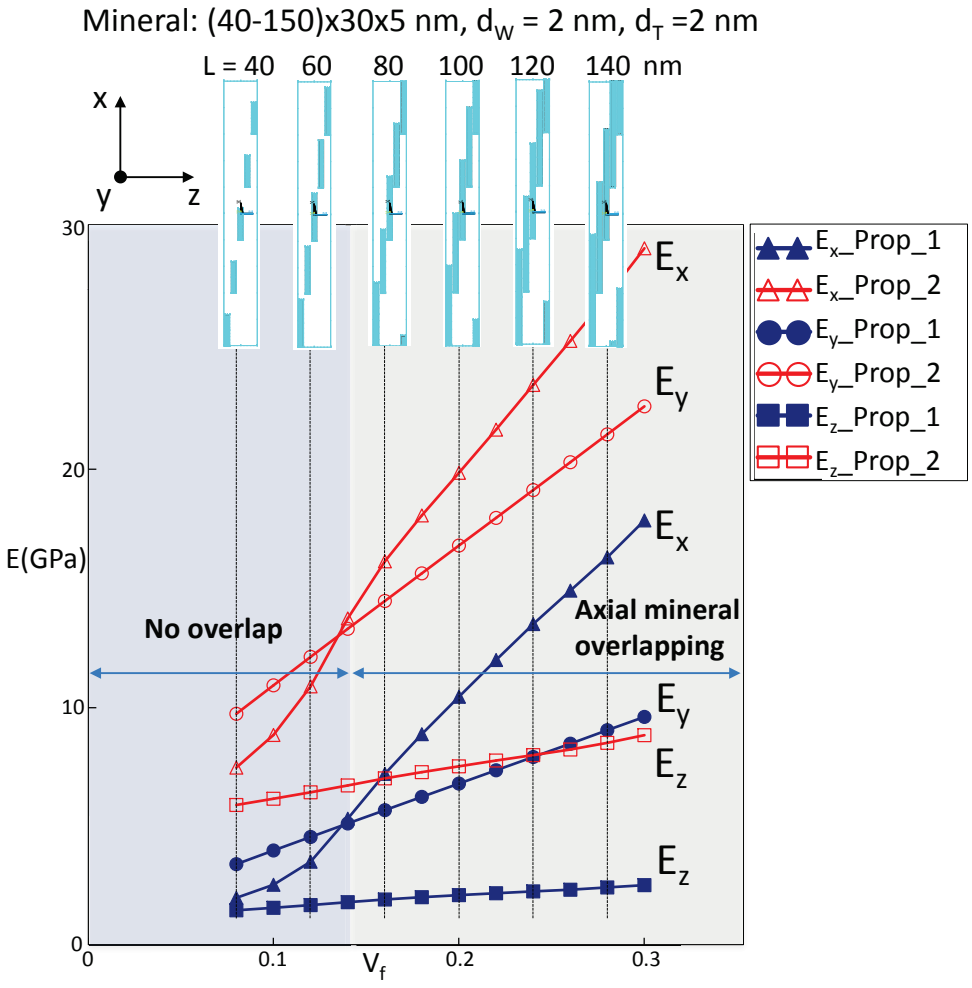

Figure 3.9: Variation of Young's moduli with volume fraction of mineral by considering different platelet lengths, in the range L ∈ [40, 150] nm. Results are obtained for two sets of constituent elastic properties. Lateral space between platelets, d_T, remains constant and equal to 2 nm (Vercher-Martínez *et al.* [2015]).

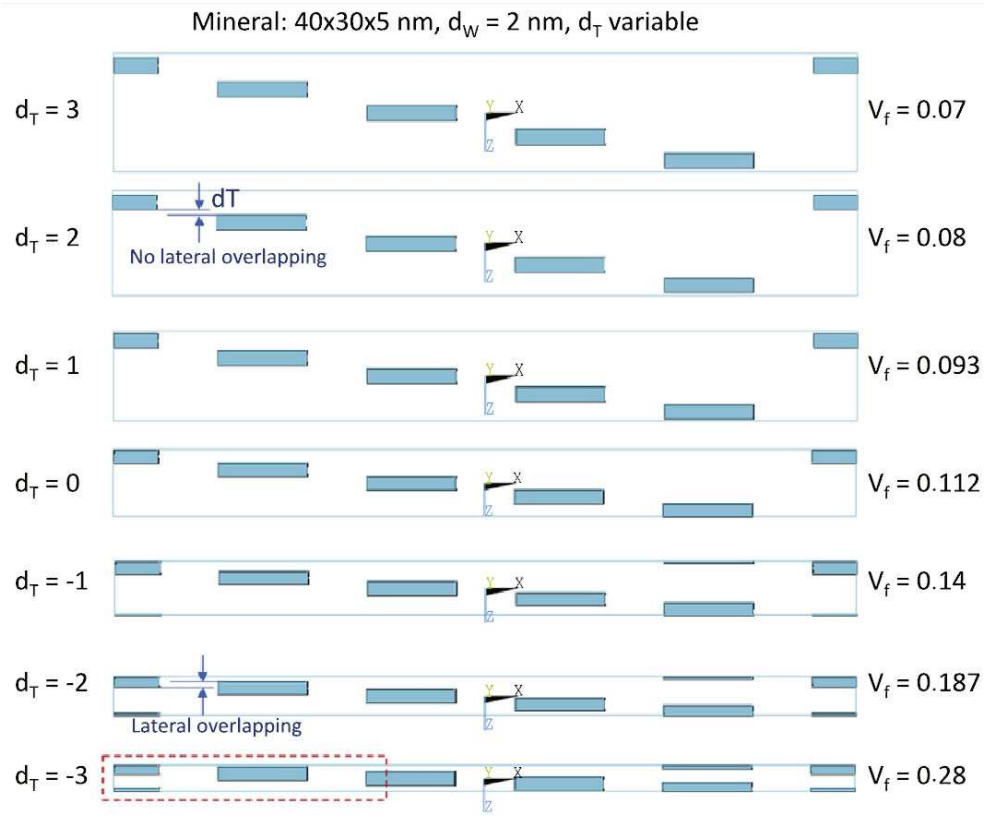

Figure 3.10: Example of cell volumes analyzed varying the lateral space between minerals, in the range $d_T \in$ [3, -3] nm. Dimensions W, T and d_W remain constant. In this figure, L = 40 nm. The mineral is represented in blue and collagen in white (Vercher-Martínez *et al.* [2015]).

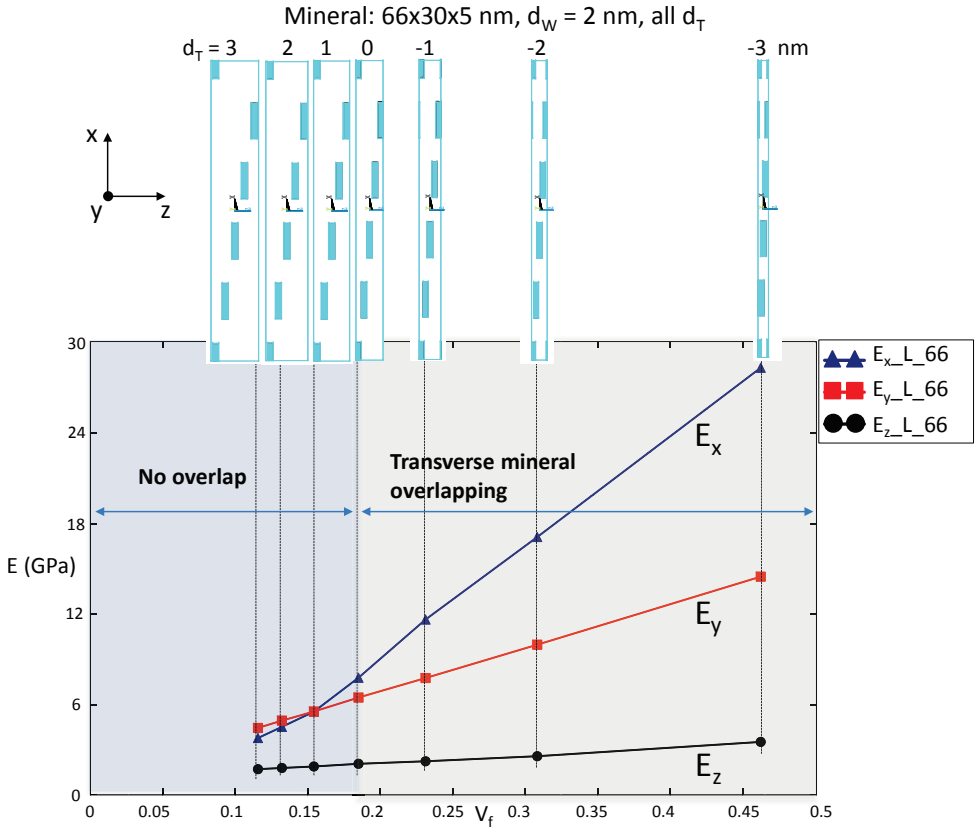

Figure 3.11: Variation of Young's moduli with volume fraction of mineral by considering different lateral space between platelets, in the range $d_T \in [3, -3]$ nm. Results are obtained for a constant platelet length, L = 66 nm (Vercher-Martínez *et al.* [2015]).

Table 3.3: Cosines of the angles that the local auxiliary directions (x, y, z) form with respect to the local orientated directions (1, 2, 3)

	1	2	3
x	α_1	β_1	γ_1
y	α_2	β_2	γ_2
z	α_3	β_3	γ_3

where
$$\begin{array}{lll} \alpha_1 = \cos(\psi_1) & \beta_1 = \sin(\psi_1)\cos(\psi_2) & \gamma_1 = -\sin(\psi_1)\sin(\psi_2) \\ \alpha_2 = -\sin(\psi_1) & \beta_2 = \cos(\psi_1)\cos(\psi_2) & \gamma_2 = -\cos(\psi_1)\sin(\psi_2) \\ \alpha_3 = 0 & \beta_3 = \sin(\psi_2) & \gamma_3 = \cos(\psi_2) \end{array}$$

The matrix $\mathbf{S}^g$ in Eq. 3.24, refers to a mineralized collagen fibril expressed in the global coordinate system of the osteon. This can lead to a constitutive matrix of an anisotropic material that can be expressed as a function of engineering constants.

$$\mathbf{S}^g = \begin{pmatrix} \frac{1}{E_{xx}} & \frac{-\nu_{yx}}{E_{yy}} & \frac{-\nu_{zx}}{E_{zz}} & \frac{\eta_{x,yz}}{G_{yz}} & \frac{\eta_{x,zx}}{G_{zx}} & \frac{\eta_{x,xy}}{G_{xy}} \\ \frac{-\nu_{xy}}{E_{xx}} & \frac{1}{E_{yy}} & \frac{-\nu_{zy}}{E_{zz}} & \frac{\eta_{y,yz}}{G_{yz}} & \frac{\eta_{y,zx}}{G_{zx}} & \frac{\eta_{y,xy}}{G_{xy}} \\ \frac{-\nu_{xz}}{E_{xx}} & \frac{-\nu_{yz}}{E_{yy}} & \frac{1}{E_{zz}} & \frac{\eta_{z,yz}}{G_{yz}} & \frac{\eta_{z,zx}}{G_{zx}} & \frac{\eta_{z,xy}}{G_{xy}} \\ \frac{\eta_{yz,x}}{E_{xx}} & \frac{\eta_{yz,y}}{E_{yy}} & \frac{\eta_{yz,z}}{E_{zz}} & \frac{1}{G_{yz}} & \frac{\mu_{yz,zx}}{G_{zx}} & \frac{\mu_{yz,xy}}{G_{xy}} \\ \frac{\eta_{zx,x}}{E_{xx}} & \frac{\eta_{zx,y}}{E_{yy}} & \frac{\eta_{yz,z}}{E_{zz}} & \frac{\mu_{zx,yz}}{G_{yz}} & \frac{1}{G_{zx}} & \frac{\mu_{zx,xy}}{G_{xy}} \\ \frac{\eta_{xy,x}}{E_{xx}} & \frac{\eta_{xy,y}}{E_{yy}} & \frac{\eta_{xy,z}}{E_{zz}} & \frac{\mu_{xy,yz}}{G_{yz}} & \frac{\mu_{xy,zx}}{G_{zx}} & \frac{1}{G_{xy}} \end{pmatrix} \tag{3.24}$$

where $\eta_{i,jk}$ the mutual influence coefficients (type 1 and 2) defined by Lekhnitskii [1963]; $\mu_{ij,kl}$ are Chentsov coefficients or ratios between shear strains caused by a

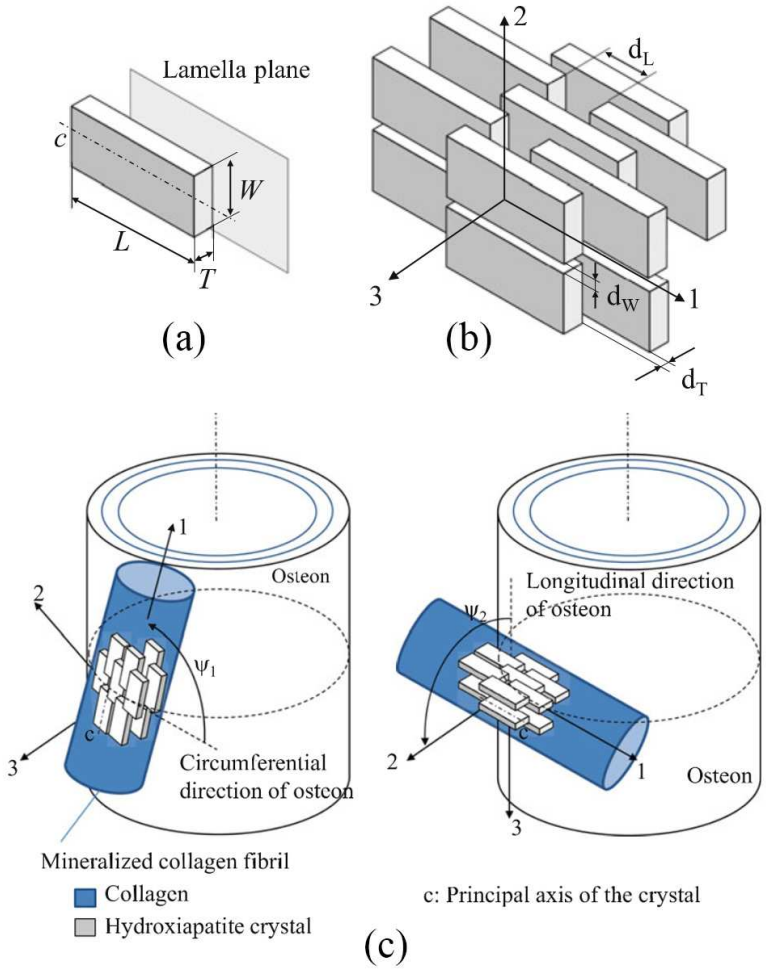

Figure 3.12: Schematic illustration of several details at different scales: (a) Crystal dimensions L, W and T, c represents the principal axis of the crystal which remains always parallel to the lamella plane. (b) Staggered crystal distribution. Local or orientated coordinate system (1, 2, 3) in which elastic constants are calculated through Halpin-Tsai equations. d_L, d_T and d_W, are the distances between crystals in three dimensions. (c) Following Akiva *et al.* [1998], two possible rotations of the crystals are defined: ψ_1 is the angle rotated around the normal direction of the lamella plane and ψ_2 is the angle rotated around their own principal axis, c.

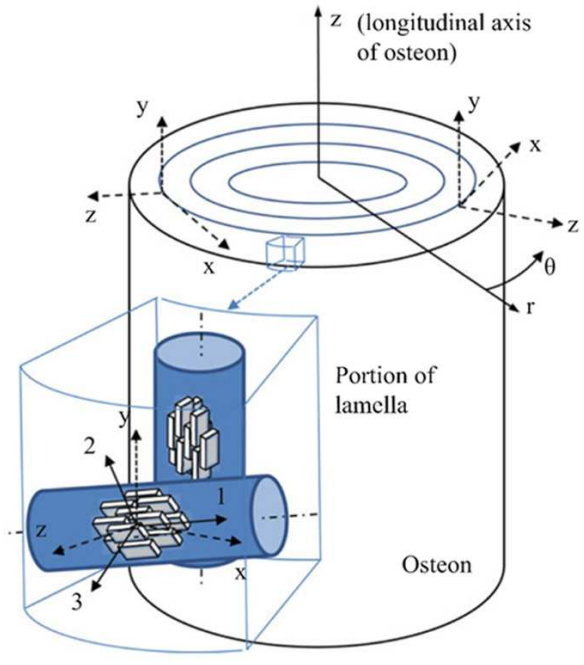

Figure 3.13: Coordinate system scheme. Cylindrical coordinate system (r, θ, z) is used as a global coordinate system, and a local auxiliary coordinate system (x, y, z) is defined at any point, being (x, y, z) coincident with (θ, z, r), respectively.

shear stress. Now it is possible to obtain the elastic constants in the cylindric system with the following expressions:

$$\begin{aligned} E_{rr} &= \frac{1}{S^g_{33}} \quad G_{r\theta} = \frac{1}{S^g_{55}} \quad \nu_{r\theta} = -\, S^g_{13}\frac{1}{S^g_{33}} \\ E_{\theta\theta} &= \frac{1}{S^g_{11}} \quad G_{\theta z} = \frac{1}{S^g_{66}} \quad \nu_{\theta z} = -\, S^g_{21}\frac{1}{S^g_{11}} \\ E_{zz} &= \frac{1}{S^g_{22}} \quad G_{zr} = \frac{1}{S^g_{44}} \quad \nu_{zr} = -\, S^g_{32}\frac{1}{S^g_{22}} \end{aligned} \tag{3.25}$$

where numerical subscripts are referred to the entries of $\mathbf{S}^g$ matrix and where local auxiliary coordinate system (x, y, z) used in Eq. 3.11 and 3.24, corresponds directly to the global system of the osteon. Analogously, the constitutive matrix of the fibril in the global coordinate system will show a complete matrix with the form:

$$\mathbf{C}^g = \begin{pmatrix} C_{11} & C_{12} & C_{13} & C_{14} & C_{15} & C_{16} \\ C_{21} & C_{22} & C_{23} & C_{24} & C_{25} & C_{26} \\ C_{31} & C_{32} & C_{33} & C_{34} & C_{35} & C_{36} \\ C_{41} & C_{42} & C_{43} & C_{44} & C_{45} & C_{46} \\ C_{51} & C_{52} & C_{53} & C_{54} & C_{55} & C_{56} \\ C_{61} & C_{62} & C_{63} & C_{64} & C_{65} & C_{66} \end{pmatrix} \tag{3.26}$$

Using Eq. 3.25 Young's modulus, Poisson's ratios and shear modulus can be obtained for the mineralized collagen fibril. For example, considering all crystals aligned with longitudinal axis of the osteon and with no rotation over its own c axis, i.e. $\psi_1 = \psi_2 = 0$, the properties obtained are listed in Table 3.1.

Fig. 3.15 represents the variation of Young's modulus in different local auxiliary directions x e y when ψ_1 takes values between 0° and 90°. In this case, as $\psi_2 = 0°$, Young's modulus E^{fib}_{zz} is coincident with E^{fib}_{33} and has a constant value of 8.84 GPa. It should

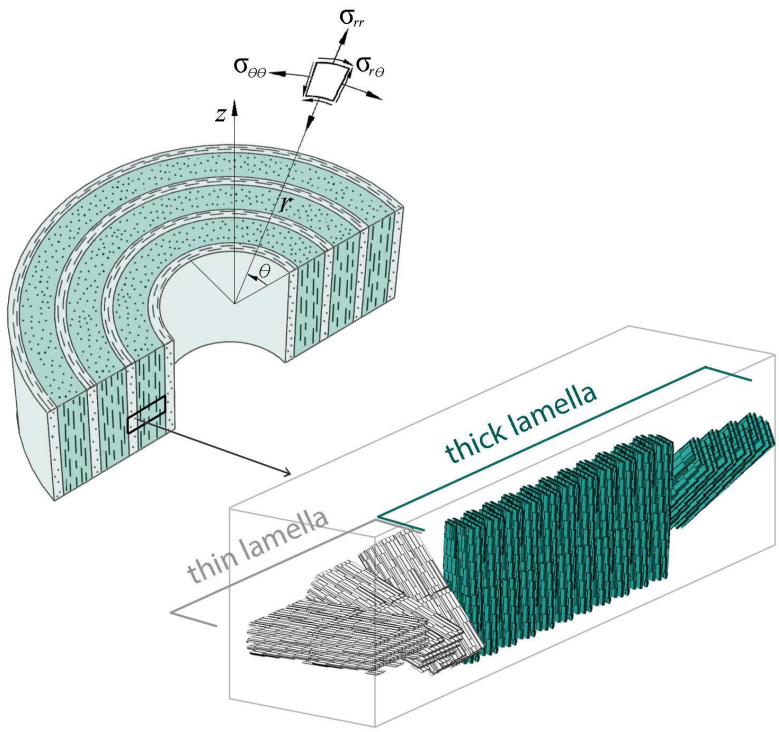

Figure 3.14: Model of an osteon with thin and thick lamellae, showing the cylindrical reference system (r, θ, z) aligned with the osteon axis. Condensation of the 5 sublamellar structure, with 5 different mineralized fibril orientations, into two equivalent layers: thin and thick lamellae.

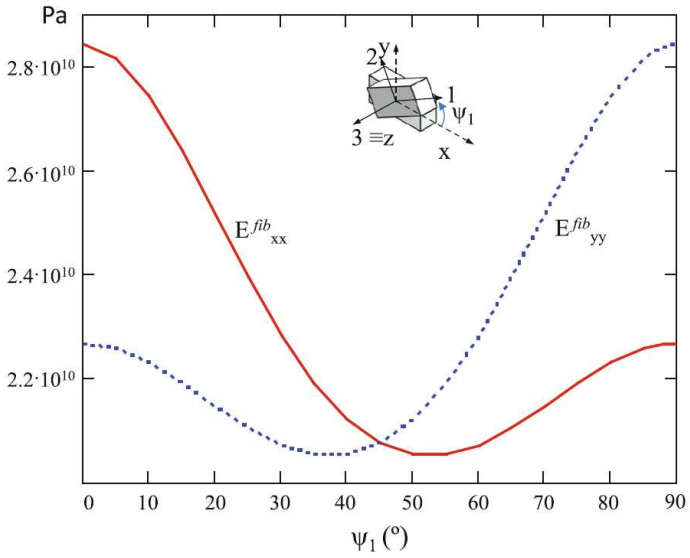

Figure 3.15: Variation of mineralized collagen fibril Young's moduli ($E^{fib}_{xx}, E^{fib}_{yy}$) in plane xy. ψ_1 is the rotation angle (Vercher *et al.* [2014]).

be noted that E^{fib}_{yy} is the one that initially shows lower values, being its minimum of 20.54 GPa near ψ_1= 35°. E^{fib}_{xx} shows a complementary trend with respect to E^{fib}_{yy} being its minimum value at ψ_1=55°.

The trends for Poisson's ratios and shear moduli are summarized next. The Poisson's ratio that shows the greatest variation with ψ_1 is ν^{fib}_{xy}, being its maximum value 0.346 at $\psi_1 = 40°$ and its minimum value 0.182 at $\psi_1 = 90°$. ν^{fib}_{yz} and ν^{fib}_{zx} present more uniform values indicating a high anisotropic behavior. Shear moduli G^{fib}_{yz} and G^{fib}_{zx} remain almost constant about 2.8 GPa. The maximum value is reached by $G^{fib}_{xy} =$ 10.5 GPa at $\psi_1 = 45°$.

Poisson's ratios and shear moduli variations with the angle ψ_2 are shown in Figs. 3.18–3.20. As ψ_1= 0, Young's modulus in x direction is constant, $E^{fib}_{xx} = 32.53$ GPa and is coincident with E^{fib}_{11}. It should be noticed that E^{fib}_{zz} firstly decreases with respect to ψ_2 reaching its minimum value of 7.68 GPa approximately at $\psi_2 = 35°$ (Fig. 3.18). As expected, E^{fib}_{yy} shows a complementary trend with respect to E^{fib}_{zz} being its minimum value around $\psi_2 = 55°$.

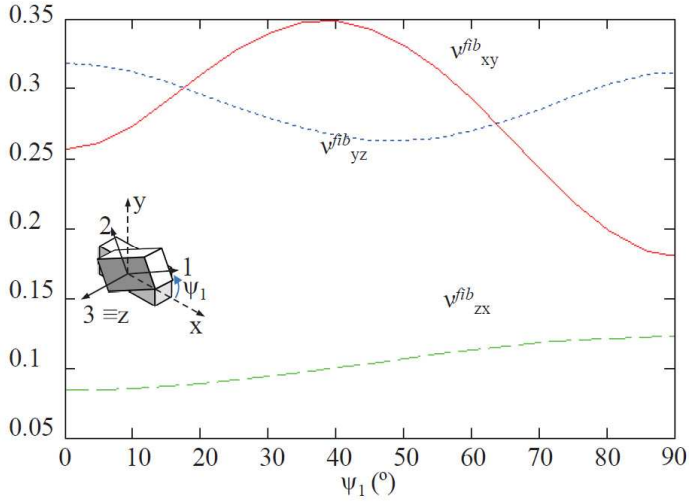

Figure 3.16: Variation of mineralized collagen fibril Poisson ratios (ν_{xy}^{fib}, ν_{yz}^{fib}, ν_{zx}^{fib}) in plane z. ψ_1 is the rotation angle (Vercher *et al.* [2014]).

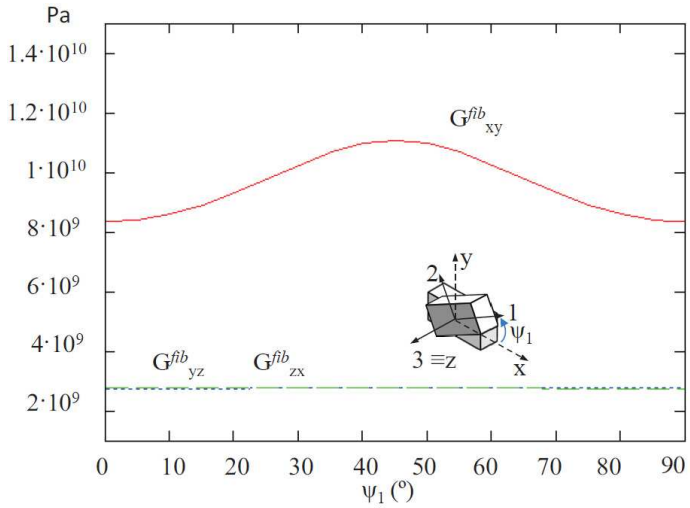

Figure 3.17: Variation of mineralized collagen fibril shear moduli ($G_{xy}^{fib}, G_{yz}^{fib}, G_{zx}^{fib}$) in plane z. ψ_1 is the rotation angle (Vercher *et al.* [2014]).

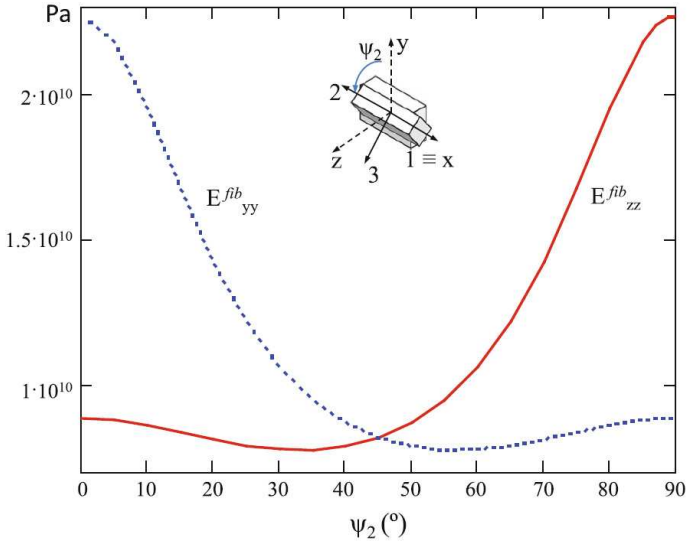

Figure 3.18: Variation of mineralized collagen fibril Young's moduli (E^{fib}_{xx}, E^{fib}_{yy}) in plane x. ψ_2 is the rotation angle (Vercher *et al.* [2014]).

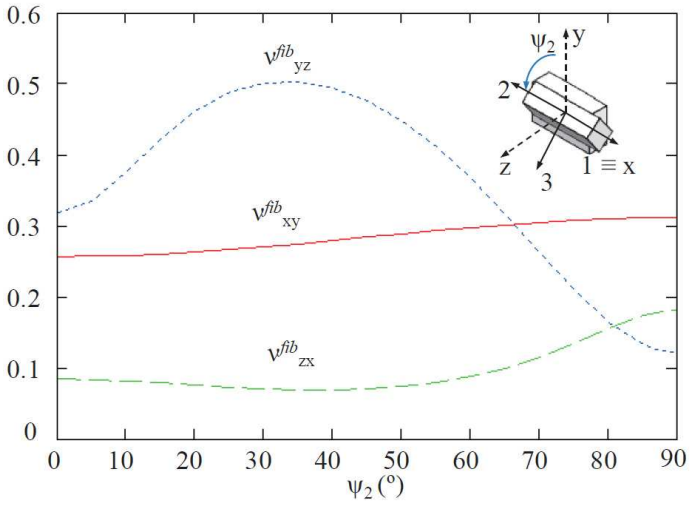

Figure 3.19: Variation of mineralized collagen fibril Poisson ratios (ν^{fib}_{xy}, ν^{fib}_{yz}, ν^{fib}_{zx}) in plane x. ψ_2 is the rotation angle (Vercher *et al.* [2014]).

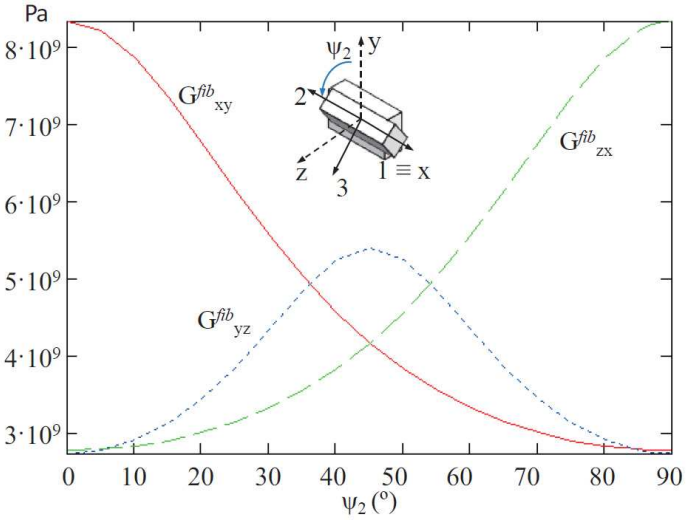

Figure 3.20: Variation of mineralized collagen fibril shear moduli ($G_{xy}^{fib}, G_{yz}^{fib}, G_{zx}^{fib}$) in plane x. ψ_2 is the rotation angle (Vercher *et al.* [2014]).

The Poisson's ratio ν_{xy}^{fib} does not vary much with ψ_2, taking values between 0.228 and 0.33, see Fig. 3.19. The greatest variation in its plane occurs for ν_{yz}^{fib} with a maximum value of 0.503 at about $\psi_2 = 35°$ with a minimum value of 0.122 at $\psi_2 = 90°$. The variation of ν_{zx}^{fib} with the angle ψ_2 is similar to that shown with the angle ψ_1 (Fig. 3.16). Also it can be noticed that all shear moduli vary widely with ψ_2. G_{xy}^{fib} and G_{zx}^{fib} show the same maximum value (7.73 GPa) at ψ_2 =0 and 90° respectively, exhibiting also a symmetrical trend with respect to each other (Fig. 3.20). G_{yz}^{fib} is maximum at $\psi_2 = 45°$ with 5.4 GPa.

3.3.1 Elastic properties of secondary osteons

From mineralized collagen fibril elastic properties, the next hierarchical level properties i.e. lamellar properties, can be derived.

Following the structure proposed by Weiner *et al.* [1991] described in the previous Chapter 2, the sublayer with fibrils at 0° (sublayer 1 in Fig. 2.3) is parallel to superior

Table 3.4: ψ_1 collagen fibril angles and ψ_2 for crystals with respect to its own axis for each sublayer of thin lamella

	$\psi_1(^o)$	$\psi_2(^o)$	t (μm)
sublayer 1	0	0	0.4
sublayer 2	30	0	0.2
sublayer 3	60	0	0.2

Table 3.5: ψ_1 collagen fibril angles and ψ_2 for crystals with respect to its own axis for each sublayer of thick lamella

	$\psi_1(^o)$	$\psi_2(^o)$	t (μm)
sublayer 4	90	70	1.8
sublayer 5	120	30	0.6

and inferior limits of the lamellae. Here the c axis of crystals are in a perpendicular orientation with respect to the longitudinal axis of the osteon. This sublayer is called thin lamellae by Akiva *et al.* and has a thickness of 0.4 nm (Akiva *et al.* [1998]).

In successive sublayers, the c axis of crystals rotates as follows: ψ_1=(30°, 60°, 90°, 120°). The angle ψ_2 (rotation of the crystals over its own axis) is not quantified yet in literature (Akiva *et al.* [1998]). Second and third sublayers constitute a transition zone of approximately 0.4 μm. In Akiva *et al.* [1998], sublayers fourth and fifth are called "$thick\ lamella$" and "$back-flip\ lamella$", and have a thickness of 1.8 μm and 0.6 μm respectively. This pattern can fit the configuration of a rotated staggered structure.

The procedure for obtaining the constitutive matrices of a lamella is analogous to the one followed for the collagen fibril:

- According to Table 3.3 of Section 3.3, the cosines of ψ_1 and ψ_2 are calculated. These angles are formed by the local auxiliary system of coordinates (x,y,z)

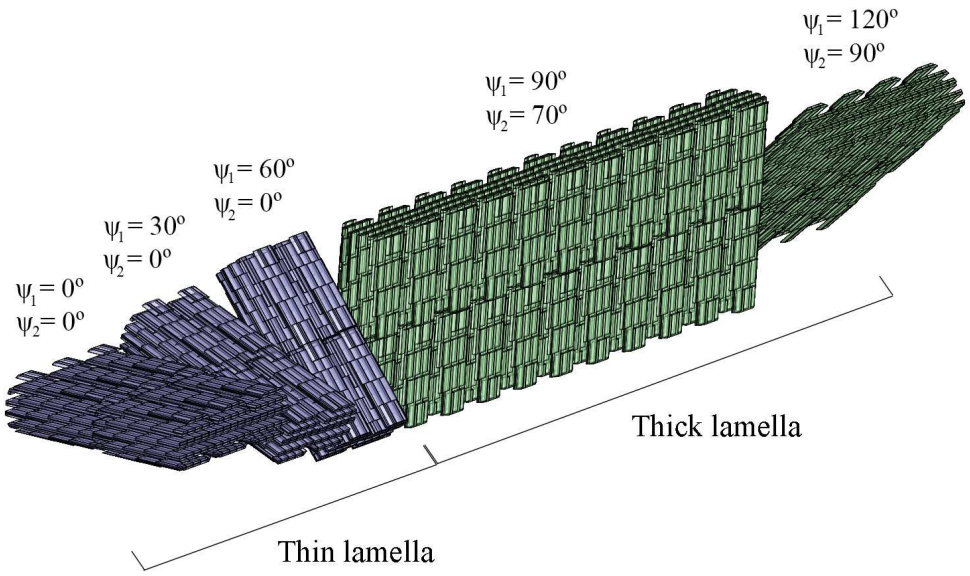

Figure 3.21: Schematic illustration of five lamellar sublayers grouped as thick (green) and thin (purple) lamellae.

with the oriented one (1,2,3) for each one of the five sublamellae. The angles used are in Tables 3.4 and 3.5.

- The matrix **q** (Eq. 3.12) of coordinate transformation is calculated from director cosines obtained for each sublayer in the previous step.
- From Eq. 3.11 we obtain the compliance matrix for each sublayer with its particular crystal orientation.
- The constitutive matrices are obtained by $\mathbf{C}^g = (\mathbf{S}^g)^{-1}$.
- With the obtained constitutive matrices for each sublamella, the matrix of the group can be obtained by the rule of mixtures which will be explained in the following Subsection 3.3.2.

3.3.2 Homogenized properties for thick and thin lamellae

Defining explicitly 5 sublayers in each lamella, is a difficult and high computational cost procedure if we want to represent the microstructural level of cortical bone (tens of lamellae). In order to simplify the FE model of the osteon, we have grouped the 5 sublayers in two that will be called in this Thesis as thick and thin lamellae with thicknesses of 0.8 μm and 2.4 μm respectively, as shown in Fig. 3.21.

The rule of mixtures is a well known procedure to estimate elastic properties in composite materials. The following equations 3.27 and 3.28 are used for thick and thin lamellae constitutive properties (Tables 3.4 and 3.5). These values are taken from Akiva *et al.* [1998].

$$D_{thin} = \frac{1}{T_{thin}}(T_1 D_1 + T_2 D_2 + T_3 D_3) \tag{3.27}$$

$$D_{thick} = \frac{1}{T_{thick}}(T_4 D_4 + T_5 D_5) \tag{3.28}$$

where D is the elastic property and T is the thickness of each sublamella, $T_{thin} = T_1 + T_2 + T_3$; $T_{thick} = T_4 + T_5$

This procedure is applied to each one of the terms of $\mathbf{C}^g$ matrix for thin and thick lamellae and finally the group property is obtained.

$$\mathbf{C}_{thin} = \begin{pmatrix} 27.136 & 9.977 & 4.003 & 0.729 & 0.699 & -0.254 \\ & 23.766 & 3.779 & 0.729 & 0.335 & -0.166 \\ & & 9.706 & 0.097 & 0.001 & -0.0004 \\ & & & -0.014 & 0.124 & 6.531 \\ & sym & & & 4.102 & 1.052 \\ & & & & & -0.014 \end{pmatrix} \text{GPa} \tag{3.29}$$

$$\mathbf{C}_{thick} = \begin{pmatrix} 13.567 & 6.241 & 0.316 & 0.122 & -2.741 & 3.299 \\ & 29.934 & -0.606 & -0.219 & -1.182 & 6.137 \\ & & -0.039 & 0.539 & -2.316 & 21.269 \\ & & & 0.139 & -0.129 & 4.191 \\ & sim & & & 7.04 & -0.324 \\ & & & & & 3.079 \end{pmatrix} \text{GPa} \tag{3.30}$$

3.3.3 Elastic properties of interstitial tissue

The first type of bone in mammals is an interwoven tissue with course collagen fibers with randomly organized osteocytes (Cowin [2001]). In human, woven bone is resorbed and replaced by lamellar bone at age 2 and 3 years where fibrils are arranged into plywood-like layers. That tissue is called primary bone. With time and growth, bones need to reshape and remodel by forming new osteons over that primary tissue (that continues with the lamellar structure) that is called interstitial tissue. Some authors affirm that interstitial tissue is more mineralized because minerals continue growing after remodeling (Martínez-Reina *et al.* [2010]; Ascenzi *et al.* [2013]; Prendergast and Huiskes [1996]). That theory is reasonable from the point of view of the protecting role that more fragility can give to interstitial bone over osteons (Schaffler *et al.* [1995]). This idea is reinforced in Cowin [2001]: "Although the magnitudes of crack density vary greatly between investigators, approximately half to two thirds of the total in vivo cracks have been observed in the interstitial tissue. Only a small fraction of the cracks were observed entirely within osteons." (Cowin [2001]).

Although the bibliography about elastic properties of interstitial tissue is scarce, there is consensus that it is a stiffer tissue than secondary osteons by 10-15 % (Rho *et al.* [2001]; Chan and Nicolella [2012]; Budyn and Hoc [2007]; Li *et al.* [2013]). Hence, in this Thesis the constitutive matrix of interstitial tissue is calculated by Eq. 3.31, where $\mathbf{C}_{osteon}$ is the constitutive matrix of the five sublayered osteon lamella, obtained by applying the rule of mixtures explained in Section 3.3.2. In Table 3.6 there are

Table 3.6: Elastic properties of interstitial bone reported in literature, where E is Young's modulus in the longitudinal orientation of bone and ν is the Poisson's ratio

Author	E (GPa)	ν	Source
Rho *et al.* [1997]	25.8 ± 0.7	0.3	Human
Zysset *et al.* [1999]	25 ± 4.3	0.3	Human
Dong and Guo [2006]	19.31	0.3	Human
Li *et al.* [2013]	14.12	0.153	Human
Nobakhti *et al.* [2014]	13.73 ± 6.56	0.3	Bovine

some values of Young's modulus and Poisson's ratios from different authors, but for consistency with the properties previously defined, Eq. 3.31 is used.

$$\mathbf{C}_{interstitial} = \mathbf{C}_{osteon} \times 1.10 \tag{3.31}$$

3.3.4 Elastic properties of cement line

During bone remodeling, osteoclasts (bone resorption cells) demarcate a zone over interstitial tissue for new material to be deposited. The cement line corresponds to the thin line delimitating the new osteon.

At microstructural scale, in a composite where secondary osteons can be considered as reinforcement fibers and interstitial tissue as the matrix, cement lines would act as an interface. The cement line is a very thin layer (≈ 1 μm) compared with lamellae and its composition and degree of mineralization compared with other elements of cortical bone (osteons and interstitial tissue) is still a discussed topic in bibliography. There are authors that suggest that collagen fibers of osteons do not pass through cement lines, making them the weakest link of cortical bone, and that could be a reason to the common phenomenon of microcracks firstly propagating through cement lines than penetrating osteons (Skedros *et al.* [2005]).

Table 3.7: Elastic properties of cement line in literature

Low mineralized CL	High mineralized CL
Fawns and Landells [1953]	Skedros *et al.* [2005]
Lakes *et al.* [1979]	Davies [2007]
Frasca *et al.* [1981]	Busse *et al.* [2009]
Burr *et al.* [1988]	Launey *et al.* [2010]
Park and Lakes [1986]	
Nobakhti *et al.* [2014]	

In Burr *et al.* [1988] a constituent analysis of cement line with the suggestion of a low mineralized composition is made. This theory is consistent with the hypothesis that cement line provides a weak interface with interstitial tissue and is consistent with the differences found in punctual specific stiffness in their experiments. A weak interface between interstitial tissue (matrix) and osteons (reinforcement) leads to a poor stress transmission capacity that promotes crack initiation in cement lines but slows it down in interstitial matrix, thus representing a barrier to osteons. Burr *et al.* [1988] also suggest that cement lines are responsible of a portion of viscoelasticity of bone, particularly in long time and slow frequencies for bovine and human bone. There are also authors that question and contradict the premise of low content of mineral in cement lines with experimental results affirming a high mineralization level (Davies [2007]). See Table 3.7 for a comparison between these two positions in literature.

It is demonstrated for composite materials that shear modulus in the plane perpendicular to the direction of fibers is highly affected if the number of interfaces number is increased (Dasgupta and Bhandarkar [1992]). In bone, cement lines could act as a mechanism of energy dissipation through damage generation. In the work of Nobakhti *et al.* [2014] the behavior of a cement line in cortical bone is analyzed with a three-dimensional model and it can be concluded that in a bending load case, interfaces increase strains but decrease stresses.

In Table 3.8 some elastic properties in literature used in this Thesis are listed.

Table 3.8: Elastic properties of cement line in literature

Author	E	ν
Prendergast and Huiskes [1996]	6 GPa	0.25
Ascenzi *et al.* [2013]	3.29 GPa	0.3
Li *et al.* [2013] (2013)	9.64 GPa	0.3
Nobakhti *et al.* [2014]	88.5 ± 22.42 MPa	0.3

3.4 Fulfilment of thermodynamic restrictions

In order to fulfill thermodynamic principles, the compliance and stiffness matrices have to be positive definite, see e.g. Gurtin [1973]. Hence, this condition implies that the elastic constants of the stiffness matrix have to verify some relationships.

Lempriere [1968] expressed these relationships for an orthotropic material as follows:

$$E_{11}, E_{22}, E_{33}, G_{23}, G_{31}, G_{12} > 0 \tag{3.32}$$

$$|\nu_{21}| < \left(\frac{E_{22}}{E_{11}}\right)^{0.5} |\nu_{12}| < \left(\frac{E_{11}}{E_{22}}\right)^{0.5} \tag{3.33}$$

$$|\nu_{13}| < \left(\frac{E_{11}}{E_{33}}\right)^{0.5} |\nu_{31}| < \left(\frac{E_{33}}{E_{11}}\right)^{0.5} \tag{3.34}$$

$$|\nu_{23}| < \left(\frac{E_{22}}{E_{33}}\right)^{0.5} |\nu_{32}| < \left(\frac{E_{33}}{E_{22}}\right)^{0.5} \tag{3.35}$$

$$1 - \nu_{21}\nu_{12} - \nu_{13}\nu_{31} - \nu_{32}\nu_{23} - 2\nu_{12}\nu_{31}\nu_{23} > 0 \tag{3.36}$$

$$1 - \nu_{13}\nu_{31} > 0 \tag{3.37}$$

$$1 - \nu_{21}\nu_{12} > 0 \tag{3.38}$$

$$1 - \nu_{32}\nu_{23} > 0 \tag{3.39}$$

$$\nu_{21}\nu_{32}\nu_{13} < \frac{1 - \nu_{21}^2\left(\frac{E_{11}}{E_{22}}\right) - \nu_{32}^2\left(\frac{E_{22}}{E_{33}}\right) - \nu_{13}^2\left(\frac{E_{33}}{E_{11}}\right)}{2} < \frac{1}{2} \tag{3.40}$$

Additionally, from the symmetry of the compliance matrix we have:

$$\frac{\nu_{12}}{E_{11}} = \frac{\nu_{21}}{E_{22}}; \quad \frac{\nu_{13}}{E_{11}} = \frac{\nu_{31}}{E_{33}}; \quad \frac{\nu_{23}}{E_{22}} = \frac{\nu_{32}}{E_{33}} \tag{3.41}$$

In a technical note by Cowin and Van Buskirk [1986], these thermodynamic restrictions are summarized and they were used to verify the elastic constants of bone obtained by Ashman *et al.* [1984] through ultrasound techniques.

As mentioned above, a wide range of crystal platelet dimensions can be found in the bibliography. When Halpin-Tsai equations are used to estimate theoretically elastic constants of a mineralized collagen fibril for typical constituent properties (Wagner and Weiner [1992]; Akiva *et al.* [1998]), one should pay attention to the values of crystal aspect ratios, L/T and W/T , because not all the possible crystal aspect ratios verify the thermodynamical restriction summarized before.

In Vercher *et al.* [2014] a detailed study of the influence of the aspect ratios on the elastic constants is presented for Halpin-Tsai equations, and the range of aspect ratios that fulfill the thermodynamic restrictions is provided. In Fig. 3.22 a results summary of the dimension ranges that fulfill the thermodynamic restrictions is presented. Combinations of aspect ratios that are not given in the ranges of Rubin *et al.* [2003] are indicated in the table by "out-of-range values". It can be observed that only a small range of values satisfies simultaneously all thermodynamic restrictions when Halpin-Tsai equations are used. Therefore, the Halpin-Tsai equations must be used with caution for certain constituent properties.

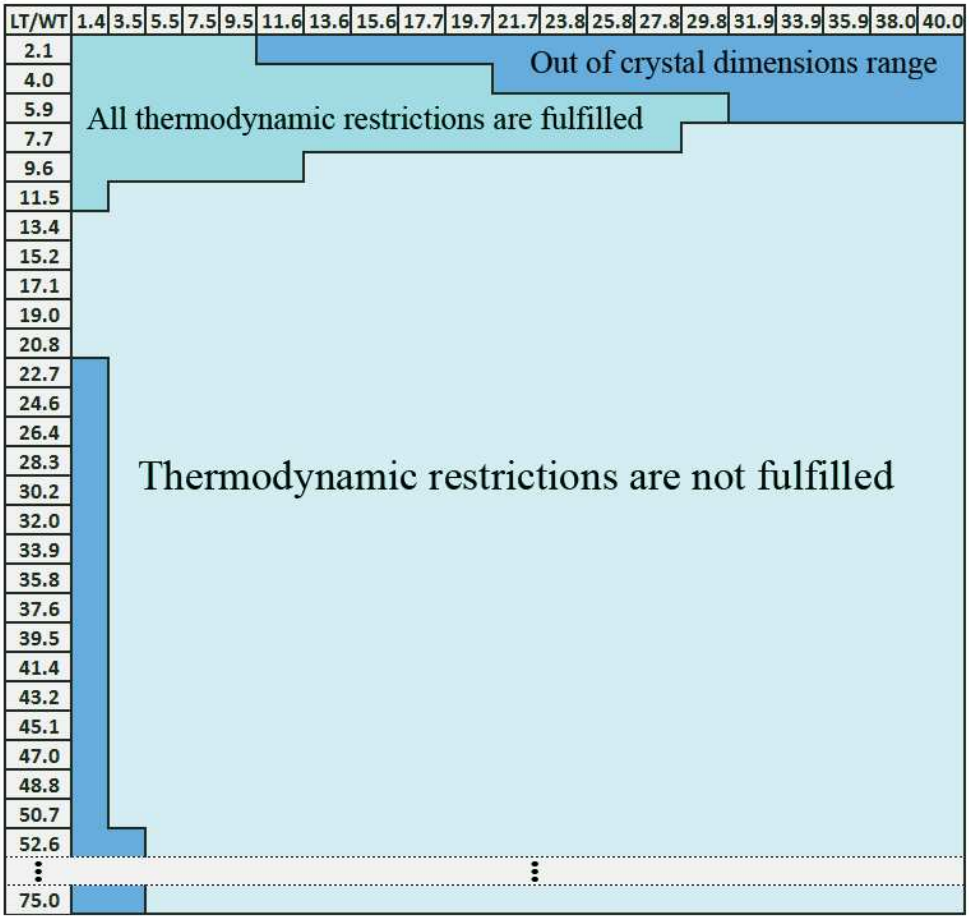

Figure 3.22: Results summary for all thermodynamic restrictions when Halpin-Tsai equations are applied (Vercher *et al.* [2014]). $LT = L/T$ and $WT = W/T$. Constituent properties are taken from Akiva *et al.* [1998].

Chapter 4

Strength properties of cortical bone

4.1 Introduction

In the literature about experimental tests in order to characterize the strength properties of cortical bone, the contribution of Ascenzi *et al*. is remarkable not only for the quantity of works but for the innovation at that time in developing tools and methods. These methods allowed to explain for the first time some phenomena at small scales of bone and particularly for osteons. These authors achieved the isolation of osteons in form of cylindrical microsamples and subjected them to numerous mechanical tests (Ascenzi and Bonucci [1967, 1968, 1972]; Ascenzi *et al.* [1973]; Ascenzi [1988]).

As a first approach of this Thesis, the modeling of an isolated osteon is an aim, and thus, the works of Ascenzi *et al*. are a reference and an experimental support in order to validate the models.

In Ascenzi *et al.* [1973] the osteon is analyzed under compressive loads. The sketch in Fig. 4.1 shows the simple configuration used, in which a section of an osteon

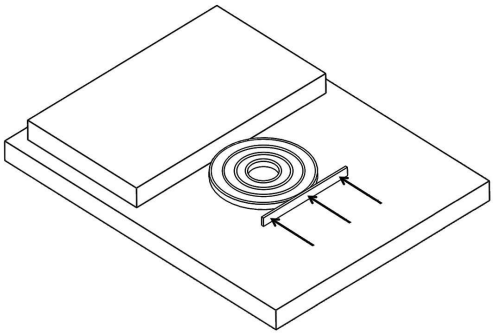

Figure 4.1: Radial compressive loading test by Ascenzi *et al.* [1973].

(30-40 μmm thick) is placed on a slide and pressed against the side of a coverslip (160 μm thick) using a spatula, thus being subjected to radial loading. In the work by Ascenzi *et al.* [1973] detailed indications about the experimental procedure are provided. In a previous work, Ascenzi and Bonucci [1968] also described the procedure followed to extract microsamples of single osteons from cortical tissue. Due to the sample extracting procedure, the osteon geometry can be assumed to be cylindrical in practice. In fact, the authors selected those osteons whose geometry was essentially circular on a transverse plane.

We will focus on the dominant type of osteon that can be found in the cortical tissue of long bones, named type I in Ascenzi *et al.* [1973]. Its main feature is an alternated lamellar arrangement, sketched in Fig. 4.2: lamellae with fibrils essentially aligned in the axial direction of the osteon alternated with lamellae whose fibrils are mainly aligned in the circumferential direction. Here, the authors suggest that fibrils in one lamella make an angle of nearly 90° with the fibrils in the next. Ascenzi and Bonucci arrived to this conclusion by observing the osteons under polarized light, which exhibits an alternate pattern, and the corresponding correlation with electron microscopy.

In addition, the authors referred that the fibrils of the innermost and outermost lamellae are essentially oriented in a circumferential direction (Ascenzi *et al.* [1973]). We note in passing that the cement line (1 μm thick) is not considered in the single osteon models of this Thesis because it is expected that this layer was fully damaged or eliminated during the osteon extraction process. In their work, these authors also

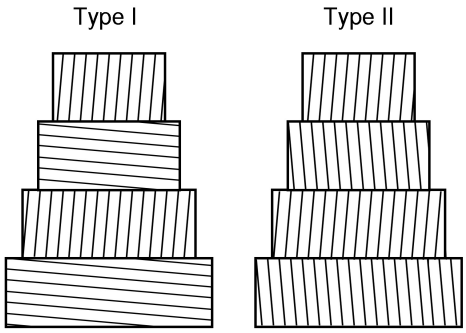

Figure 4.2: Sketch of the laminated structure of osteon types I and II, following Ascenzi *et al.* [1973].

consider another type of osteon (type II), with lamellae showing a spiral course fibril arrangement, close to the axial direction of the osteon (see Fig. 4.2). Even in this type of osteon, Ascenzi and Bonucci reported that fibrils of the innermost and outermost lamellae are essentially oriented in a circumferential direction. The principle of having alternated lamellae and the more recent sublayered lamellar structure proposed by Weiner *et al.* [1999] are both assumed in this Thesis.

Experimentally, and for type I osteons (the type analyzed in this work), we can verify that the application of a compressive radial load leads to the generation of microcracks in circumferential direction, as described in a comprehensive way by Ascenzi *et al.* [1973]. These authors reported the following experimental evidences:

- Microcracks are circumferential and they appear mainly in the lamellae whose fibrils are aligned in the axial direction of the osteon (longitudinal lamellae). Some of them are located along the interfaces of the lamellae. In addition, microcracks extend through the whole thickness of the analyzed section.
- Microcracks begin in the longitudinal lamellae that are near the haversian canal.
- Microcracks appear in the four quadrants and concentrate in circular sectors located in a region between 20°and 50°with respect to the loading direction.
- The lamellae with fibrils essentially arranged in the circumferential direction (transverse lamellae) do not show apparent damage in this process. Fig. 4.3

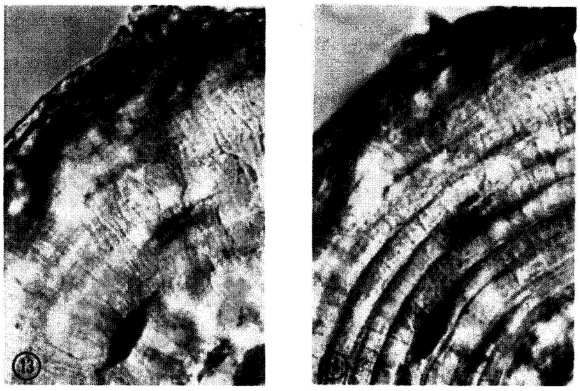

Figure 4.3: Behavior under compressive load of an osteon type I: left, before loading; right, after loading, showing the generation of microcracks by Ascenzi *et al.* [1973].

shows a portion of a tested osteon before the load application (left) and under the application of the load that causes the circumferential microcracks (right). Further analysis with electron microscopy shows that the microcracks within the longitudinal lamellae advance through the interfibrillar substance (that acts as a matrix), indicating that the strength of this substance is clearly lower than the fibril strength.

Recently, Ebacher *et al.* [2012] also carried out experimental tests by compressing a portion of cortical tissue in the radial direction. Their results are in full agreement with those observed by Ascenzi *et al*. From all the above experimental observations, it can be inferred that the matrix failure that appears in the longitudinal lamellae is caused by either a normal tensile traction that acts in the radial direction, or a shearing traction, or a combination of both. This behavior is analogous to the delamination processes that can be found in structural fiber reinforced composite materials due to the existence of interlaminar stresses. This will be verified by the numerical analyses presented in Chapter 6.

4.2 Strength properties of an osteon

One of the load conditions analyzed in this Thesis (compressive diametral loading of the osteon) is essentially an in-plane loading state. It is expected that the failure is governed by the plane stress state shown in Fig. 3.14 in regions where circumferential (or hoop) $\sigma_{\theta\theta}$, radial σ_{rr} or shear $\sigma_{r\theta}$ stresses are large compared to their respective strength limits. Following customary terminology in structural composite materials, the circumferential stress σ_{rr} can be considered an intralaminar stress, whereas σ_{rr} and $\sigma_{r\theta}$ correspond to interlaminar stresses that cause eventual delamination.

It is also expected that the thick lamellae exhibit a low strength to these stresses, because the mineralized collagen fibrils are essentially aligned in the out-of-plane direction (i.e. the osteon z-axis direction, see Fig. 3.14). For thick lamellae and for in-plane loads, the interfibrillar matrix is the main load-bearing material and its relative low strength can lead to matrix microcracking. This is in accordance with the experimental evidences commented in Chapter 2 and is verified numerically in the following chapters.

As explained in the background Chapter 2, in the works by Ascenzi and Bonucci [1967, 1968, 1972] extensive experimental testing on isolated osteons to characterize the tensile, compressive and shear properties are carried out. In this Thesis and previous works of the research group, we estimate the strength properties from Ascenzi and Bonucci's tests on osteons subjected to tensile load in the osteon z-axis and from shear tests performed by application of a punch centered on the osteon in the z-axis. From all available data, we have considered the results for 25-30 year-old donors with a high calcification degree, determined by microradiography and tested on wet conditions. Osteons with a high calcification degree are stiffer, stronger and with a more linear elastic behaviour up to rupture than those with low calcification (Ascenzi and Bonucci [1972]).

It is well known that the stiffness and strength properties depend not only on the calcification degree, but also on the humidity condition and age (Ascenzi *et al.* [1973]). The change in tensile stiffness and strength in the axial direction due to humidity is very significant, being larger for dry samples than for wet samples. The effect of the calcification degree is not so important although, as expected, it is shown that the

stiffness and strength values are smaller for a low calcification degree. Finally, the influence of age is not so considerable.

Despite the fracture planes intersected some lacunae in their experimental tests, it is worth remarking that in Ascenzi and Bonucci [1967, 1972], the authors did not find a clear evidence that may correlate the lacunae density with the tensile or shear strengths. Note that cortical bone exhibits a considerable inelastic deformation, relaxing stress concentrations and increasing its toughness (Ebacher *et al.* [2012]). It is often suggested that the strain amplification at the osteocyte lacunae increases the strain perceived by the osteocytes and the subsequent bone remodelling signaling e.g. Prendergast and Huiskes [1996]; Ascenzi *et al.* [2004].

4.2.1 Strength properties of thick and thin lamellae

Circumferential tension strength

Given the fibril arrangement in the thin lamellae (see Fig. 3.14), the circumferential tensile strength of the thin lamellae must be clearly greater than for thick lamellae, i.e. $S^{\text{thin}}_{\theta\theta,\text{t}} > S^{\text{thick}}_{\theta\theta,\text{t}}$. As expected, Ascenzi and Bonucci reported that the maximum stiffness and strength for an osteon loaded in the axial z-axis is found for type II osteons (following the nomenclature of Fig. 3.14) (Ascenzi and Bonucci [1967]). With the exception of the innermost and outermost lamellae, type II osteons have lamellae oriented mainly in the axial direction of the osteon. The strength value of this type of osteons loaded in a tensile test was reported as 120 MPa in Ascenzi and Bonucci [1967] (for a dry condition, this value increases up to 193 MPa). Therefore, it seems reasonable to assume that the strength of a sublamella loaded in the fibril direction is about this value. Hence, the circumferential tensile strength of thin lamellae will be estimated as $S^{\text{thin}}_{\theta\theta,\text{t}}$=120 MPa.

The estimation of the circumferential tensile strength for the thick lamellae is more elusive. From tensile tests carried out in the z-axis for type I osteons, Fig. 4.2, we have considered in this work that the onset of the failure of the weakest lamellae under the tensile test corresponds to a clear depart from the linear response in a σ–ϵ diagram. These diagrams are available in the work by Ascenzi and Bonucci [1967] for

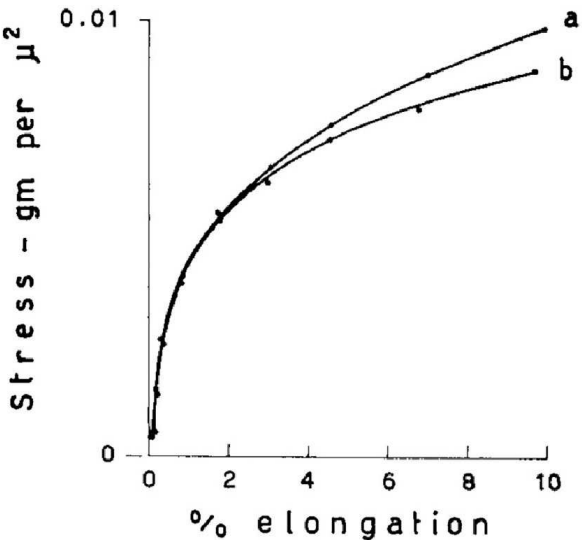

Figure 4.4: Stress strain curves for tensile tests in the z-axis of single osteons by Ascenzi and Bonucci [1967]. Curve (a) corresponds to a wet and fully calcified type I osteon,taken from a 30 years old man. Curve (b) same from a 80 years old man. Note: 1 gr $/\mu^2 \approx 10^4$ MPa.

type I osteons. Under a tensile test in z–axis for type I osteons, the first failure will occur for lamellae whose fibrils are orientated perpendicularly to the loading direction and this will introduce a loss of linear behaviour in the σ–ϵ response. This value has been estimated in an approximated way from Fig. 4.4, reproduced from Ascenzi and Bonucci [1967], and is about 50 MPa, that can be assumed to be the strength of a thin lamella when loaded in the osteon z–direction. We make a further assumption by considering that this strength is equal to the strength of a thick lamella when loaded in the circumferential direction and hence $S^{\text{thick}}_{\theta\theta,\text{t}}$=50 MPa.

Radial tensile strength

A tensile failure in the radial direction is an interlaminar failure that implies the fracture of the interfibrillar matrix without affecting the mineralized collagen fibrils. Therefore, the radial tensile strength will be approximately the same for all sub-lamellae or their grouping into either thin or thick lamellae. Thus, we can write $S^{\text{thin}}_{rr,\text{t}} \approx S^{\text{thick}}_{rr,\text{t}}$ and it will simply denoted as $S_{rr,\text{t}}$. Since this failure mode is similar

to the failure mode of a thick lamella loaded circumferentially (both modes imply the damaging of the interfibrillar matrix), it is reasonable to assume that $S_{rr,\mathrm{t}} \approx S^{\mathrm{thick}}_{\theta\theta,\mathrm{t}}$ = 50 MPa. When no better estimates are available, this hypothesis is also usual in the analysis of delamination of structural composite materials (Brewer and Lagace [1988]).

Shear strength

Ascenzi and Bonucci carried out shear tests by micropunching the center of osteons in the axial direction (Ascenzi and Bonucci [1972]). This type of test led to the separation, almost cylindrical, of a set of inner lamellae with respect the outer. Their results show that the shear stiffness and strength depend slightly on the type of osteon (I or II): the shear strength $S_{s,mpunch}$ varies between 56 MPa for type I and 46 MPa for type II. It can be assumed that the shear strength of a thick lamella in the $r-z$ plane (see reference system in Fig. 3.14) under the micropunch test is similar to the shear strength in the plane r-θ of a thin lamella. Therefore, we will assume that $S^{\mathrm{thin}}_{r\theta,\mathrm{s}} = 46$ MPa.

The shear strength in the plane r-θ for thick lamellae must be clearly lower than 46 MPa, since this shear mode does not involve the shearing of mineralized fibrils, which are essentially normal to the plane r-θ. The shearing failure will involve mainly shearing of the interfibrillar matrix. This value has been estimated as $S^{\mathrm{thick}}_{r\theta,\mathrm{s}} \approx 20$ MPa.

It is worth emphasizing that the estimated values given above must be considered as a first approximation, being the deviations large in practice due to several factors, such as calcification degree or water content. Another aspect not considered here is the variation of properties from inner lamellae to outer lamellae, which has been reported for elastic behaviour, e.g. in Faingold *et al.* [2012]. The literature on strength properties is scarce and further research is necessary to have better characterization of the strength properties of these tissues.

Table 4.1: Strength values by Ascenzi *et al.* [1973] and specific fracture energies in the transversal plane (normal to the osteon axis) used for osteon, interstitial tissue and cement line by Li *et al.* [2013].

$S_{u,osteon}$ shear	$S_{u,osteon}$ radial	$G_{I,osteon}$	$G_{I,inter}$	$G_{I,CL}$
20 MPa	47 MPa	860 N/m	238 N/m	146 N/m

4.3 Strength properties of cement line and interstitial tissue

Damage simulation in cortical bone is a very complex problem that depends on multiple variables that increase as the structural scale is reduced. The strength properties are more difficult to determine from different tests than elastic properties, because some properties as humidity, age, mineralization and more can change for each sample.

In this work we used the strength properties indicated in Table 4.1. For osteons (lamellae) the strength values are taken from the works by Ascenzi *et al.* where numerous tests were made on isolated osteons (Ascenzi *et al.* [1973]). We focused on results of tensile and shearing punching tests both in the osteon longitudinal direction. For this study we have considered high mineralization data measured for human femur of 25-30 years old and tested under humid conditions. The osteons with high calcification degree have high values of stiffness, strength and a more lineal elastic behavior to failure than the ones with low degree of mineralization (Ascenzi *et al.* [1973]).

The bibliography for strength estimation of properties for interstitial bone and cement lines is scarce. Numerous studies of failure and fatigue tests on cortical bone conclude that the strain energy release is higher at osteons and lower at cement lines, being this closer to interstitial tissue values (Li *et al.* [2013]).

Tensile works from Rho *et al.* [2001] show evidence that osteons have 30% less strength values than interstitial tissue. In Burr *et al.* [1988] there is a reference of works from Aoji *et al.* showing that for compression cases strength of bone is inversely proportional to the quantity of interstitial bone. The works of Chan and Nicolella

[2012] and Ritchie *et al.* [2005] report some experimental data of strain energy release for osteons, interstitial tissue and cement lines. Due to the gaps in data and taking into account the previous ideas, we propose a proportional relation that relates the strength properties and the specific fracture energies for osteon, interstitial bone and cement line. We assume a given geometry with a crack longitude a and the same geometry and crack are supposed for the osteon and interstitial materials.

The objective of this Section is to calculate $S_{u,inter}$ and $S_{u,CL}$ given the values in Table 4.1.

For mode I fracture, the ultimate tensile strength for a given crack a, for each material (osteon and interstitial tissue) is:

$$\sigma_{c,osteon} = \frac{K_{Ic,osteon}}{C\sqrt{\pi a}}; \qquad \sigma_{c,inter} = \frac{K_{Ic,inter}}{C\sqrt{\pi a}} \tag{4.1}$$

where K_{Ic} is the critical stress intensity factor or fracture toughness and C is the geometrical factor. From 4.1 we have:

$$\frac{\sigma_{c,osteon}}{\sigma_{c,inter}} = \frac{K_{Ic,osteon}}{K_{Ic,inter}} \tag{4.2}$$

On the other hand, the strain energy release rate G is related to the stress intensity factor for mode I fracture, as follows:

$$G_I = \frac{(K_I)^2}{E'} \tag{4.3}$$

where E' is related to Young's modulus (depending on a plane stress or plane strain condition) although this is not relevant in the following analysis.

Although $\sigma_{c,osteon}$ and $\sigma_{c,inter}$ are ultimate tensile stresses for a given crack length, it looks reasonable to keep this relationship for the general strength values under the hypothesis of linear elastic fracture mechanics:

$$\frac{S_{u,osteon}}{S_{u,inter}} \approx \frac{\sigma_{c,osteon}}{\sigma_{c,inter}} \approx \frac{K_{Ic,osteon}}{K_{Ic,inter}} \approx \sqrt{\frac{G_{Ic,osteon}}{G_{Ic,inter}}\frac{E_{osteon}}{E_{inter}}} \tag{4.4}$$

Table 4.2: Strength properties for cement line calculated using Eq. 4.6

E_{CL}	A	$S_{u,CL}^{\text{shear}}$	$S_{u,CL}^{\text{normal}}$
3.29 GPa	7.60	2.99 MPa	7.03 MPa
6.0 GPa	4.17	4.04 MPa	9.48 MPa
9.64 GPa	2.6	5.11 MPa	12.01 MPa

Since the Young's modulus of the interstitial tissue is about 10% greater than the osteon modulus, we can write:

$$\frac{S_{u,osteon}}{S_{u,inter}} \approx \sqrt{\frac{G_{Ic,osteon}}{G_{Ic,inter}} \frac{E_{osteon}}{E_{inter}}} = \sqrt{\frac{G_{Ic,osteon}}{G_{Ic,inter}} 1.10} \tag{4.5}$$

where osteon properties and strain energy release rate of interstitial tissue are known (see Table 4.1) and the strength value $S_{u,inter}$ is calculated using Eq. 4.5.

In order to estimate the strength of the cement line $S_{u,CL}$ and taking into account the elastic properties from Subsection 3.3.1, we perform a similar calculation:

$$\frac{S_{u,osteon}}{S_{u,CL}} \approx \sqrt{\frac{G_{Ic,osteon}}{G_{Ic,CL}} \frac{E_{osteon}}{E_{CL}}} = \sqrt{\frac{G_{Ic,osteon}}{G_{Ic,CL}} A} \tag{4.6}$$

were A is the ratio of osteon and cement line modulus. For CL we have taken three values for E_{CL} from bibliography (Chapter 2), yielding result values for the ultimate strength of the CL in the normal direction in the range 7.03-12.01 MPa (see Table 4.2). An analogous procedure is followed to predict $S_{u,CL}^{\text{shear}}$.

Chapter 5

Introduction to FEM in bone analysis

The finite element method is a very useful technique for mechanical simulation and structural analysis. Nowadays it is the most used technique, not only for the linear elasticity problem in structural analysis, but also for plasticity, electromagnetism, heat transfer, etc. The FEM is a very flexible tool that can be applied in a vast amount of engineering applications and in a wide variety of materials. As it has been explained in previous chapters of this Thesis, the finite element method can be applied to study the mechanical behavior of bone from the smallest structural hierarchical level as can be the unitary cell of the mineralized collagen fibril, as to the macrostructural level of the whole skeletal system.

After obtaining the elastic and strength material properties, the aim of the following sections and chapters is to apply the finite element method to analyze the mechanical behavior of cortical bone from the model of a single osteon with simplified geometry to a system composed of osteons, interstitial tissue and cement lines with realistic geometries and both for two-dimensional and three-dimensional models.

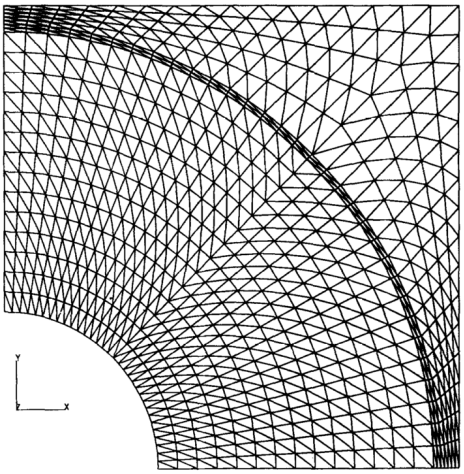

Figure 5.1: Finite element mesh for hollow three-component quarter-fiber model by Hogan [1992].

In literature there are interesting works regarding the modeling of cortical bone at osteonal level. One of first numerical microstructural models in bone was proposed by Hogan [1992], who modeled the cortical bone at microstructural level with the finite element model of Fig. 5.1. This model is an extension of micromechanical 2D techniques used in structural fiber-reinforced composites where osteons act like fibers and interstitial tissue as matrix. The cement line is defined as the interface between these two. The prediction of macroscopic properties through the model is well correlated with experimental data, although the big dependence of constituent material properties is recognized.

Prendergast and Huiskes [1996] also proposed a 2D finite element model of an osteon, (Fig. 5.2) considering the main morphology details in a cross-section (Haversian canal, concentric lamellae, cement line and lacunae, also including interstitial matrix surrounding the osteon). In their work, the model is used to evaluate the strains in lacunae under the presence of microcracks (some authors suggest that bone regeneration mechanisms are related to the changes of size and local strains near lacunae acting as sensors in the process).

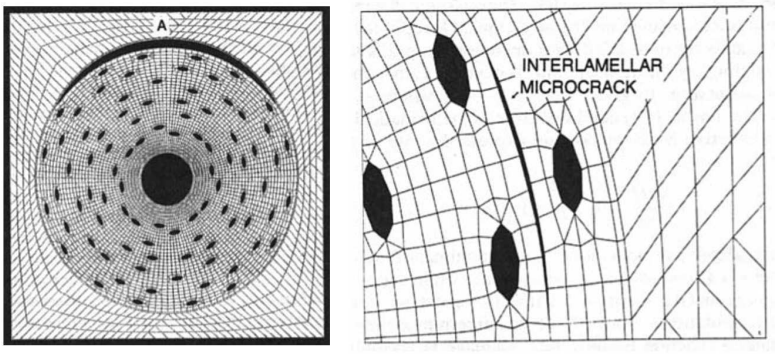

Figure 5.2: Left: 2D finite element model of a osteon by Prendergast and Huiskes [1996]. Right: *ad hoc* inclusion of microcracks.

More recent works as the proposed by Ascenzi *et al.* [2013] analyse the mechanical behavior of bone with a complete three-dimensional multiscale model with patient-specific material properties presented with experimental validation at each structural level (micro-macro), where mechanical response is predicted in order to analyze strains under physiological loading conditions for long bones. In Fig. 5.3 we can see the microstructural model where 6-node-wedge and 8-node-brick elements were used to mesh the interstitial bone and 8-node-brick elements and 20-node-brick elements to mesh the osteon. The interstitial bone model has an hexahedron dominated mesh due to the complexity of the geometry to fit with osteons geometry.

In other works of Maria-Grazia Ascenzi *et al.*, the lacunar distribution and fibril orientation is analyzed from experimental data. Numerical scripts for random modeling according to experimental distribution are developed to investigate how orientation relates to strains and stresses during mechanical testing (Ascenzi and Lomovtsev [2006]; Ascenzi *et al.* [2008]).

5.1 Bone failure and damage background

It is known that both cortical and trabecular bone have the property of noticing the presence of microcracks and other kind of damage and replace these regions with

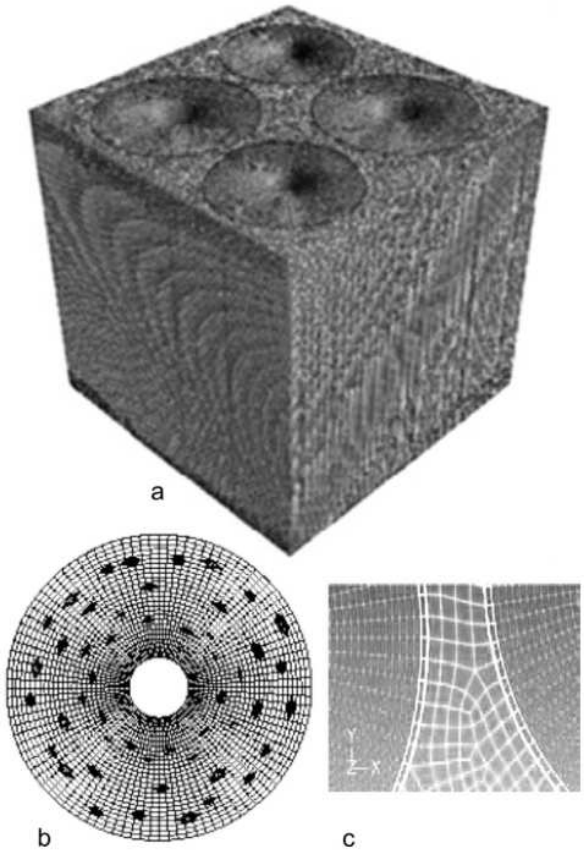

Figure 5.3: Micro-FE model by Ascenzi *et al.* [2013]. (a) This 0.5 mm model contains four heterogeneous osteon models with (b) osteocyte lacunae viewed in cross-sections. The models of cement lines (c) at the interface with interstitial bone model are also included.

new material. This mechanism is triggered by the presence of microdamage (one of the factors for bone remodeling) and it allows naturally to optimize the geometry and bone mass. The analysis of these mechanisms is of great importance in healing of bone fractures, implants, bone degeneration with age and bone diseases. The biomechanical treatment of the problem has given place to a vast literature in the past decades given the importance of the problem and its social transcendence, but still there are many aspects unknown (Cowin [2001]). As previously mentioned, this Thesis is focused on the microstructural and sub-microstructural levels of cortical bone.

There are different methods to simulate failure in quasi-fragile materials as cortical bone. With the finite element method different techniques can be applied for explicit and implicit crack propagation; in the fracture mechanics context the cohesive zone models (CZM), applied in structural mechanics can be extended to the biomaterial field after a convenient adaptation and setup (Yang *et al.* [2006]; Cox and Yang [2007]). Some models and fracture toughness calculations for cortical tissue have been achieved under the linear elastic fracture mechanics (LEFM) although it is starting to be admitted that LEFM does not give an exhaustive and complete description and it is not sufficiently consistent (Yang *et al.* [2006]; Cox and Yang [2007]).

The CZM have begun to be implemented to the analysis of cortical bone tissue (Yang *et al.* [2006]) and have the advantage of giving the possibility to consider the situation of "no damage" and locate the damage progressively depending on whether the critical values defined when the failure criterion is achieved. In addition, consideration of such nonlinear models is a valid alternative, since it is only possible to apply LEFM when cracks are much greater than a certain length (Bažant [2002] indicates $D/l \geq 100$, where D is the cross-section dimension and l the characteristic fracture zone length), in the human cortical bone case crack lengths ranging from 3 to 10 mm according to Yang *et al.* [2006]; Cox and Yang [2007]. Another disadvantage of the LEFM is that it assumes the existence of an initial crack. By contrast, CZM can be applied in the vicinity of notches or stress concentrators.

The CZM models formulated through cohesive interface elements (zero thickness) are also suitable in situations where it is possible to define a priori the location of cracks and their potential propagation path (e.g. adhesive bonding and delamination in laminated analysis (Turon *et al.* [2007])), as it is required to set the cohesive elements in the mesh. For cortical bone microstructure these elements could be introduced at the interfaces between osteon lamellae and interstitial matrix and also in the cement

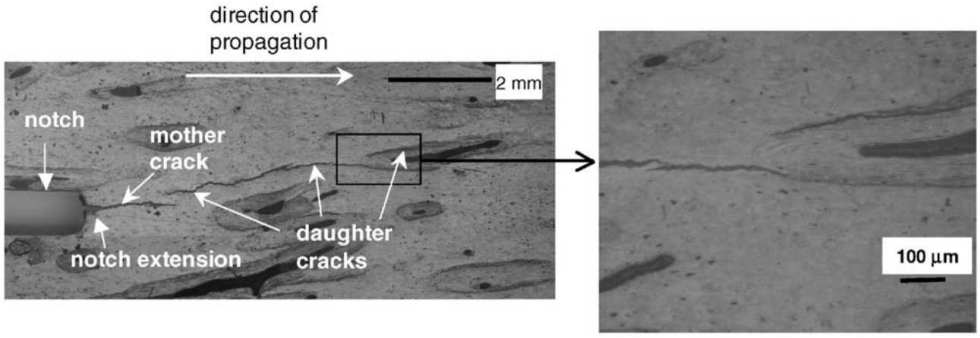

Figure 5.4: An optical micrograph of a crack in 34-year-old human cortical bone. Note the formation of daughter cracks and corresponding uncracked ligaments, by Yang *et al.* [2006].

line, since experiments show that the microcracks tend to start between the lamellae and progress along the cement line when are reached (see Fig. 5.4).

The works that exemplify the implementation of the CZM to bone tissue models are relatively recent. Ural and Vashishth [2006]; Ural [2009] and Yang *et al.* [2006] have applied models of cohesive fracture to the behavior of cortical bone from a macroscopic point of view, relating it to the fracture toughness of the material from tests on compact-tension (CT) specimens collected in literature or to fracture modeling of bone. Additionally, Tomar [2009] applied the cohesive model to trabecular bone and Ichim *et al.* [2007] to dentin and enamel.

Other authors combine the use of failure modes in structural components with X-FEM introducing discontinuities of displacements in a FE mesh and simulating the separation between crack faces with the possibility of incorporating additional terms for modeling singular fields of LEFM surrounding the crack tip. This methodology is not commonly used in the modeling of microstructural biomaterials because of the complexity of the models that promote the use of alternative techniques for predicting the failure propagation. Between the works that incorporate X-FEM to the micromechanical failure of cortical tissue, the works by Budyn and Hoc [2007] are remarkable although in the context of LEFM. This model (see Fig. 5.5) presents some deficiencies derived from the X-FEM standard approach: it is assumed that crack initiation is at Haversian canals due to stress concentration from geometry (when it

is well known that cracks initiate principally between interfaces as cement lines or interstitial lamellae (O'Brien *et al.* [2003, 2005]; Nalla *et al.* [2005])).

There are two distinct approaches for damage study (Taylor *et al.* [2007]): the first one is based on damage mechanics, modeling the system as a continuum, assuming that the quantity of damage over a region grows as function of a local parameter, as can be the strain energy density. The second approach is the mechanistic and regards to the microstructural details trying to explain the complex mechanisms behind micro damage processes. The latter the one selected in this Thesis and it can be useful to develop numerical models of the mechanical behavior of microstructure that include the explicit presence of microcracks.

There is consensus in the literature (Taylor *et al.* [2007]; Yang *et al.* [2006]; Vashishth [2007]) that two modes of microdamage can be identified at cortical bone: on one hand the existence of microcracks (with size between 50 and 200 μm) and on the other hand the presence of diffuse microdamage that is at the same level of mineralized collagen fibers, associated with a lower hierarchical scale. The mechanisms that relate the level of microdamage with a higher risk of fracture are not still well defined, but the relation between these levels and a higher degradation of tissue toughness results unquestionable (Yang *et al.* [2006]). Taylor *et al*. have developed numerous works regarding the relationship between microstructure and microcracks in cortical bone. It has been proved that for the most of microcracks, osteons and cement lines act like growing barriers (O'Brien *et al.* [2003, 2005]). Only for microcracks large enough this barrier is exceeded, where osteons present less strength for growing. In O'Brien *et al.* [2003] there is a study of accumulation, distribution and microcracks spreading as result of fatigue tests, describing a model for the simulation of fatigue processes.

From a mechanical point of view, the cortical tissue belongs to the vast group of quasi-fragile materials (Hambli *et al.* [2012]). The failure of these materials is usually preceded by the formation of a certain type of distributed damage. This is the case of concrete, rocks, polymers, plastic fiber reinforced composites, etc. in addition to other biomaterials.

The growing and coalescence of cracks and diffuse damage leads to a gradual generation of highly located damage zones that act as precursors of fracture at macroscopic level.

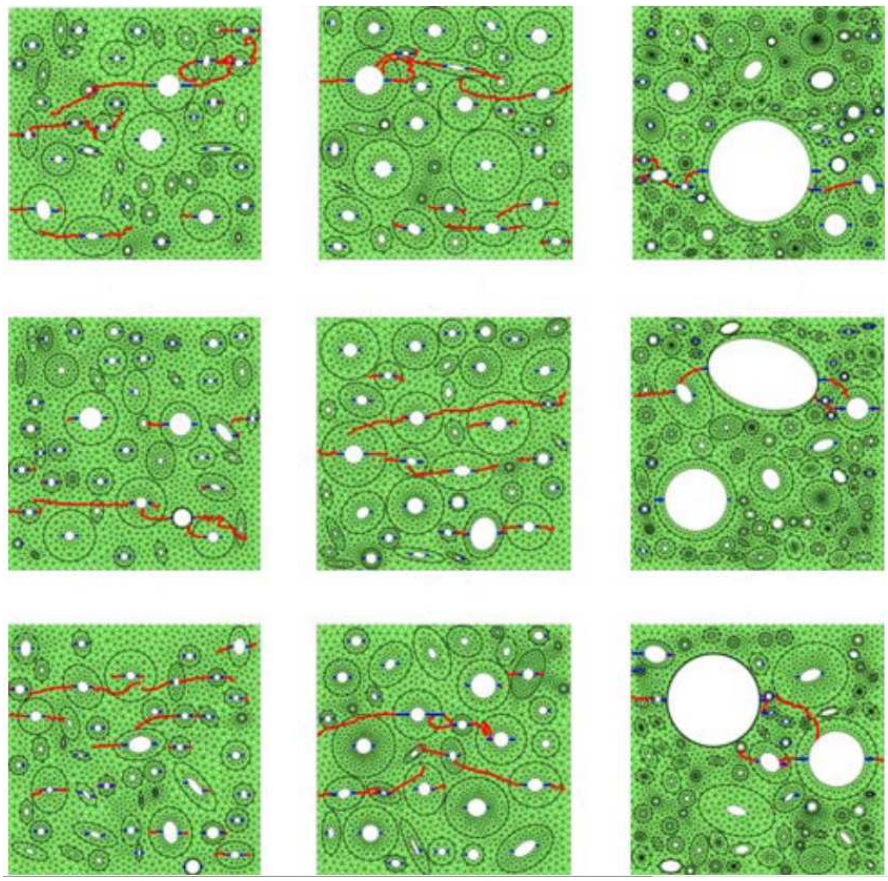

Figure 5.5: Crack propagation for different X-FEM model configurations of cortical bone by Budyn and Hoc [2007].

Prendergast and Huiskes [1996] also consider degradation phenomena of material stiffness in the zones of high strains. The deficiency of the model is that it does not predict the initiation of cracks or degradation zones but it includes them *ad hoc* between the lamellae and the cement line (Fig. 5.2) in order to evaluate their effect. The degradation is included by simple modification of Young's modulus of elements near lacunae. To improve this limitation is one of the objetives of this Thesis.

The progressive damage technique in FEM appeared from the necessity of more accurate and less computational expensive methods to evaluate the damage tolerance for the composite material elements used in aeronautic industry.

The bases of the damage tolerant methodology are the knowledge of mechanical behavior of composite materials, including the mechanisms and progression of failure. With that aim, some computational and analytical tools have been created, in order to predict the progression of damage in more advanced stages than initiation or first ply failure (FPF). These tools usually used a material properties variation. The most commonly used methods at present are the material properties/stiffness degradation method (known as MPDM) and the element failure method (EFM) (Tan and Nuismer [1989]; Tan [1991]; Tan and Perez [1993]). In both cases it is important to choose an appropriate failure criterion for each model because the degree of precision with respect to experimental tests will depend on its implementation.

Two of the most recent damage theories applied to composite materials are the multicontinnum theory (MCT) (Mayes and Hansen [2004]) and micro-mechanical failure (MMF) (Ha *et al.* [2008]). These theories have important differences with respect to less recent criteria as Tsai-Wu, because incorporate micromechanical aspects and differentiate between fiber or matrix dominated modes of failure (Tay *et al.* [2008]). Both MCT and MMF evaluate the composite failure based on constituent stresses (fiber and matrix), but are based on different methods to calculate stresses. The MCT uses phase averaging while MMF uses representative elementary models of fiber and matrix.

For progressive damage, both methods (MCT and MMF) can be implemented in finite element codes with procedures as element-failure algorithm (Tay *et al.* [2003]) or stiffness degradation (Chang and Chang [1987]). In this latter some values of material stiffness are reduced when the failure of the composite has been reached according with the corresponding mode. That fact requires that the code recalculates

the element and global stiffness every time that an element fails. In the element-failure method, the damage is modelated directly from manipulation of nodal forces of the element that fails instead of modifying the stiffness. This way some convergence problems can be avoided. In Tay *et al.* [2009] a composite analysis with failure and reparation is developed, the model is done in Abaqus and a subroutine is used for implementing degradation (in this case the stiffness degradation method is used) based on the micromechanical damage criterion (MMF). In Hou *et al.* [2000] some damage criteria are implemented for laminates using the finite element code DYNA3D, where an impact test is simulated.

5.1.1 Stiffness degradation method (MPDM)

This method consists in modeling the material degradation that starts after an initial failure is reached in one of the elements of the mesh. This degradation is achieved by reduction of the material properties. In this way, through implementation of field variables (sometimes are also called degradation constants) it is possible to simulate the propagation of failure of failed elements. For example, a two-dimensional plane-stress model proposed by Tan and Nuismer [1989]; Tan [1991]; Tan and Perez [1993], the field variables for properties degradation are D_i in Eq. 5.1. It is important to remark that in these works, the Poisson coefficients are not modified or degraded for failed elements, only Young's modulus and stiffness.

$$\begin{aligned} E_{11} &= D_1 E_{11}^0 \\ E_{22} &= D_2 E_{22}^0 \\ G_{12} &= D_6 G_{12}^0 \end{aligned} \tag{5.1}$$

where E_{11} and G_{12} are the effective material properties with damage and E_{11}^0, E_{22}^0 and G_{12}^0 are the material properties without damage. The patterns in damage progression are in agreement with experimental results obtained by Tan *et al.*, but it was observed that the estimated strength values are very sensitive to selected values of internal variables.

Camanho and Matthews [1999] found a good adjustment of analytical and experimental results for a carbon reinforced plastic. The next values are the assigned damage

degradation constants for bending, traction and shearing: D_1^T=0.07, D_2^T=D_4^T=0.2, D_1^C=0.14, D_2^C=D_4^C=0.4, where T is for tension and C for compression.

For matrix tensile traction (and shearing cracks): E_2^d=$D_2^T E_2$; G_{12}^d=$D_4^T G_{12}$; G_{23}^d=$D_4^T G_{23}$

For fiber tensile traction: E_1^d=$D_1^T E_1$

For matrix compression (and shearing cracks): E_2^d=$D_2^C E_2$; G_{12}^d=$D_4^C G_{12}$; G_{23}^d=$D_4^C G_{23}$

For fiber compression: E_1^d=$D_1^C E_1$

In the work of Chang *et al.* [1991] a comparison between experimental and numerical results for a holed laminated is presented. In this work different failure criteria are presented too. They differ from previous commented works because the material properties are reduced to 0.0, including Poisson ratios when the criteria are reached. In the documentation of the user subroutine USDFLD of the finite element software Abaqus, a simulation of the test of this work is made with multiple failure modes of an epoxy-graphite laminated (-45/+45) composed of 24 layers. The material is defined as a laminated with the option `*Material` (`Type=LAMINA`) where elastic properties defined for a planar state of stress are the following: E_x, E_y, ν_{xy}, G_{xy}.

In the example the subroutine is applied to solid linear materials CPS4 of full integration and CPS4R of reduced integration.

The failure criteria proposed by the authors for this analysis are developed in their work and are the following: matrix failure, shearing fiber/matrix, shearing failure of the entire composite and combination of these.

The Abaqus results are compared with experimental load-displacement data (Fig. 5.6) with excellent agreement up to the point where the load maximum is reached. After that, the numerical load-displacement curve drops off sharply, whereas the experimental data indicate that the load remains more or less constant (Systemes). The dominant failure mode is the fiber/matrix shearing. In the analysis is commented that a better adjustment on the results could be achieved if some after-failure material data were available. Without these, the behavior is very sensitive to the mesh and type of element which is very clear in the difference between curves in Fig. 5.6.

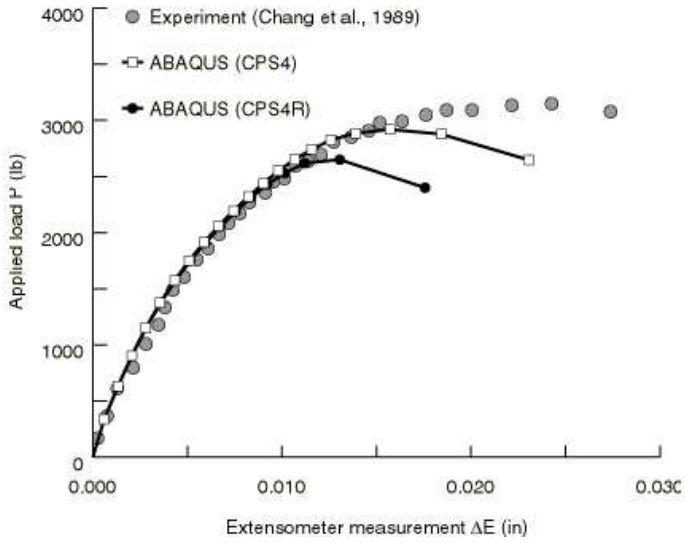

Figure 5.6: Experimental and numerical (Abaqus/Standard (Systemes)) load displacement curves from Chang *et al.* [1991].

5.1.2 Element failure method (EFM)

In the literature there is a more frequent use of MPDM for the progressive damage analysis. Nevertheless is important to remark that has potential disadvantages when the stiffness matrix values are zero or close to zero. As an alternative to avoid this disadvantages, Tay *et al.* [2003] proposed the EFM for the progressive damage in composites for a fast convergence. Essentially, the method manipulates the element nodal forces directly in order to simulate the damage effect without making any change in the material stiffness. The failed elements are not eliminated of the mesh, instead a number of equivalent forces are applied to the internal forces acting on these nodes.

If we have for example a 2D finite element, the relationship between node forces and stiffness is:

$$\mathbf{K}\,\mathbf{u} = \mathbf{f} \tag{5.2}$$

Where u is the nodal displacements vector, f is the nodal forces vector and K is the master stiffness matrix without damage. Integrating over the domain Ω we have the equation 5.3.

$$\mathbf{K} = \int_{\Omega} \mathbf{B}^T \mathbf{C}\ \mathbf{B}\ d\Omega \tag{5.3}$$

where $\mathbf{C}$ is the stress-strain matrix and $\mathbf{B}$ is the matrix that relates strains with nodal displacements.

By performing the corresponding operations for plane stress or plane strain 2D problems, we have the following forces (the example is in 2D but in 3D is absolutely analogous):

$$\begin{aligned} f_{xi} = C_{11} \int_{\Omega} N_{i,x} \left(\sum_{j=1}^{m} N_{j,x} u_{xj} \right) d\Omega \\ + C_{12} \int_{\Omega} N_{i,x} \left(\sum_{j=1}^{m} N_{j,y} u_{yj} \right) d\Omega \\ + C_{66} \int_{\Omega} N_{i,y} \left(\sum_{j=1}^{m} N_{j,y} u_{xj} + \sum_{j=1}^{m} N_{j,x} u_{yj} \right) d\Omega \end{aligned} \tag{5.4}$$

$$\begin{aligned} f_{yi} = C_{12} \int_{\Omega} N_{i,y} \left(\sum_{j=1}^{m} N_{j,x} u_{xj} \right) d\Omega \\ + C_{22} \int_{\Omega} N_{i,y} \left(\sum_{j=1}^{m} N_{j,y} u_{yj} \right) d\Omega \\ + C_{66} \int_{\Omega} N_{i,x} \left(\sum_{j=1}^{m} N_{j,y} u_{xj} + \sum_{j=1}^{m} N_{j,x} u_{yj} \right) d\Omega \end{aligned} \tag{5.5}$$

It is clear that for every coefficient change C_{ij} of the stiffness matrix, it would be the correspondent change on nodal forces. It is always possible to calculate the equivalent forces for each particular material stiffness while the contrary is not always satisfied. In other words, applying changes on nodal forces not always correspond to identifiable changes on stiffness material properties. For this reason, the EFM is a more general method than MPDM.

If for example, a finite element of a material without damage that has a group of nodal forces that have been obtained in the equilibrium condition (see Fig. 5.7). These forces can be calculated on parallel and perpendicular direction from fibers. The group of internal nodal forces of the element will be in equilibrium with the opposite group of nodal forces of the adjacent elements that are connected with. However, for an element that has reached the damage, the load capacity will be compromised in a dependent dimension and spatial way. For example, if most part of damage is generated by transversal matrix microcracks, it is evident that the element will have a reduction on the load capacity on the transversal direction from fibers.

The illustrated process of Fig. 5.7 corresponds to a completely failed element; the damage is extended in both directions: fiber and transversal to fiber and for that reason the element should not be able to support any load. As commented before, in a previous state from failure of the element, the nodal forces are in equilibrium with the external forces of the adjacent elements (Fig. 5.7). When the element reaches the failure, some iterative external forces are applied (black arrows in Fig. 5.7c) in such a way the corresponding forces of the adjacent elements of the mesh are cancelled. After every successful step, the internal nodal forces of the mesh (pointed arrows) will decrease in magnitude until a very small value remains (close to zero or to a very small percentage from the original value). This process is automatized and a very small residual value is specified. In that way the iterative process will end when that residual value will be reached. Fig. 5.8 shows a flux diagram for the implementation of this method.

Is important to remark that the cancelled forces in this process are not the internal nodal forces of the element but the internal nodal forces of adjacent elements of the finite element mesh. The failed element has been strained under the applied external forces; because of this the internal stresses of the damaged element do not conserve a physical meaning.

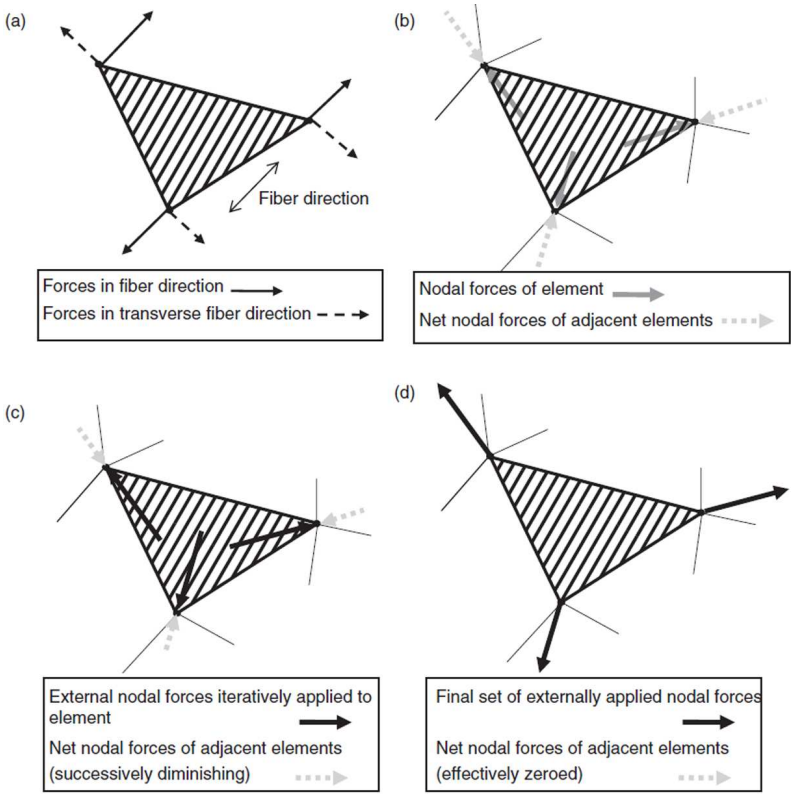

Figure 5.7: The EFM procedure by Tay *et al.* [2008].

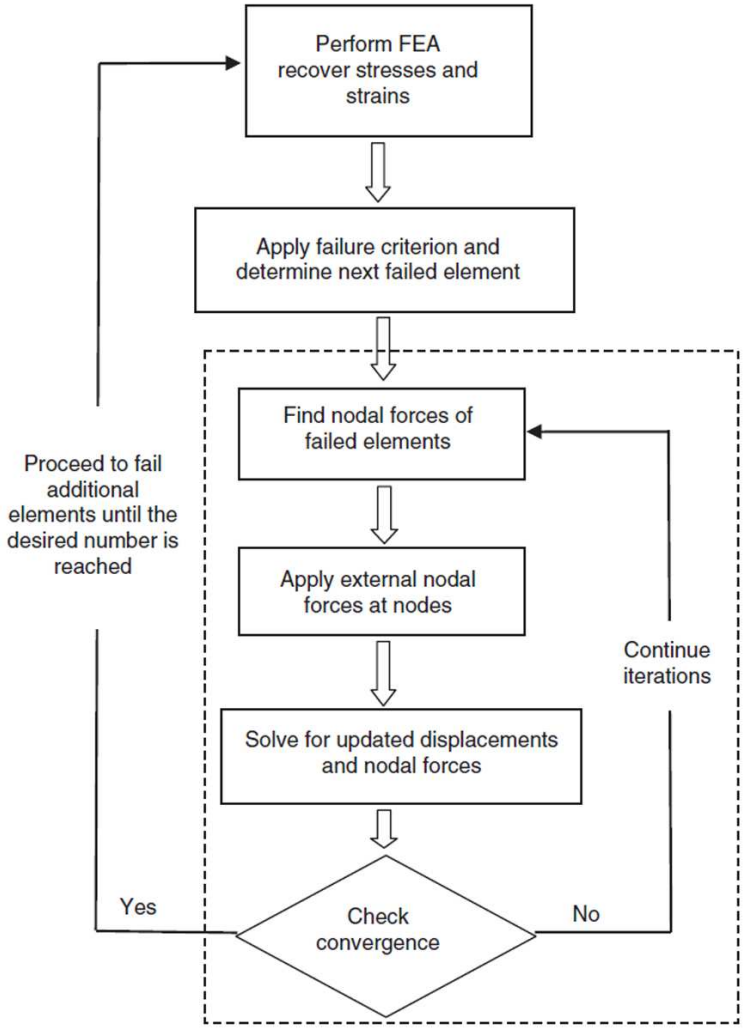

Figure 5.8: Flowchart for implementation of EFM by Tay *et al.* [2008].

One advantage of this technique is that it allows the crack propagation in any direction without the need to re-mesh or modify the constitutive material matrix.

5.2 Failure criteria

As explained in previous sections, there are multiple theories in literature for implementing damage that are used not only to predict failure initiation but also for predicting a damage pattern after reaching material ultimate strength. If we consider an osteon as a laminate composed of multiple thick and thin lamellae, we can group the most influent stresses to failure as intralaminar and interlaminar.

In composites, intralaminar failure criteria can be classified in three groups: non-interactive (the most known are maximum stress and maximum strain), interactive (as Tsai-Hill and Tsai-Wu (Tsai and Wu [1971])), partially interactive or failure mode based (as Hashin and Rotem [1973] and Puck [1998]). The validity and applicability of each one depends on the convenience of the application and the adjustment with experimental results (Daniel [2007]).

The maximum stress and maximum strain criteria are typical examples of non-interactive theories that do not predict failure accurately because they overestimate the failure strength without having into account the interaction of different modes. Interactive theories as Tsai-Wu have better agreement with experimental results.

In composites, failure highly depends on the loading pattern. The most common failure in laminates is delamination, defined as separation between adjacent layers. Other analyzed failure modes for this type of materials are the matrix itself, fiber breaking or pullout of fibers. In laminates, the shearing failure can lead to low nominal stresses due to the weakening of interlaminar area.

In fracture mechanics the failure analysis is based on the stress-strain state that is required for a preexisting crack to propagate. The theories and failure modes observed in composites are applicable to bone tissue (Cowin [2001]). The problem in cortical bone lies in the complexity of obtaining experimental data at microstructural or inferior levels in order to set the failure modes, critical loads for failure initiation and

stress levels for crack propagation. As a conclusion of a large number of works, from Cowin [2001] it can be inferred the importance of interfaces at different hierarchical levels for evaluating failure criteria and the large dispersion of experimental data.

As described previously, the interface between collagen and hydroxyapatite reinforcement plays an important role in the mechanical analysis of cortical bone and in that aspect it is important to know the loading transmission between matrix and fibers. In composite material theories it is commonly assumed a perfect bond mathematically described as continuity in matrix and fiber displacement.

In Bundy [1985] is demonstrated that a composite modulus decrease if there is at least a portion of mineral that debonds and at the same time, this indicates that the continuity condition is not fitted. The initial models in literature are very simplified and the evolution on experimental techniques (Zysset *et al.* [1999]; Ebacher *et al.* [2012]; Gupta *et al.* [2006]; Gupta and Zioupos [2008]; Gupta *et al.* [2013]) as electronic microscopy, computerized tomography, X-Ray scattering, etc. has induced to more complex models that can analyze with more detail the intralamelar level.

In Chapter 4 the strength lamellar properties have been derived from homogenized values so the effect of damage between the interface collagen-matrix is not taken into account. In order to analyze the interlaminar failure, the Brewer and Lagace quadratic criterion of Eq. 5.6 has been chosen (Brewer and Lagace [1988]). This criterion is widely used in the context of composite materials to analyze the delamination with excellent correlation with experimental tests.

$$\left(\frac{\langle\sigma_{rr}\rangle}{S_{rr,\mathrm{t}}}\right)^2+\left(\frac{\sigma_{r\theta}}{S_{r\theta,\mathrm{s}}}\right)^2\geq 1 \quad \text{con} \quad \sigma_{rr}>0 \tag{5.6}$$

where

σ_{rr} = radial stress
$\sigma_{r\theta}$ = shear stress
$S_{rr,\mathrm{t}}$ = radial tensile strength
$S_{r\theta,\mathrm{s}}$ = shear strength

The Macaulay bracket operator $\langle\ \rangle$ in the first term denotes the positive part and indicates that the radial stress must be included only if $\sigma_{rr} > 0$, because compressive radial stresses tend to close any eventual microcrack and therefore make no contribution to the interlaminar failure criterion. The criterion is interactive in the sense that accounts for the simultaneous contribution of the radial and shear stresses. In the context of structural composites, this criterion is used to predict delamination between laminate plies.

The intralaminar failure of a lamella requires the individual verification of the following relationship for each lamella:

$$\sigma_{\theta\theta} \geq S_{\theta\theta} \tag{5.7}$$

which simply checks whether the lamella fails under circumferential tensile stress or not. Note that circumferential compressive stresses are considered not to lead to intralamellar failure.

Chapter 6

2D cortical bone models

6.1 Single osteon model

As a first approach to the analysis of cortical bone a 2D model of a single osteon is proposed. The aim of this finite element model is to determine the inplane stress distribution and predict the location of microcrack initiation and further propagation based on Ascenzi *et al*. compression tests (Ascenzi *et al.* [1973]). The geometry has been simplified to a half circular ring, including 17 thin lamellae and thick lamellae, see Fig. 6.2. The alternating arrangement of these lamella resembles the type I osteon described by Ascenzi *et al.* [1973], see Fig. 4.2. The first lamella around the haversian canal is a thin lamella, with a dominant fibril orientation in the circumferential direction Ascenzi *et al.* [1973].

Although it is well known that lamellae have thicknesses variations, we have assumed that the thin and thick lamellae have constant thicknesses of 0.8 μm and 2.4 μm, respectively, according to the arrangement described in Section 3.2. The diameter of the haversian canal is 40 μm and hence the total diameter of the osteon is 148.8 μm. All these dimensions are in agreement with the secondary osteon dimensions reported in Cowin [2001]. Due to the small thickness of the specimen tested by Ascenzi *et*

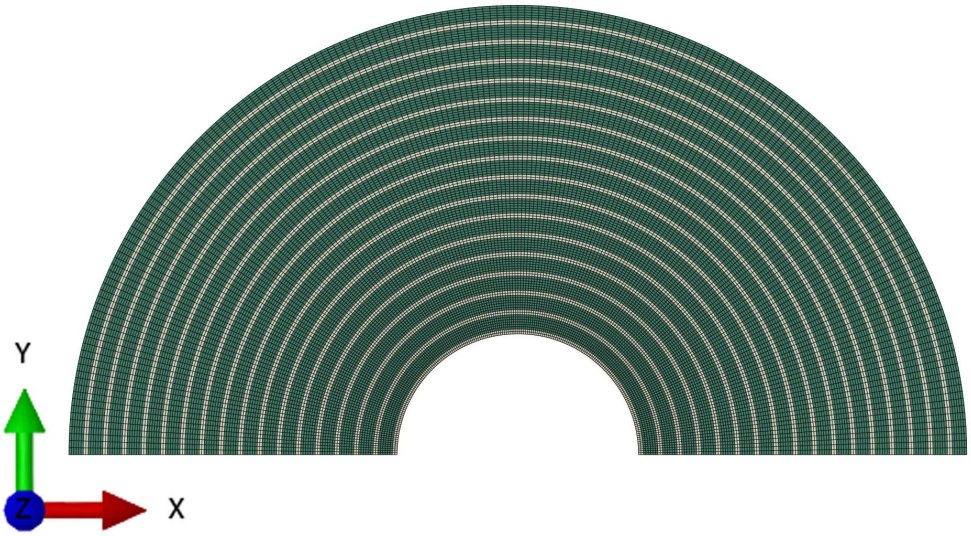

Figure 6.1: FE mesh without lacunae, clear color is for thin lamellae and dark for thick lamellae.

al. sketched in Fig. 4.1, a plane stress condition has been assumed, with unitary thickness. The applied pressure p is distributed along a 60° circular arc, being its magnitude increased through the analysis. In this research half ring has been used to model the osteon because it is intended to analyse the effect of the asymmetric distribution of lacunae, although a quarter would be mathematically sufficient for a symmetric geometry.

A structured mesh has been generated that facilitates the definition of the lamellae boundaries. Since some contact surface procedures are involved in the analysis, a 4-node bilinear element has been used (CPS4 in Abaqus). In the following Subsection 6.1.1 the procedure of adding lacunae to the model is explained.

To ease the introduction of anisotropic properties and application of failure criteria, an essential feature of the model is the alignment of the material axes with the circumferential and radial directions of the osteon reference system, see Fig. 3.14. All the resulting stresses are also referred to the axes r and θ of Fig. 3.14.

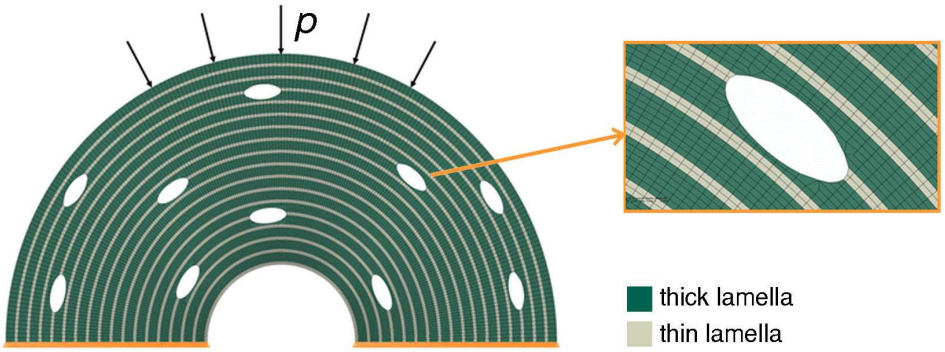

Figure 6.2: Finite element model, showing the applied load, the displacement constraints, the lamellae and the lacunae considered. The mesh is structured, enabling the arrangement into thin and thick lamellae of constant thickness and the cylindrical orientation of the material axis for each lamella. The detailed view shows the modification of the structured mesh to allow for the presence of lacunae.

6.1.1 Including lacunae to the model

During forming and remodeling stages of osteons a big number of cellular processes are active, being these achieved by three principal types of cells beside blood cells: osteoclasts, that absorb old tissue and leave space for next type of cells: osteoblasts, that nucleate and synthesize bone, and finally osteocytes that are osteoblasts "trapped" into the lamellar tissue but keeping a structured net of fine canaliculi between them, see Fig. 6.3. The space they fill into the tissue is called lacuna and has an approximated ellipsoidal shape that is very important for the remodeling process because of its known role as sensors of the mechanical state of the osteon and for triggering the remodeling process when it is needed (Klein-Nulend *et al.* [2012]; Ascenzi *et al.* [2008]; Nicolella *et al.* [2006]; Knothe Tate *et al.* [2004]).

In order to include lacunae to the FE mesh, a subroutine in Matlab has been developed, starting with a central node as an input. The shape of the elements that surround the center is transformed into ellipses trying to preserve the good quality of the original structured mesh. This script is programmed in a way that is possible to include a lacuna anywhere in the mesh. Shown in Fig. 6.1.

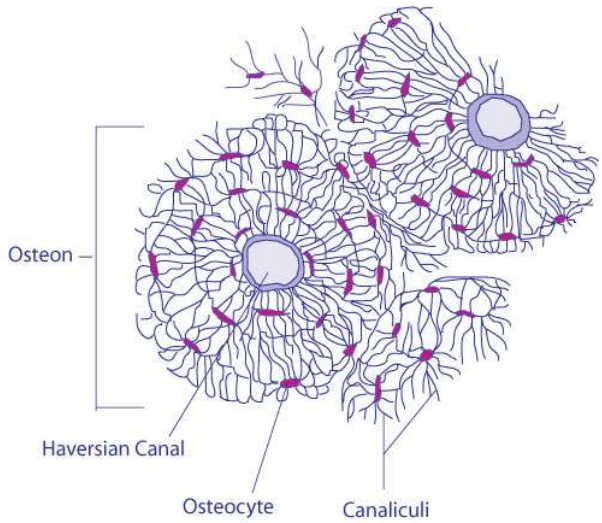

Figure 6.3: Diagram depicting transverse section of cortical bone at microstructural level.

The geometry of the lacunae is based on the features given by Prendergast and Huiskes [1996], where the lacunae are described as ellipsoids of dimensions 22μm x 9μm x 4μm, with a major axis forming about 26° with the osteon axis and located in the boundary between lamellae (Currey [1962]). Therefore, the ellipses modelled in this work are a section of the 3D ellipsoids, assuming all the intersected lacunae are located in the same transverse plane. Hence the dimensions of lacunae are approximately the same (with minimum variations generated by the different sizes of elements and its orientation). The spatial distribution of the lacunae is based on the data found in Cowin [2001], that report an average density in cortical bone of 460 lacunae per mm^2 and an average lacunae area of about 30 to 40 μm^2.

The subroutine for generating lacunae from a structured FEM mesh has the following procedure:

- The stated shape has different element sizes, hence the exact geometry of lacunae depends on the elements that compose it and the place that are located.
- The lacunae size is taken from bibliography: ellipsoids between lamellae with approximated dimensions of principal axes: 22 μm x 9 μm x 4μm (Prendergast and Huiskes [1996]). In order to model the transversal section is assumed in

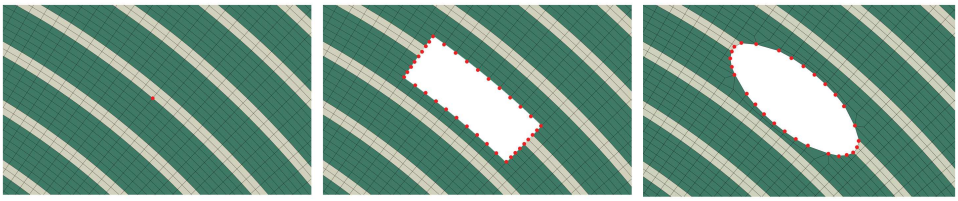

Figure 6.4: Sequence for including lacunae to the mesh. Firstly the central node is identified, secondly the neighboring elements are deleted and finally the surrounding nodes are relocated in ellipsoidal shapes.

this model that all the lacunae are in the same plane of the osteon, hence the dimension of lacunae are approximately the same (with minimum variations generated by the different sizes of elements and its orientation).

- The size of elements neighboring the central node (input) is read from the coordinate matrix and it is compared with the size of principal axes of lacunae. The subroutine calculates the number of elements that are totally contained in the lacuna and eliminates them from the mesh (Fig. 6.4).
- The coordinates of the remaining nodes in contour are modified in such a way that they are moved to the ellipse contour, trying to preserve the side orientation of elements.

Using this procedure and the correlation with some images in the literature, 10 lacunae have been included in the half-model of an osteon shown in Fig. 6.2.

Lacunae are placed in the osteon taking images from literature as reference. In Ascenzi *et al.* [2008] a periodic structure of lacunae is proposed that fulfils the characteristic patterns of spacing and distribution of micrographs. According to Cowin [2001], the mean area of a lacuna is from 30 to 40 μm^2 and its cortical bone density is 460 lacunae per mm^2. In agreement with these data and relating to micrographs in literature, 10 lacunae have been included in the mesh. Fig. 6.2 shows the result of the inclusion following the previous procedure and concluding the geometrical model. The material axes of the modified elements are also defined in accordance to the global circumferential and radial directions.

6.2 Material model

The material definition in Abaqus as in the most common finite element codes has the following characteristics:

- It specifies the material behavior and set all the relevant property parameters.
- It can define multiple material behaviors.
- The material has an assigned name that is used to define all the elements that are represented by the same properties.
- It can be variable field dependent and can be assigned to solution dependent field variables.
- It can be specified in a local coordinate system. This is required for non-isotropic materials.

The anisotropic elastic material properties for thick and thin lamellae that have been calculated in Chapter 3 are defined in Abaqus through the `*elastic` command with `type=anisotropic` and followed by the constant values lines of the constitutive matrix with the structure shown in Eq. 6.1.

$$\begin{Bmatrix} \sigma_{11} \\ \sigma_{22} \\ \sigma_{33} \\ \sigma_{12} \\ \sigma_{13} \\ \sigma_{23} \end{Bmatrix} = \begin{bmatrix} D_{1111} & D_{1122} & D_{1133} & D_{1112} & D_{1113} & D_{1123} \\ & D_{2222} & D_{2233} & D_{2212} & D_{2213} & D_{2223} \\ & & D_{3333} & D_{3312} & D_{3313} & D_{3323} \\ & & & D_{1212} & D_{1213} & D_{1223} \\ & & & & D_{1313} & D_{1323} \\ & & & & & D_{2323} \end{bmatrix} \begin{Bmatrix} \epsilon_{11} \\ \epsilon_{22} \\ \epsilon_{33} \\ \gamma_{12} \\ \gamma_{13} \\ \gamma_{23} \end{Bmatrix} = \left[D^{el}\right] \begin{Bmatrix} \epsilon_{11} \\ \epsilon_{22} \\ \epsilon_{33} \\ \gamma_{12} \\ \gamma_{13} \\ \gamma_{23} \end{Bmatrix} \tag{6.1}$$

where $1 = x$, $2 = y$ and $3 = z$ of the coordinate system of Fig. 6.1.

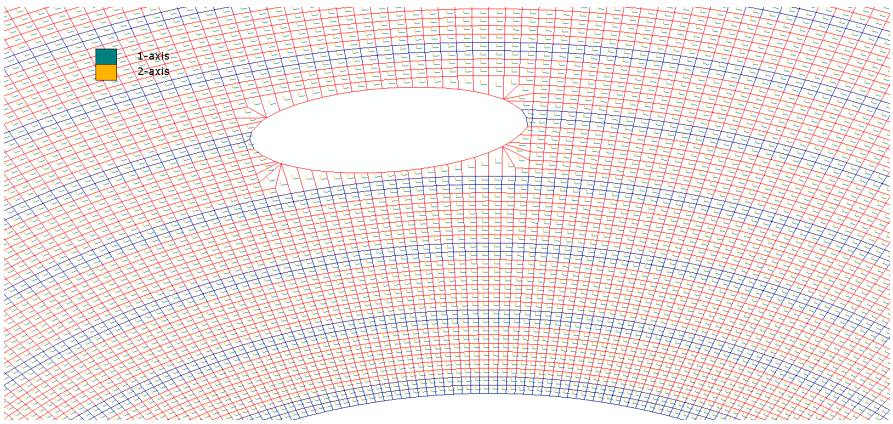

Figure 6.5: Detail of the local coordinate system of each element of the mesh. Thin lamellae are shown in red.

6.3 Coordinate systems

For the anisotropic material orientation definition and setting of failure criteria is essential to use a local coordinate system for elements with the polar coordinate arrangement of Fig. 3.14, with axes parallel to radial and circumferential directions. In Fig. 6.5 the local system defined for the thick and thin lamellae materials is shown, having all the properties defined in this reference system.

The definition of the coordinate system in the Abaqus input is made by the coordinates of two points that are situated on the z axis of the cylindrical coordinate system of Fig. 6.6. The command is: `*ORIENTATION, DEFINITION=COORDINATES, SYSTEM=CYLINDRICAL`.

Additionally, the boundary conditions for a single osteon model are the displacement constraint of the two inferior surfaces that correspond to the symmetry axis of Fig. 6.2 (applied in the input file with the command `*BOUNDARY, TYPE=DISPLACEMENT`).

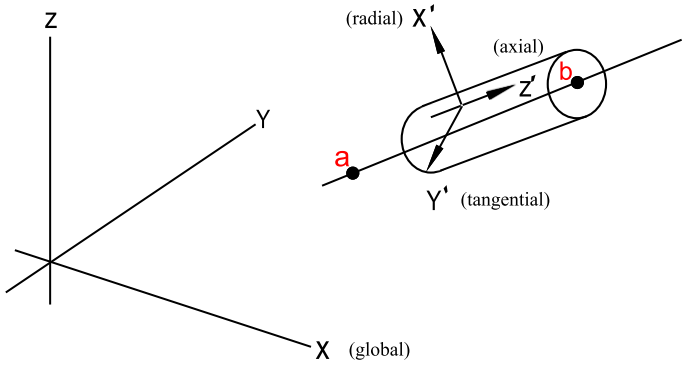

Figure 6.6: Cylindrical coordinate system defined in Abaqus by the coordinates of points a and b.

6.4 Failure initiation

In order to determine the interlaminar failure, the Brewer and Lagacé criterion (Eq. 5.6) has been implemented in Abaqus and applied to the stress evolution resulting from increasing the applied pressure p. Fig. 6.7 shows a contour map of the value given by the left side of Eq. 5.6. The interlaminar failure initiates when this value is 1 and the first occurrence takes place in a thick lamella (indicated by an arrow), about 45° with respect to the vertical axis and in the neighborhood of a lacuna that acts as a local stress raiser. The failure load at this instant is $p \approx 14$ MPa. The region where the failure initiates is in agreement with the experimental evidences commented in Chapter 4.

The mode failure is mainly by interlaminar shear, since $\sigma_{r\theta}$ reaches its strength limit $S^{\text{thick}}_{r\theta,\text{s}} \approx 20$ MPa, as shown in Fig. 6.8(c). In Fig. 6.8(a) it can be observed that, in the regions of high $\sigma_{r\theta}$, the interlaminar radial stress σ_{rr} is small compared with its strength limit $S_{rr,t} = 50$ MPa, and therefore contributes very little to the failure criterion 5.6. The different shear limits in thick and thin lamellae and their interaction due to their different stiffness, tend to concentrate the failure initiation in regions at about 45° with the vertical axis. Note in Fig. 6.8(c) that the lacuna presence exacerbates the stress concentration locally, causing the failure initiation.

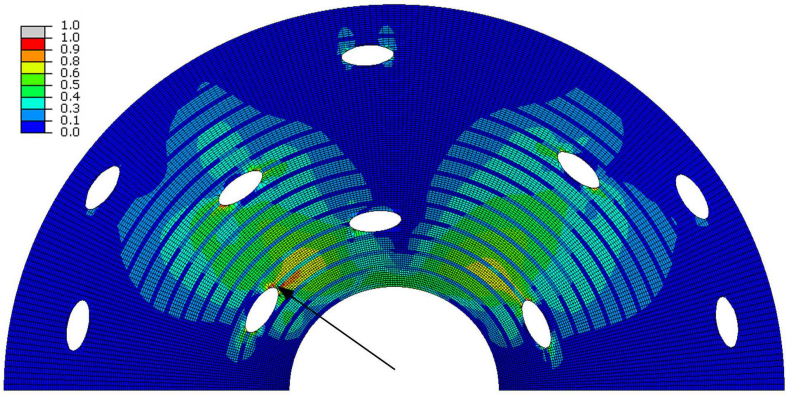

Figure 6.7: Initiation criterion. Application of the failure criterion of Brewer and Lagacé to determine the initiation of failure, reached at a load of $p \approx 14$ MPa.

6.5 Interlaminar failure propagation using the node release technique

After determining the initiation of failure and its location, the propagation has been carried out using two different techniques: the node release technique and the progressive damage approach. In the node release technique (NRT), contact surfaces are defined along the prospective crack propagation direction. This technique is often used to model debonding of surfaces along a specified direction. It involves the definition of master and slave contact surfaces.

The slave nodes are constrained not to penetrate into the master surface; however, the nodes of the master surface can, in principle, penetrate into the slave surface. This has been accomplished by duplication of nodes along the interfaces between thick and thin lamellae, where microcracks are expected to grow.

The two surfaces are initially tied and act as a single surface until a prescribed failure or fracture criterion is satisfied. When the criterion is reached, the connection between the surfaces is released.

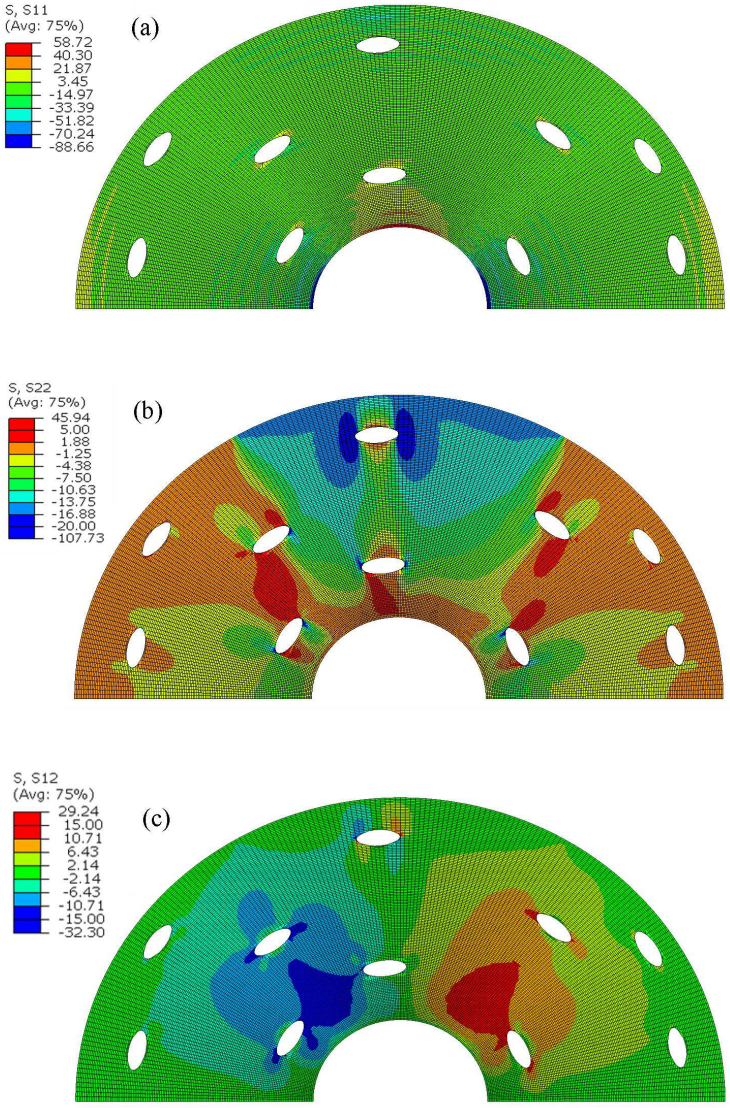

Figure 6.8: Initiation criterion. Application of the failure criterion of Brewer and Lagacé to determine the initiation of failure, reached at a load of $p \approx 14$ MPa. S11 is for circumferential stresses, S22 for radial stresses and S12 for shearing stresses.

In combination with the contact procedures available in Abaqus (Systemes), the same master and slave surfaces shown in Fig. 6.9 are used to enable the contact between crack faces after the microcrack growth. This contact exists due to the compressive nature of the applied load. The analysis of the proposed model is computationally expensive, especially because the number of potentially debonding and contacting surfaces is high (all interfaces between thick and thin lamellae). An implicit incremental approach has been used for the analysis of propagation, where debonding, contact and loss of stiffness is expected during the nonlinear analysis.

As explained before, the initiation conditions at an interface are determined using the Brewer and Lagacé criterion (Fig. 6.7). Initially, only one node is released at this point. The eventual propagation of the microcrack (equivalent to a surface delamination) is also governed by the Brewer and Lagacé criterion. The Abaqus command `*Debond` (see Fig. 6.9) is used to release the initially tied nodes as the load increases. In the simulation, initiation points of new microcracks depend on the previous microcrack evolution.

In order to evaluate the crack propagation condition, an approach based on energetic considerations, such as the strain energy release rate G should be considered. However, critical values for the specific energy at fracture G_c are not available at the interlamellar and intralamellar level. Hence, we resolved to use a stress-based approach considering the Brewer and Lagacé criterion at a certain characteristic distance d.

The Abaqus command `*Debond` involves the values of contact pressure CPRESS and contact shear CSHEAR. The criterion is then evaluated at a distance d ahead the crack tips of the generated microcrack, thus avoiding the theoretical singularity at the crack tips. The problem turns out to be the choice of the distance d. We have chosen a distance d = 1.5 μm ahead the crack tip, which provides reasonable results. A sensitivity analysis has been carried out regarding this distance, as commented at the end of this section.

The following characteristics should be fulfilled for surfaces to be debonded (Systemes):

- Both surfaces must have the same normal.

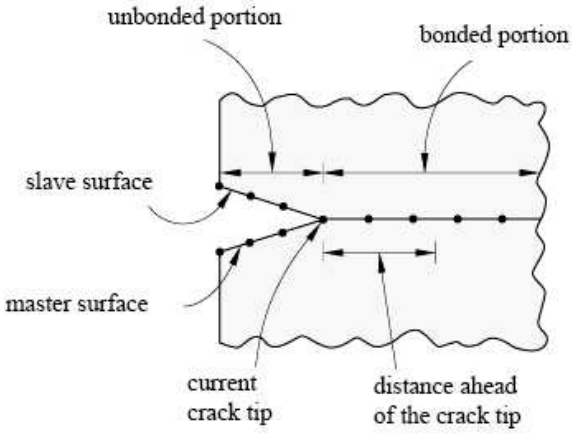

Figure 6.9: Schematic definition of the Abaqus critical stress criterion applied between two surfaces (Systemes).

- The surface should be continuum.
- Deformable elements can not be mixed with rigid body elements as part of the same surface.

In this model, the surface contact has been defined through a "`contact pair`" in Abaqus, and it implies the pairs of surfaces or node sets with surfaces that can interact between them through the analysis.

The "`contact pair`" in Abaqus/Standard (Systemes) has the following characteristics:

- Can be used to define interactions between bodies in mechanical, coupled temperature-displacement, coupled pore pressure-displacement, coupled thermal-electrical, and heat transfer simulations.
- Should be part of the model definition.
- Can be formed using a pair of rigid or deformable surfaces or a single deformable surface.
- Do not have to use surfaces with matching meshes.

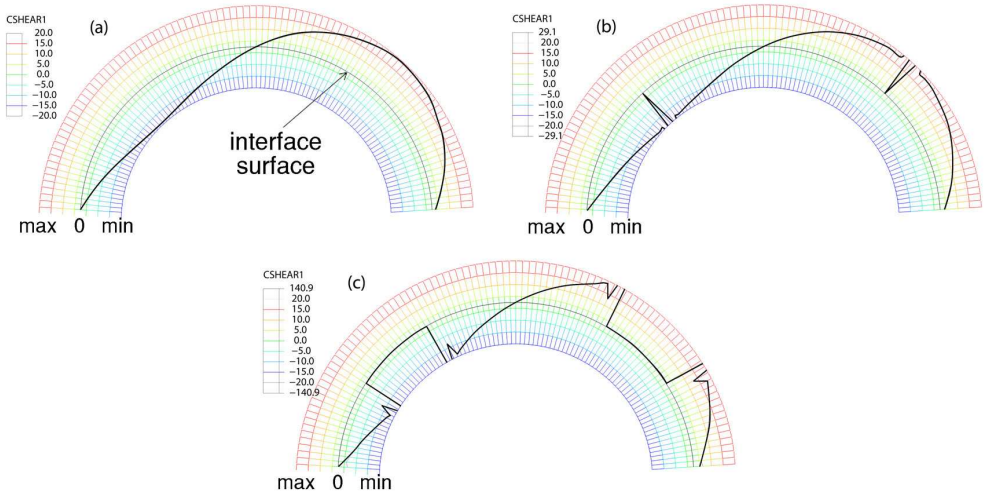

Figure 6.10: Node release technique. Evolution of shear stress along one of the contact surfaces (CSHEAR in Abaqus). For the sake of clarity, the surface does not intersect any lacunae. (a) Stress state before microcrack initiation; (b) microcrack initiation; (c) microcrack propagation.

- Cannot be formed with one two-dimensional surface and one three-dimensional surface.

Contact can be defined in Abaqus/Standard in terms of two surfaces that may interact with each other as a "`contact pair`" or in terms of a single surface that may interact with itself in "self-contact". Abaqus/Standard enforces contact conditions by forming equations involving groups of nearby nodes from the respective surfaces or, in the case of self-contact, from separate regions of the same surface.

In Fig. 6.10, the variation of CSHEAR for an interface surface is represented at three instants. The solid black lines represent the value of the shear stress along an interface between a thick and thin lamella. The coloured blue-to-red lines are simply marker scales that quantify the value of the shear stress, from minimum (blue) to maximum (red) passing through zero. The three subfigures represent different states of failure initiation and propagation. The first plot Fig. 6.10(a) represents a continuous distribution of the interface shear before failure initiation (a surface without intersecting lacunae is represented for simplicity). Once the variable CSHEAR reaches a value

close to the limit strength ±20 MPa, a node is released at this point. Hence, the interface shear stress drops locally to 0, as shown in Fig. 6.10(b).

Two incipient cracks along the interface have been formed (each with two crack tips), one on the left quadrant and the other one on the right quadrant. The shear stress drops to zero between the crack tips, because the crack faces are free from shear stresses (it has been assumed that there is no friction between crack faces).

A further increase of the load causes the interface cracks to propagate, as in Fig. 6.10(c), where CSHEAR is 0 inside the cracks. Both cracks have grown along the interface surface. The region where the shear stresses are zero has increased, i.e. the crack faces have become longer. Fig. 6.11 shows the contour maps for the Brewer and Lagacé where the red colour has 1.0 as an upper limit value. Values exceeding 1.0 are plotted in grey and represent the regions in which failure is initiated and propagated as the load is increased.

From left to right and top to bottom, the plot (a) in Fig. 6.10 corresponds to the initiation location, in a state similar to the represented in Fig. 6.11, $p \approx 14.0$ MPa. Next plot (b) shows an advancing crack on the left quadrant and a new crack just initiated on the right quadrant when the load has been increased to $p \approx 16.6$ MPa. In successive plots, both cracks grow and other microcracks are initiated and eventually grow up to a generalized state of failure with several propagated microcracks. For the last plot (f), $p \approx 20.1$ MPa, the innermost thin lamella also starts failing due to high circumferential stresses. It has been verified that the intralaminar criterion (Eq. 5.7) is not achieved at earlier stages. From 6.11, it can be observed that the numerical analysis here presented is in good agreement with the experimental behavior observed by Ascenzi *et al.* [1973] (See Fig. 4.3).

Fig. 6.12 plots the applied pressure p versus the displacement of the load application point located on the vertical radius. The expected loss of stiffness under a compressive load is evidenced by the progressive reduction of the slope in the diagram. It can be observed that once the microdamage starts due essentially to the interlaminar shear stresses, the load bearing capacity of the system is notably reduced. Fig. 6.12 shows the results of a sensitivity analysis for three characteristic distances d, showing that qualitative differences are not large within a reasonable distance d compared to geometric dimensions.

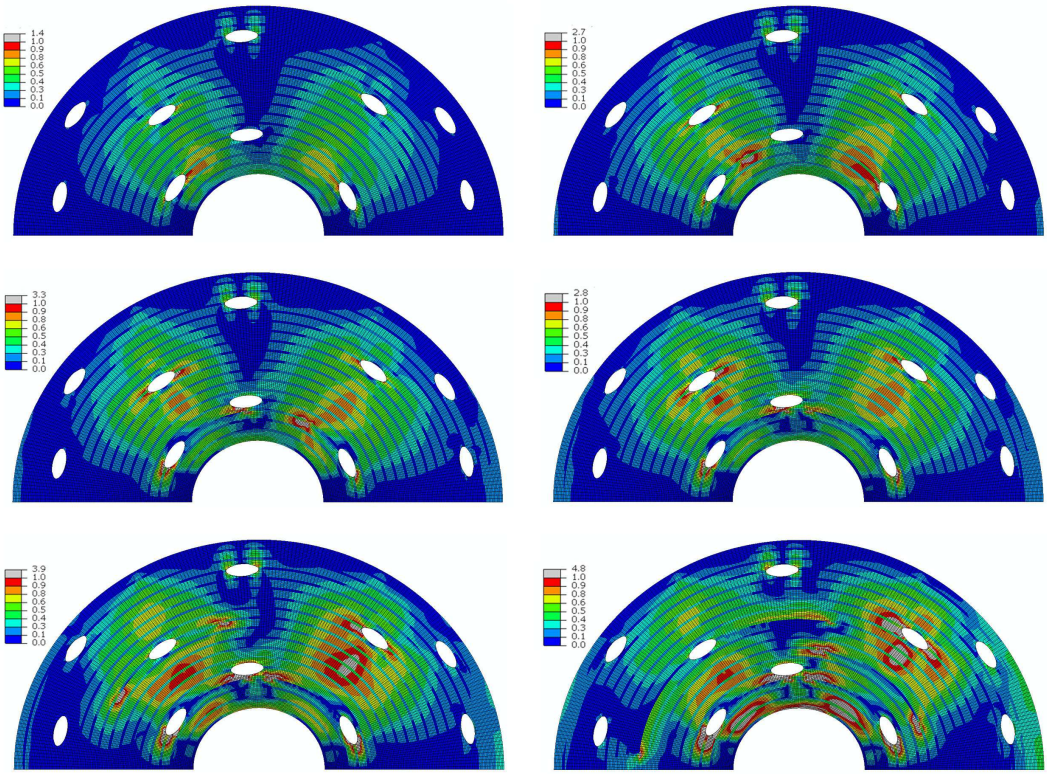

Figure 6.11: Node release technique. Evolution of the Brewer and Lagacé criterion for six instants of the microcracks initiation and propagation sequence. The instants correspond to the following applied pressures: (a) $p \approx 14.0$ MPa, (b) $p \approx 6.6$ MPa, (c) $p \approx 18.0$ MPa, (d) $p \approx 18.1$ MPa, (e) $p \approx 19.1$ MPa, (f) $p \approx 20.1$ MPa.

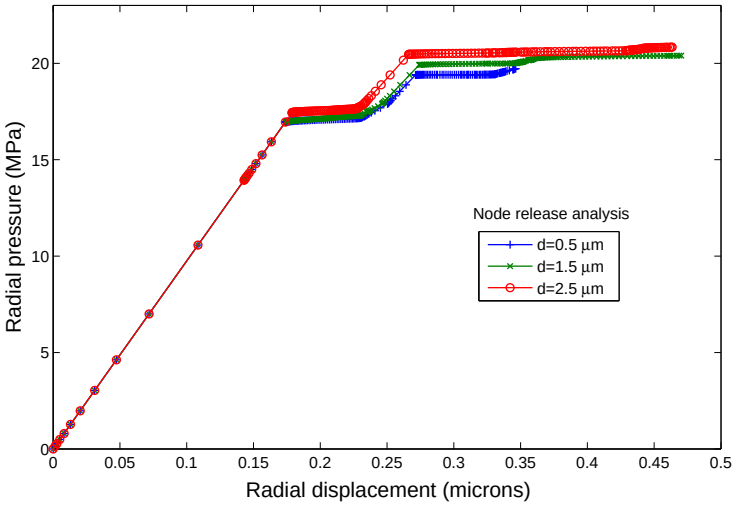

Figure 6.12: Node release technique. Sensitivity analysis to the characteristic length d used in the application of the procedure.

6.6 Progressive damage model

6.6.1 Failure propagation using the progressive damage approach

The previous analysis using NRT leads to the propagation of explicit microcracks. Despite this is similar to the real behaviour as shown in Fig. 4.3, this approach is computationally expensive and difficult to generalize to a representative volume with several osteons or to 3D models. As an alternative, the failure propagation after initiation has also been simulated through a progressive damage approach. This approach is based on a nonlinear FE analysis in which the stiffness properties are reduced at the element level as its stress state reaches a failure condition (Tay *et al.* [2008]). This approach has been successfully applied in structural composite materials, such as fiber reinforced laminates (Tay *et al.* [2008]; Chang and Chang [1987]; Hou *et al.* [2000]; Lapczyk and Hurtado [2007]).

In the progressive damage approach, there is the elastic-brittle assumption for material behavior, in the sense that there is no significative plastic deformation (Lapczyk and Hurtado [2007]). One important advantage is its relatively simple extension to 3D models, in contrast to the numerical modelling of explicit cracks using fracture mechanics, even using the extended finite element method XFEM. Obviously, the local solution in the vicinity of the damaged zone will not be as accurate as in a fracture mechanics approach, but the technique captures the global loss of stiffness and has proven to be very efficient for diffuse damage and for models with a large number of microcracks, provided the discretization is sufficiently refined (Hambli [2013]).

The simplest approach to carry out the reduction of the elastic properties is the direct material property degradation MPD (Tay *et al.* [2008]; Chang and Chang [1987]; Hou *et al.* [2000]). This method will be used in this work and consists in reducing the elastic properties by a fixed factor that can depend on the mode failure. Although its implementation is simple, it needs an a priori specification of the reduction factors. It is customary to assume that the stiffness in certain directions is reduced to 0 (Chang and Chang [1987]; Hou *et al.* [2000]), although the analysis can lead to excessively conservative results and numerical difficulties. Tay *et al*. suggest that a constant reduction factor of 0.1 is common practice in the literature due to its simplicity and convergence advantages (Tay *et al.* [2008]). Other approaches are based on continuum damage mechanics (CDM), with a less arbitrary formulation, often based on thermodynamic principles. In CDM, the damage variable can take a value in the continuous range [0, 1], and therefore the softening introduced is not abrupt.

The MPD procedure used in this work to model the progressive damage of an osteon has been implemented in Abaqus and it is similar to the implementation by Chang and Chang [1987] for structural composites. Two field variables (FV1 and FV2) have been defined by means of the user subroutine USDFLD (User Defined Field). The field variables are solution-dependent variables that enable the assignment of different material properties according to their values. Thus, FV1=0 and FV2=0 indicate no failure, FV1=1 and FV2=0 indicate interlaminar failure and FV1=0 and FV2=1 indicate intralaminar failure, see Table 6.1.

For the no failure state the elastic moduli are not reduced and for the failed state all the elastic moduli are reduced to 5% of their original values. The field variables are solution-dependent variables in the sense that they are functions of the FE solution at the integration points (in our case, function of the stresses). In the user subroutine

Table 6.1: Field variables assigned according to failure criteria

Material state	Stiffness (%)	FV1	FV2
No failure	100%	0	0
Interlaminar failure (due to σ_{rr} , $\sigma_{r\theta}$)	5	1	0
Intralaminar failure (due to $\sigma_{\theta\theta}$)	5	0	1

USDFLD, the interlaminar and intralaminar failure criteria previously explained in Chapter 5, are evaluated at each load increment considering the strength limits defined in Chapter 4 as input parameters.

The values on the left hand side of the criteria are stored at each increment as state variables (STATEV in Abaqus). On the other hand, the field variables FV are initialized to 0 when the analysis starts and only when any state variable STATEV is equal or greater than 1.0, the corresponding field variable FV is changed to 1 (damaged state). The field variable FV will remain as 1, even when the local stresses are reduced significantly, indicating the irreversibility of the damage process. Fig. 6.13 shows the sequence of damaged elements according to the Brewer and Lagacé criterion (Eq. 5.6). As explained above, the damage initiation is governed by interlaminar shear stresses in a thick lamella at about $p \approx 14$ MPa. The damage is mainly located near the stress concentration region next to a lacuna on the left quadrant. When the load is increased to $p \approx 20.1$ MPa, propagation of damage follows the elements in thick lamellae in a very similar pattern to the one predicted with the NRT of Section 6.5, Fig. 6.11.

The progressive damage approach easily allows for computing advanced states of damage. Fig. 6.14 shows a generalized state of damage for applied pressures that are higher than the loads considered in Fig. 6.13. It can be observed that damage due to interlaminar stresses tends to concentrate in the thick lamellae. It is worth noting that damaged zones approximately match the observed experimental regions, located at about 20° and 50° with respect the vertical radius. Eventually, for the highest load, damage is generalized and extends also across thin lamellae.

As far as the intralaminar criterion of Eq. 5.7 is concerned, damaged elements are shown in Fig. 6.15. Tensile circumferential stresses cause damage in the innermost

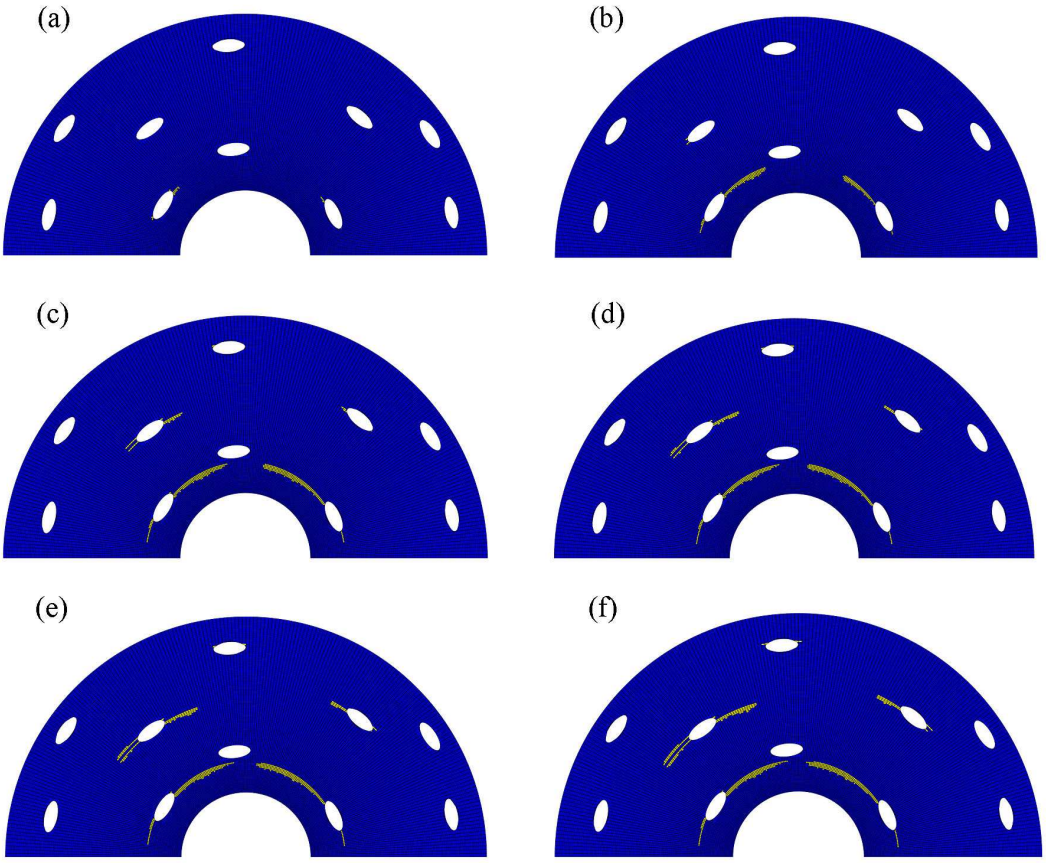

Figure 6.13: Progressive damage approach. Evolution of damaged elements (shown in yellow) by application of the interlaminar failure criterion of Brewer and Lagacé for six instants of the damage propagation sequence. The instants correspond to the following applied pressures:(a) $p \approx 14.0$ MPa, (b) $p \approx 16.6$ MPa, (c) $p \approx 18.0$ MPa, (d) $p \approx 18.1$ MPa, (e) $p \approx 19.1$ MPa, (f) $p \approx 20.1$ MPa.

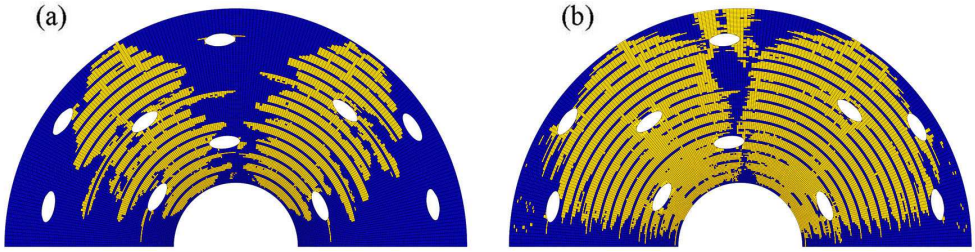

Figure 6.14: Progressive damage approach for very advanced stages of damage propagation. The instants correspond to the applied pressures (a) $p \approx 27.0$ MPa and (b) $p \approx 48$ MPa.

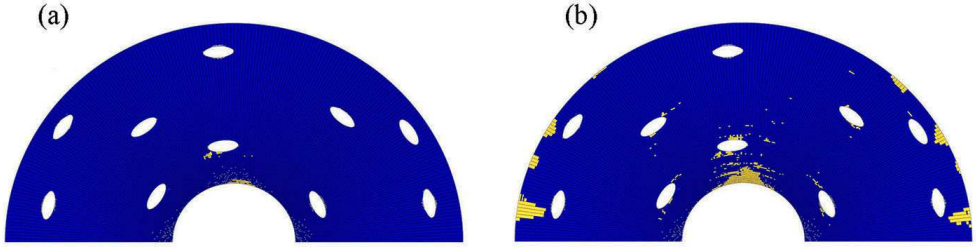

Figure 6.15: Progressive damage approach. Evolution of damaged elements (shown in yellow) by application of the intralaminar failure criterion for two very advanced load states of the damage propagation sequence. The instants correspond to the applied pressures (a) $p \approx 24.0$ MPa and (b) $p \approx 32$ MPa.

thin lamellae. The load for the initiation of this damage is relatively high (about 24 MPa), and therefore this type of damage is expected to occur only when the interlaminar failure shown in Fig. 6.13 is well developed. As a consequence, we can conclude that interlaminar shear stresses are the main cause of failure for this type of osteon under compressive diametral load, causing a separation of thin and thick lamellae, in good agreement with the experimental evidence founded by Ascenzi and Bonucci in their tests.

Chapter 7

Three point bending simulation of an ovine bone sample

In this chapter the damage degradation subroutine is applied in order to correlate experimental tests on ovine bone with a FE model aiming at inferring some elastic and strength properties that are relevant at microstructural level. Further, the initiation and growth of microcracks in the tested samples is simulated by using a damage model based on the maximum principal strain. Simulations show good correlation with the experimental results.

Three point bending tests have been carried out with cortical bone of ovine tibia, after preparing samples 20 mm long with thickness of 1 mm. Four samples have been stained for the micrograph observation in order to recognize the particular morphology at microstructural level (osteon distribution, Haversian canals, spacing and location of microcracks, etc.).

This geometry has been reproduced in a finite element model for calibration of the elastic and strength properties in such a way that the model response can be in

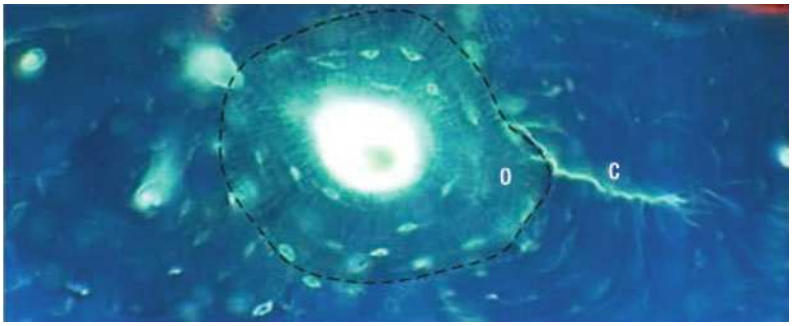

Figure 7.1: A micrograph by Taylor *et al.* [2007] where a microcrack C encounters an osteon O, and begins to grow around its cement line (dashed line). The microcrack is approximately 100 μm long.

agreement with the load-displacement behavior experimentally registered. Therefore it is possible to estimate these properties scarcely documented in bibliography through inverse analysis.

The reference models in the literature showing the distribution of damage or crack growth in cortical bone do not provide good estimations of crack propagation. As discussed in Chapter 5 the models with random distribution of osteons obtained by Budyn and Hoc [2007]; Budyn *et al.* [2008] (see Fig. 5.5) show that cracks grow in directions that cross osteons and the effect of cement lines for such propagation is not perceived, which is not in line with evidence in the literature (Taylor *et al.* [2007]; O'Brien *et al.* [2003, 2005]; Nalla *et al.* [2005]; Nicolella *et al.* [2011]), see Fig. 7.1.

In Li *et al.* [2013] three microstructural models with random distribution of osteons were analyzed (see Figs. 7.2, 7.3) using the extended finite element method (X-FEM) with an energy-based cohesive-segment scheme. In the results of these models (see Fig. 7.4) we can see how cracks propagate through osteons or Haversian canals where, as well as in Budyn and Hoc [2007], the mechanical work of cement lines appear to have no effects contrary to what is commonly accepted in several experimental works (O'Brien *et al.* [2003, 2005]; Nalla *et al.* [2005]; Nicolella *et al.* [2011]) and in our own experimentation. In these works we can see the crack following and initiating at the surroundings of the osteons and cement lines and propagating mostly through the interstitial tissue. Those cases where cracks penetrate osteons agree with experimental findings according to other authors but this case does not seem to be the dominant.

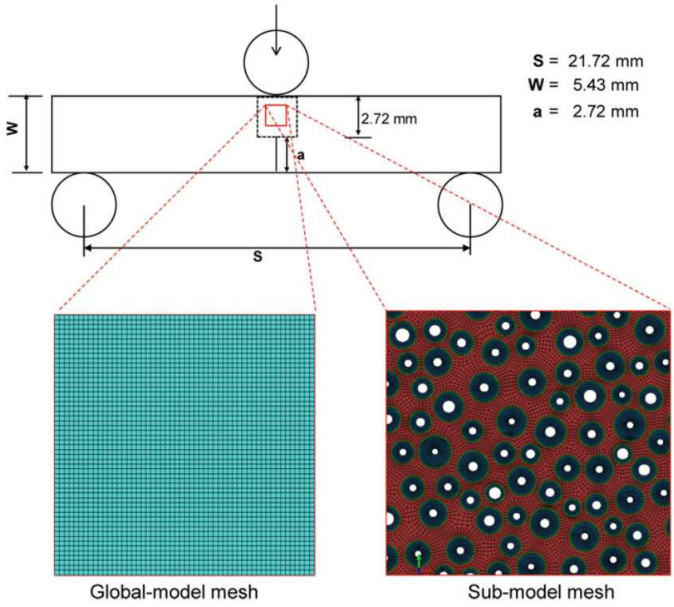

Figure 7.2: Schematic illustration of model configuration for the three-point-bending setup using global model and microstructured sub-model by Li *et al.* [2013].

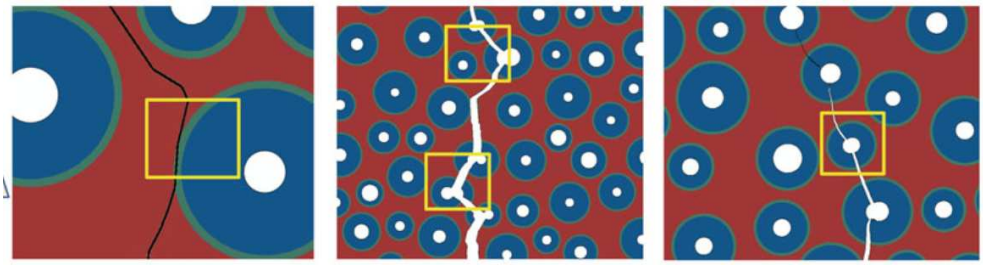

Figure 7.3: Numerical simulation of crack growth in cortical bone by Li *et al.* [2013].

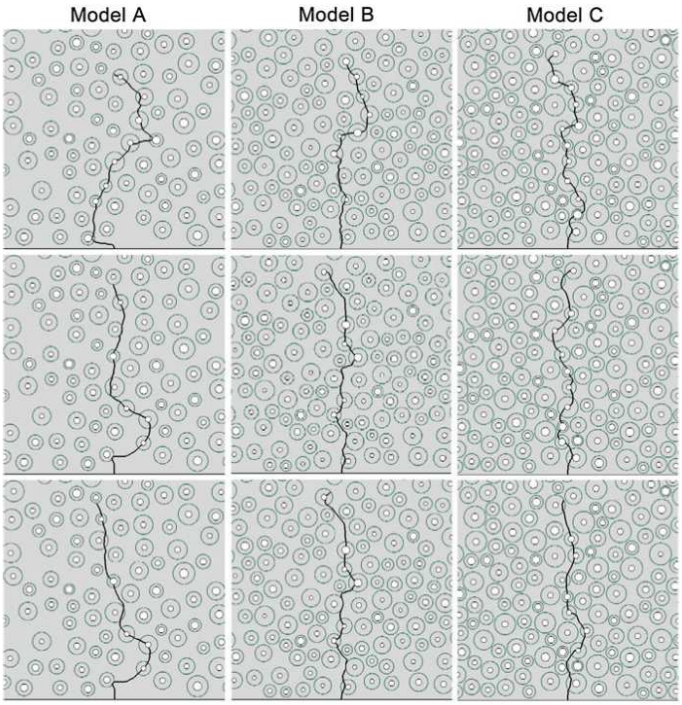

Figure 7.4: Crack propagation trajectories for various elastic moduli of cement line for three microstructured models: 25% lower than that of osteon; equal to that of osteon and 25% higher than that of osteon, by Li *et al.* [2013].

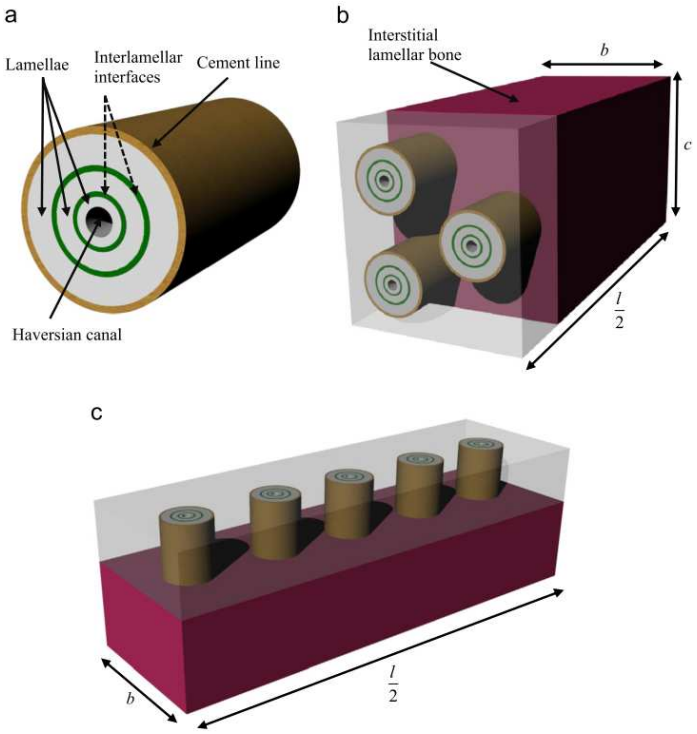

Figure 7.5: Artistic impressions of the structural characteristics of the micromechanical models developed by Nobakhti *et al.* [2014]: (a) single osteon; (b) half longitudinally-cut bone sample featuring 3 osteons; (c) half perpendicularly-cut bone sample featuring 5 osteons.

This makes sense from the point of view of protecting the osteon as the structural unity that contains the osteocytes and surrounds the blood vessels.

In the work by Nobakhti *et al.* [2014] the FE model of cortical bone of Fig. 7.5 is used to analyse local and global effects of interface structures, i.e. cement lines. Based on the results of their work, it is shown that interfaces are areas of accumulated strain in bone and are likely to act as potential paths for crack propagation. The strain amplification capability of interface structures of the order of 10 predicted by the models suggests an explanation for the levels of strain required in bone homoeostasis for maintenance and adaptation.

7.1 Mechanical tests

The mechanical tests where done at the Biomechanics Institute of Valencia (IBV) as part of the national project correspondent to this Thesis. The samples are taken from cross-section cuts made in the diaphysis of an ovine tibia with the aim of obtaining cortical sections of 1 mm of thickness as the one shown on the left hand of Fig. 7.6. Subsequently, after removing the associated tissues of periosteum and endosteum, four samples were obtained in the zone of less curvature of the total tibia transversal section.

Each one of the samples has a notch of approximately 0.5 mm (see Figs. 7.6 and 7.7). The samples were stored frozen until tests.

The microsamples were subjected to a three point bending test in an electromechanical universal machine. Fig. 7.6 shows the testing rig used for support and load application. The load application was accomplished with a velocity of 1 μm/seg and hence, the tests can be considered as quasi-static. For each sample the applied force was recorded as a function of the displacement at the application point. The results are reported in Fig. 7.8 and show an acceptable repeatability. It is evident the linearity observed until an application load of around 4-5 N. Therefore upto this range, the behavior is considered linear elastic. This will be the starting point for the generalized damage in the most stressed zones (notch vecinity) where microcracks grow fast producing the stiffness loss appreciated in the different curves of Fig. 7.8.

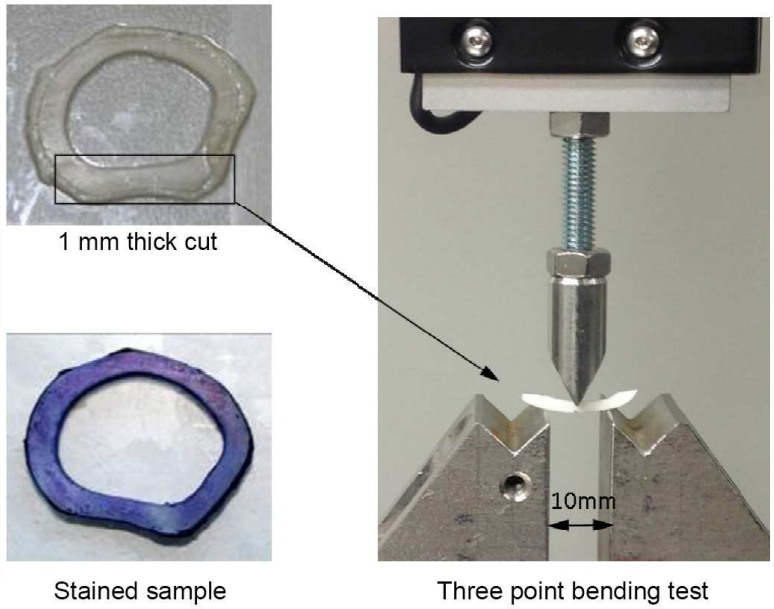

Figure 7.6: Left: Transversal section of a ovine tibia (before and after staining). Right: Three point bending of the ovine sample.

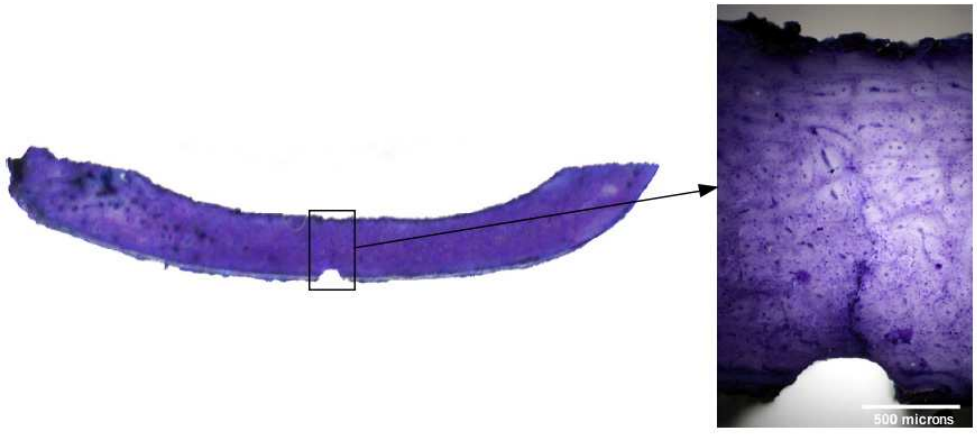

Figure 7.7: Notched test sample and detail of ovine bone stained after test No. 2.

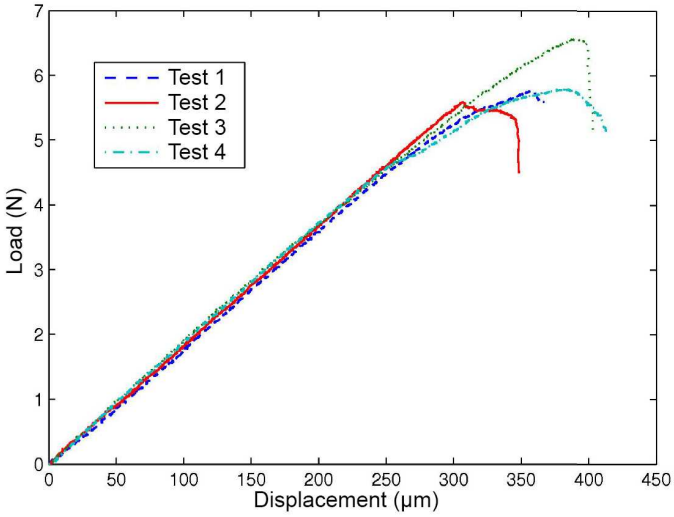

Figure 7.8: Load-Displacement response registered for four tests.

The tests were done avoiding the breakage into two parts of samples with the aim of observing the followed microcrack path a posteriori. The next step was to prepare the staining for contrast of the micrographs following a procedure proposed by Bain *et al.* [1990] that implies to dehydrate the samples (being this the reason of staining after the tests). The colorant staining for the cement lines consists in toluidine blue (1 gr.) in formic acid at 0.1% (100 ml), with 2.6 of pH during 20 minutes followed by tert-butyl alcohol (2-methyl-2-propanol) dehydration for 30 sec. It is important to avoid the presence of artifacts due to the staining and this is achieved rising the dehydration time in alcohol. Finally a quick xylene cleaning was made.

In Fig. 7.7 the osteon distribution by optical microscopy for test No. 2 is shown. The colorant concentration can be observed in the interstitial matrix, revealing the osteons and Haversian canals in a lighter color. The medium diameter of osteons is about 100 μm, although in the section some osteons present more elliptic shapes with major axis around 150-200 μm.

The existence of a growing microcrack can be observed mainly along the osteon surroundings i.e the cement lines. The origin of the microcrack is at the most stressed zone (tip of the notch).

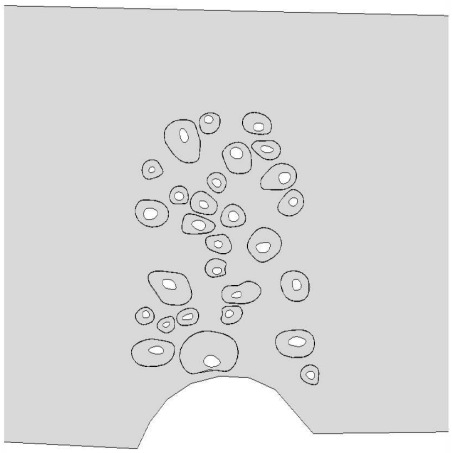

Figure 7.9: Geometrical model with osteons, cement lines and Haversian canals around the sample notch.

7.2 Finite element model

For the geometrical model generation of Fig 7.9, the sample contours and osteon shapes were processed with the software Plot Digitizer. The borderline delimitation corresponding to the cement lines is complicated and requires a thorough intervention of the analyst. Therefore this segmentation process was limited to the osteons surrounding the notch (see Fig. 7.7) that belong to the initiation and growth of the microcrack zone. The other regions sufficiently far from this zone are modeled without osteon details and instead equivalent homogenized properties are assigned. Each geometrical contour was generated from the points obtained with Plot Digitizer by a Python script in Abaqus from the osteon and Haversian canals shapes in micrographs. The thickness assigned to this model is of 1 μm.

The numerical model was solved with Abaqus v. 6.13. The obtained mesh of Fig. 7.10 has 486499 linear square elements (CPS4 in Abaqus) and 487058 nodes. A plane stress case was assumed and the region of interest is highly discretized with elements of 1 μm of side approximately in such a way that is possible to mesh the interior of cement lines. The elements of some CL are red marked in Fig. 7.10 where also boundary conditions and the applied load p are shown.

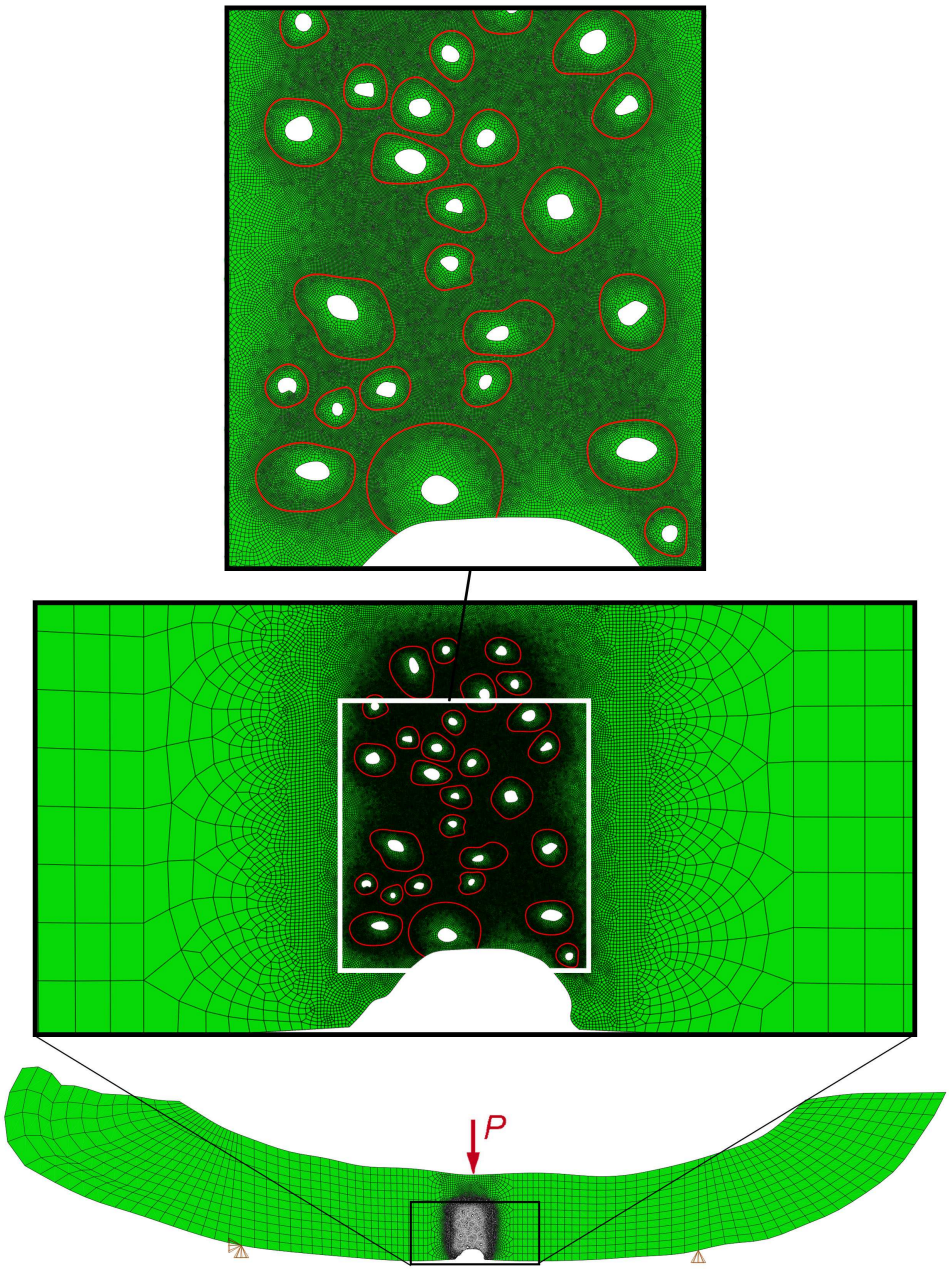

Figure 7.10: Model mesh with boundary conditions and load applied. The detailed view shows the discretization at osteons contours with the cement line elements in red.

Table 7.1: Strength properties for cement line calculated using Eq. 4.6.

	E (GPa)	ν	ϵ_i^c *test* 1 (%)	ϵ_i^c *test* 2 (%)
Osteon	11.18	0.30	17.0	17.0
Interstitial tissue	12.29 GPa	0.30	8.45	5.90
Cement line	3.3	0.30	17.40	17.75

The elastic values obtained in Chapter 3 and calculated strength properties of osteons, cement lines and interstitial tissue for two tests are summarized in Table 7.1. Regarding the damage implementation, the maximum principal strain criterion of Eq. 7.1 is implemented:

$$f = \frac{\epsilon_{p,max}}{\epsilon_i^c} \tag{7.1}$$

where $\epsilon_{p,max}$ is maximum principal strain and ϵ_i^c are critical values. Stiffness is degraded to 1% once the criterion is reached.

The first objective of the model is to verify the load-displacement response at the load application point in the linear range. A preliminary finite element analysis with the elastic values proposed in Table 7.1 shows that the numerical model has a much stiffer behaviour with respect to experimental results (13 times stiffer). Having into account the simplicity of boundary conditions and that geometrical dimensions have been modeled with precision, the stiffness of the elastic properties have to be adjusted.

After adjusting the elastic properties with a proportionality constant, the new calibrated elastic modulus for each of the regions are listed in Table 7.2.

In addition to calculated properties after calibration, in Table 7.2 some recent values of the work by Nobakhti *et al.* [2014] are listed for the same materials. The results of the test made in humid conditions results in a notably higher stiffness than in the literature data for bone tissue. Nevertheless the values reported by Nobakhti *et al.* [2014] for osteons and cement lines are even lower than the values obtained in this

Table 7.2: Calibrated Young's modulus from experimental bending test

	E model (GPa)	E from Nobakhti *et al.* [2014] (GPa)
Osteon	0.85	0.15
Interstitial tissue	0.93	13.7
Cement line	0.25	0.088

present model although this is not the case for interstitial tissue. Hence the adjusted properties can be considered in an admissible range.

7.2.1 Failure initiation strains

Figs. 7.11 and 7.12 show the strain state reached after an incremental load of 5 N, evaluated with the in-plane maximum principal strain.

In agreement with experimental tests, we can see that the maximum strain value corresponds to the cement line that is closer to the notch at the zone most prone to damage. On both figures, the same field is shown yielding strains over 16%, so we can conclude that the critical strain values for damage initiation are in that order of magnitude.

In order to determine the critical strain values, after the initial results from the behaviour at the maximum applied load, an iterative process has been done, analyzing the damage pattern evolution with respect to the critical parameters chosen until the model is in agreement with the experimental results. In this way the critical strength values are calculated with an inverse analysis. For both tests, the critical parameters are very similar even though microstructural geometries are different.

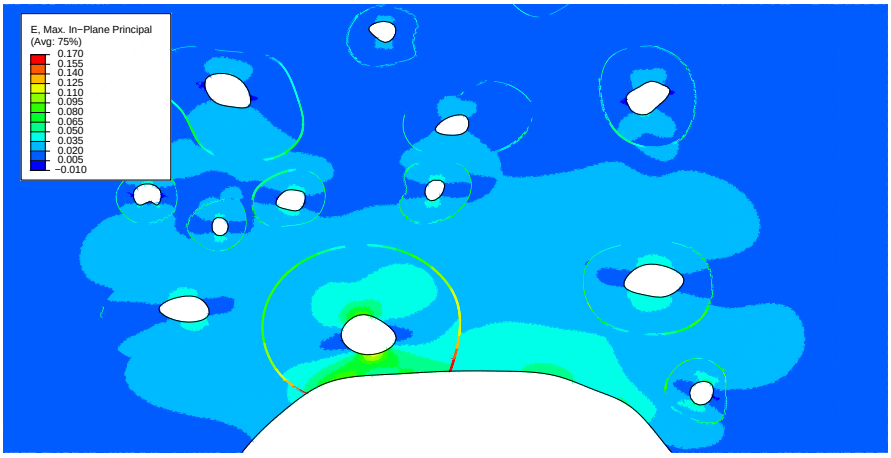

Figure 7.11: Maximum principal strain near the notch of microsample 2.

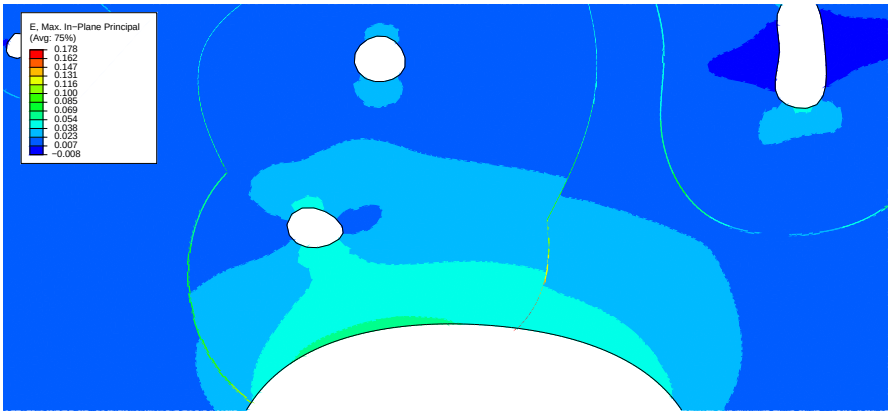

Figure 7.12: Maximum principal strain near the notch of microsample 4.

7.3 Damage model

The same damage procedure of Section 6.6 has been applied with a user subroutine USFLD in Abaqus. The damage modeling method implemented is mesh and step-dependent, so a sensitivity analysis has been carried out regarding these two variables.

Concerning time increment dependence, the substeps have to be small enough so as not to change the solution, while mesh dependence implies enough mesh-refinement.

The final damage patterns are compared with the experimental results (see Figs. 7.13 and 7.14) with good agreement.

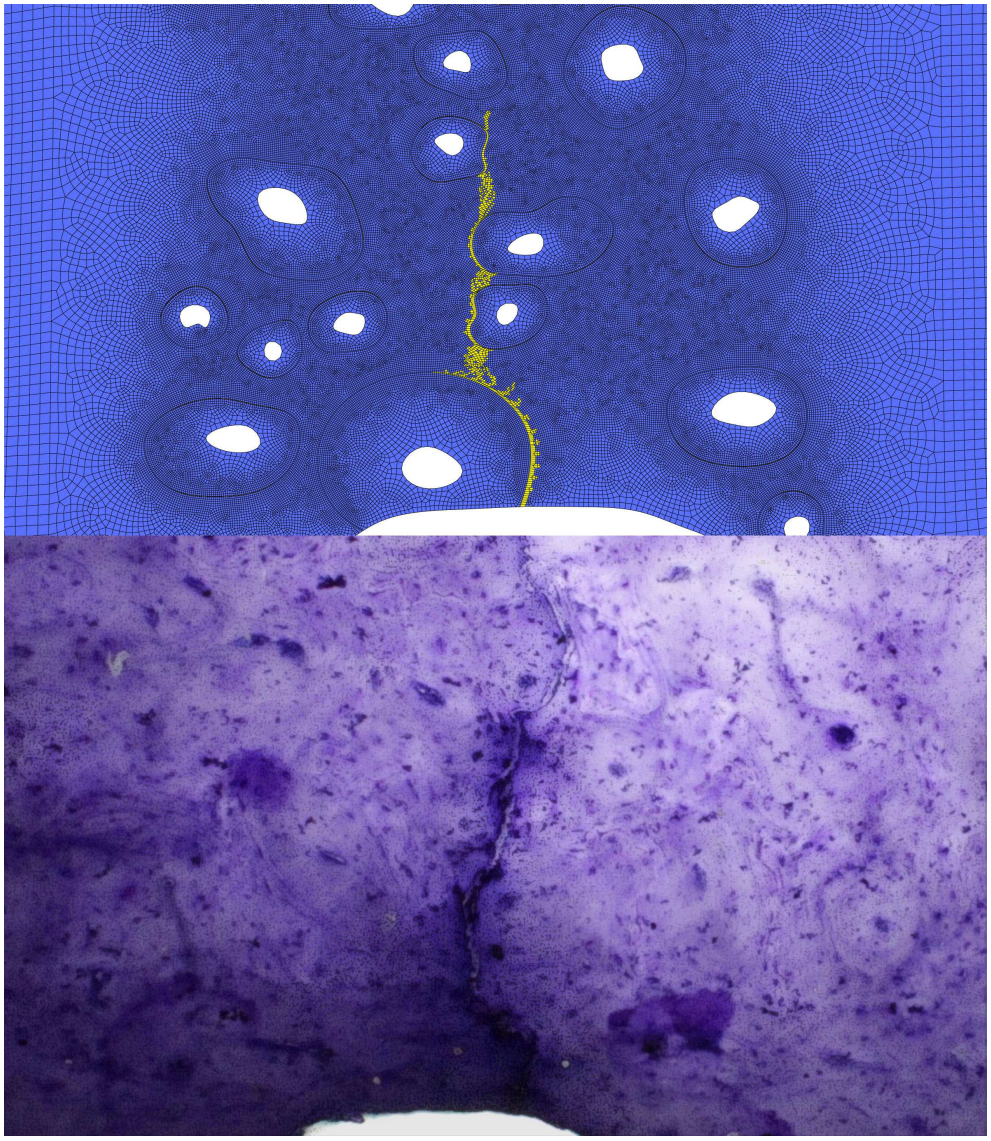

Figure 7.13: Numerical and experimental damage pattern observed at microsample 2 under a three point bending test. Damaged elements are shown in yellow.

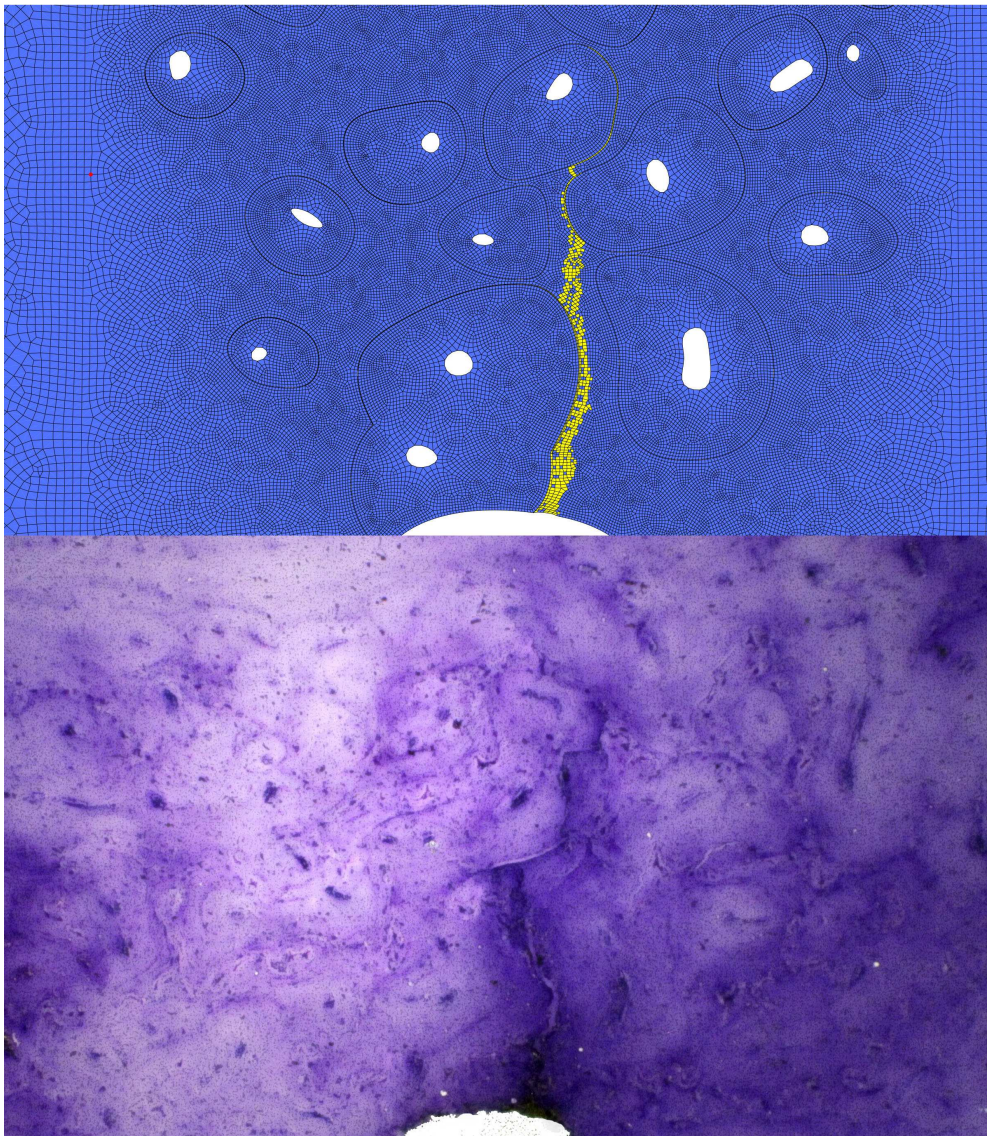

Figure 7.14: Numerical and experimental damage pattern observed at microsample 4 under a three point bending test. Damaged elements are shown in yellow.

Chapter 8

Numerical 3D model

In the last two chapters, 2D models of cortical bone with good agreement with respect to experimental evidence where developed. The aim of this Chapter is to apply the same methodology and validate damage 3D models with realistic geometries based on experimental tests from bibliography (Ebacher *et al.* [2012, 2007]; Ebacher and Wang [2009]). Three-dimensional modeling of bone microstructure is a useful tool for predicting the anisotropic mechanical behavior and its study can lead to interesting applications in multi-scale models for the improvement of fracture prevention and treatment. The damage implementation at small hierarchical levels is also an interesting research field for numerical methods looking for less computational cost in complicated geometry cases such as predicting failure from μCT scans (Verhulp *et al.* [2008]) or reproducing X-Ray synchrotron tests Gupta *et al.* [2013].

8.1 Realistic geometry based on micrographs

In previous chapters we have seen relevant models from bibliography (Ascenzi *et al.* [2013]; Li *et al.* [2013]; Nobakhti *et al.* [2014]; Aoubiza *et al.* [1996] among others) that have approached to cortical bone modeling at cortical microstructural level where

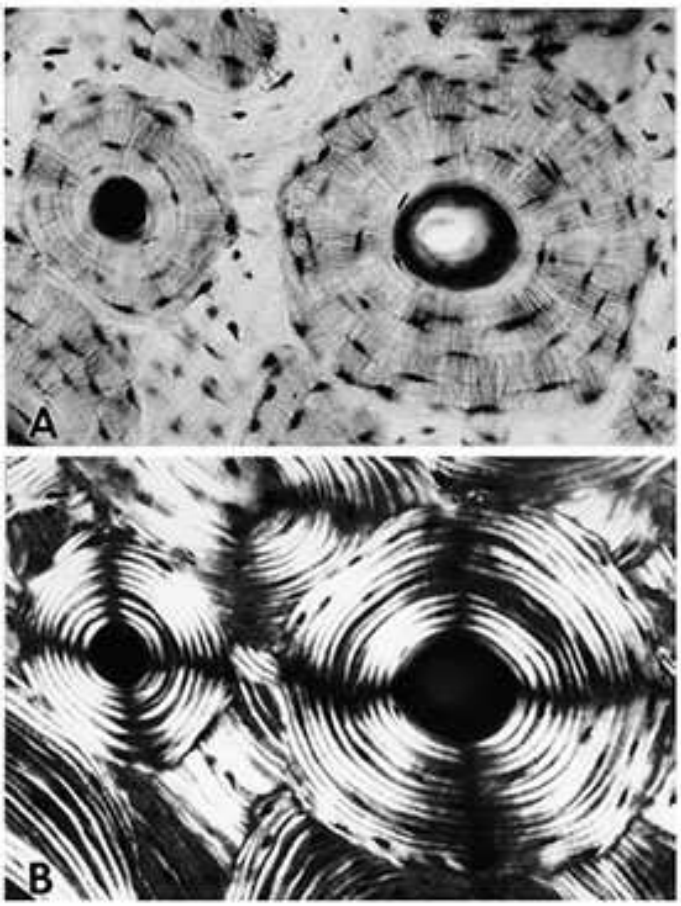

Figure 8.1: Micrographs used as references to be modeled by FE. Cross section of cortical bone showing osteons with their lacunae, canaliculi and Haversian canals by Royce *et al.* (Cowin [2001]). The bottom image corresponds to a polarized light micrograph of the same region.

model simplifications as geometry and constitutive properties are evident. Therefore, from validated damage models of previous chapters and publications (Vercher *et al.* [2014]; Vercher-Martínez *et al.* [2015]; Giner *et al.* [2014]), we proceed to the implementation of a three-dimensional model where damage propagation can be analyzed, something that can be practically unapproachable with other methods such as the X-FEM or node-release technique due to the unaffordable computational cost and time required in setting up the model Giner *et al.* [2009].

In the procedure to obtain realistic geometry models of cortical bone it is essential to have experimental results to validate and compare with, although the complexity of the heterogeneous tissues, details at such small scales and variability of parameters even in the sample treatment makes characterization a complicated procedure typical of biologic materials. In a first approach of this Thesis, we have started with a reference from the micrographs of Fig. 8.1 reported by Cowin [2001]; Steinmann *et al.* [2002] from a cortical bone sample where the distinction of different lamellae is clear under polarized light.

The procedure for obtaining the geometry of the model shown in Fig. 8.1 is similar to the one explained in Section 7.2 for the three point bending test of the ovine sample, although with different size and details of thin and thick lamellae. The topology of meshes for osteons and cement lines is structured with solid linear elements with 8 nodes. These were generated in Matlab following the osteon contours. The mesh for the interstitial part is non-structured and composed of linear square and triangular-based prismatic elements with 8 and 6 nodes respectively (C3D8 and C3D6 in Abaqus) and it is also extruded in Matlab with material and element type assignation.

Here we analyze two compression cases in both radial and longitudinal direction of the osteon (Fig. 8.2). For both cases, the distributed pressure is p=100 MPa with the aim of having a very advanced state of damage.

8.1.1 Radial compression

This type of load-case was experimentally analyzed by Ascenzi *et al*. in order to see the influence of alternate orientations of lamellae in the mechanical behavior of the osteon.

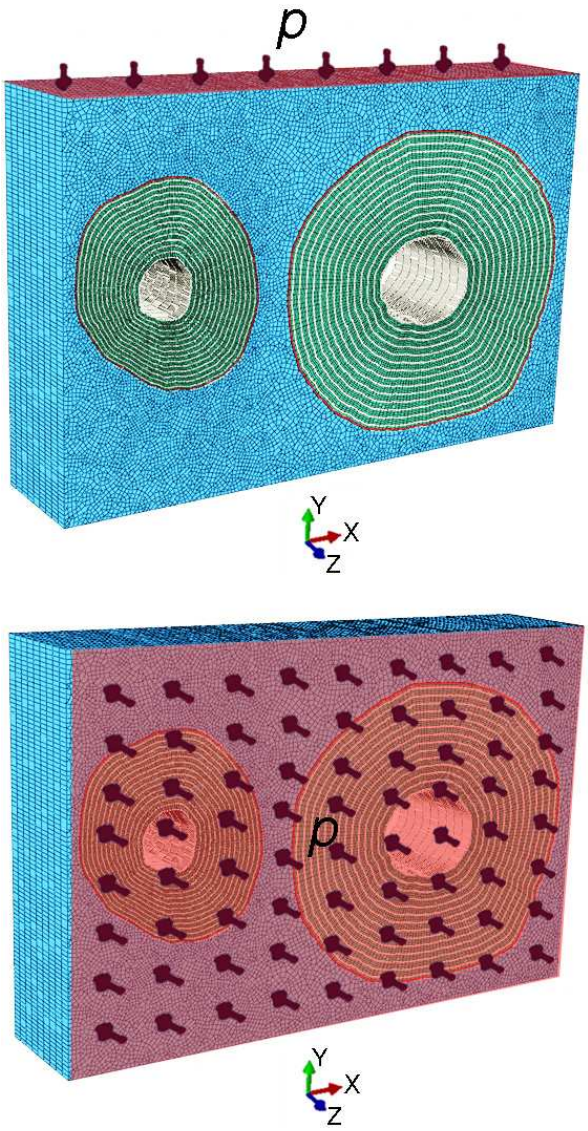

Figure 8.2: FE meshes composed of osteons, interstitial tissue and cement lines. Top: radial compression test. Bottom: axial compression test.

In Giner *et al.* [2014] it was observed that interlaminar stresses govern the damage phenomenon in an isolated osteon and that thick lamellae were the most affected for that load-case. The zones of concentrated damage are between 20° and 50° from the line of application of load. It is expected in this work that a more complex model with more entities than a single osteon will lead to a different damage pattern influenced by the composition, mechanical properties and the consideration of interstitial tissue and cement lines.

In Cowin [2001] some works related with experimental damage are discussed, and as a result we can see that the magnitude of crack density is variable in bibliography. Approximately a half of the studies indicate that cracks in vivo are observed at interstitial tissue and only a small portion correspond to those that penetrate osteons. That is attributed to the increase of mineral content at interstitial tissue that is supposed to contribute to a more fragile behavior. In Fig. 7.1 there is a micrograph of a microcrack located in interstitial bone but part of it is found on the perimeter of a cement line surrounding a Haversian system (Taylor *et al.* [2007]; O'Brien *et al.* [2003]).

8.1.2 Axial compression

The axial direction of the osteons in the model corresponds with the longitudinal axis of bone (see Fig. 8.2). There are some experimental works for the analysis of this type of load (Cowin [2001]; Ascenzi *et al.* [1973]; Ebacher *et al.* [2012]) and there is evidence of a damage pattern where the initiation is located between 30° and 35° from longitudinal axis.

8.1.3 Damage model

The procedure for damage implementation with elastic properties degradation is the same as the followed in the previous models from sections 6.6.1 and 7.3 only with the addition of out of plane stresses to failure criteria evaluation. The relatively simplicity of implementing this damage technique in a three-dimensional model is a very good advantage of this tool.

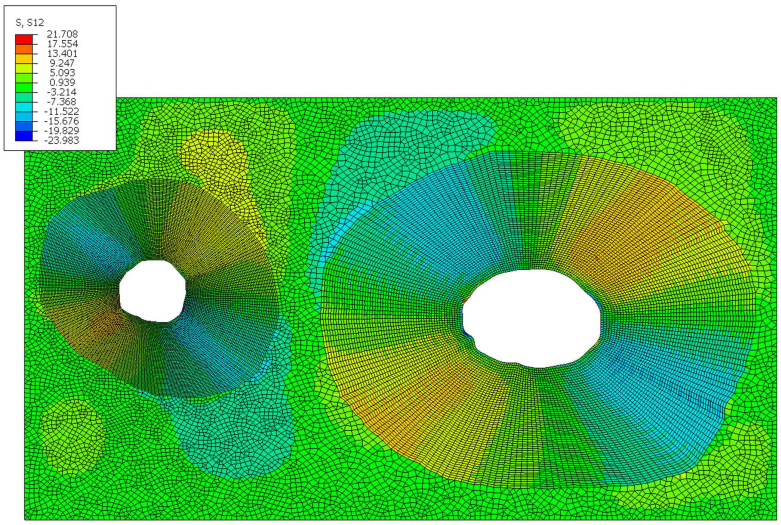

Figure 8.3: Shear stress distribution at the beginning of damage in the radial compression test.

By including in the model the interstitial tissue and cement line in addition to the realistic geometry of osteons, is interesting to notice that even though the stress distribution inside osteons is the same that the isolated case of Section 6.4, damage starts before. This is due to the contribution to the failure criteria of shear stresses in the cement line and it propagates initially through interstitial tissue (see Figs. 8.3 and 6.7).

At the bottom-right side of Fig. 8.5 we can see the distribution of shear σ_{23} stresses that can lead to a pullout of the osteons (Hiller *et al.* [2003]) under strength properties that were analyzed by Ascenzi and Bonucci [1972].

In Figs. 8.3 and 8.5 we can see the stress distribution at the onset of damage initiation for both load cases of Fig. 8.2. Stresses are referred to the coordinate system of Fig. 8.2. The patterns agree with bibliography (Cowin [2001]) but differ and provide new stress distributions in osteons due to the anisotropy of the material that is considered in this work and not in previous ones. It is important to remark that in both cases, the highest stresses and therefore damage initiation are located at cement lines and propagation is mostly through the interstitial tissue. The osteon is only affected in

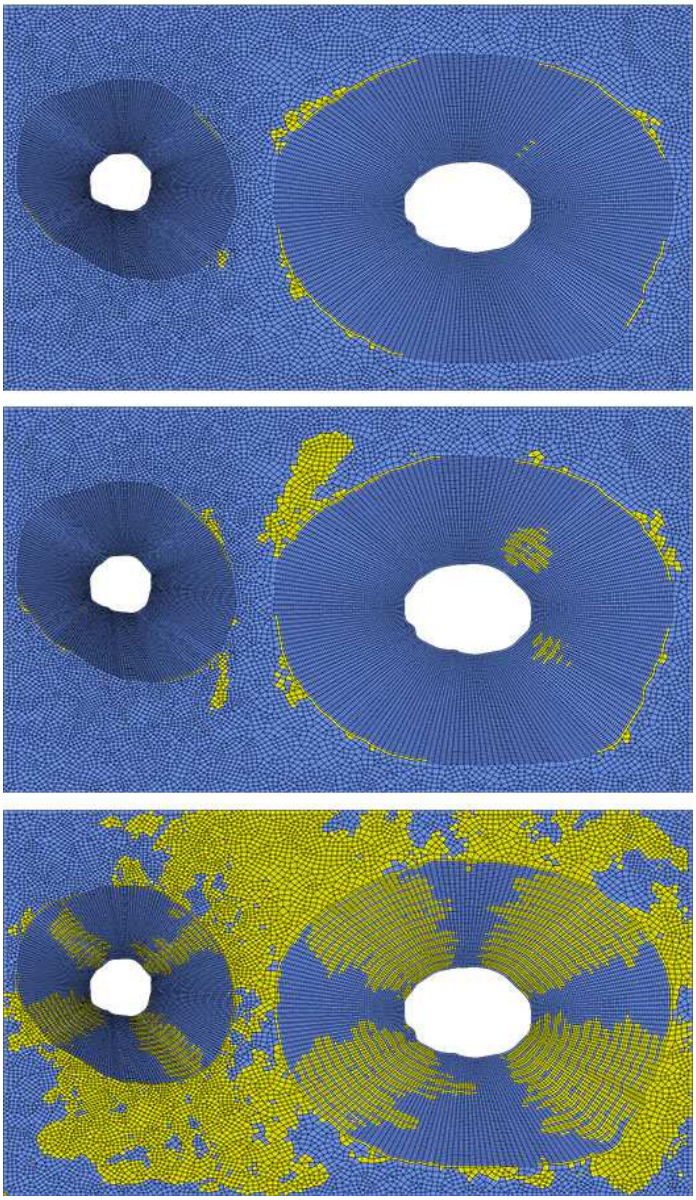

Figure 8.4: Damage sequence for radial compression loading. Damaged elements are in light color. Note damage starting at cement line.

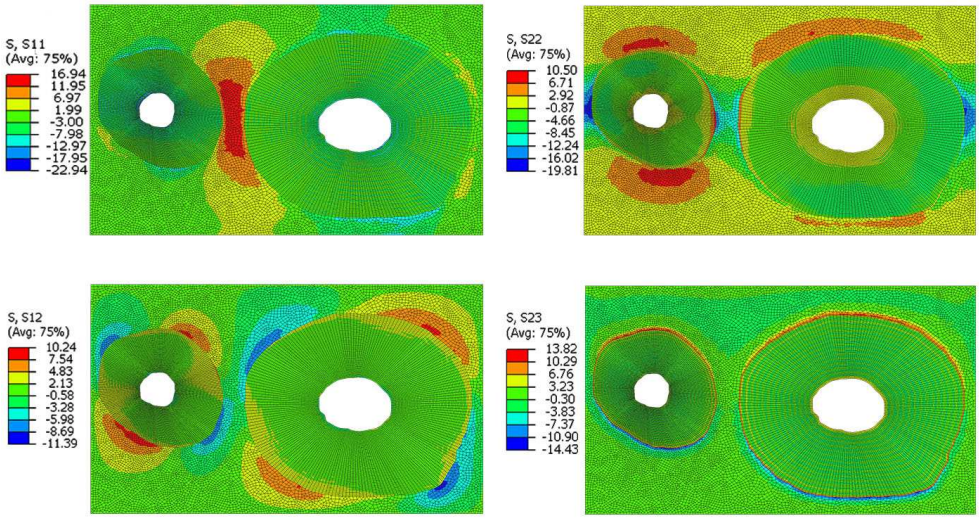

Figure 8.5: Stress distribution at the beginning of damage in the axial compression test. From left to right: top: σ_{zz}, σ_{yy}. Bottom: σ_{xy}, σ_{yz}.

some thick lamellae for the radial compression load case. Figs. 8.4 and 8.6 show a sequence of damage patterns for both, axial and radial compression cases. Fig. 8.7 shows perspective views of the advanced damage stage of both three-dimensional models. Again the damage at cement line and the surrounding tissue is observed.

8.1.4 Detailed geometry

In order to model the interstitial tissue in a more realistic way (as lamellar structure) and to compare it with the growth of cracks in experimental tests, micrographs from Ebacher *et al.* [2012, 2007]; Ebacher and Wang [2009] have been used as reference to evaluate the damage propagation under a compression test in a three-dimensional model where elastic properties and damage parameters have been adjusted in previous sections.

The realistic geometry meshes have been generated firstly from node coordinates through the software Plot Digitizer and generated in Abaqus with scripts in Python for

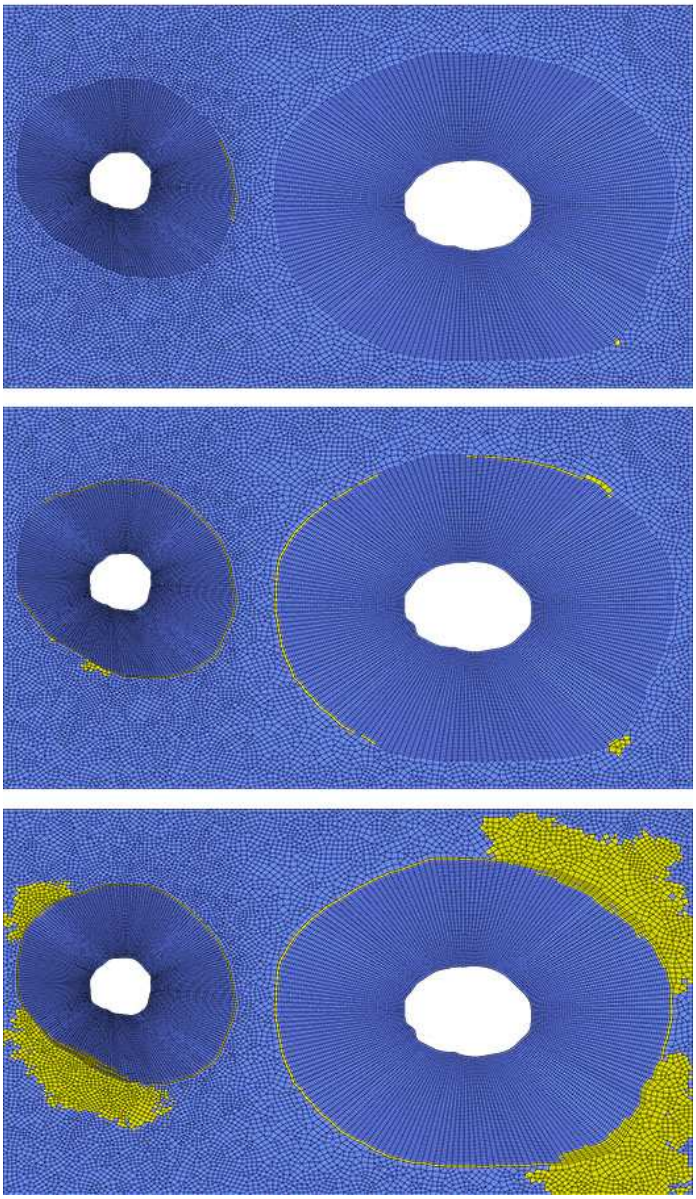

Figure 8.6: Damage sequence for axial compression loading. Damaged elements are in yellow. Note damage starting at cement line.

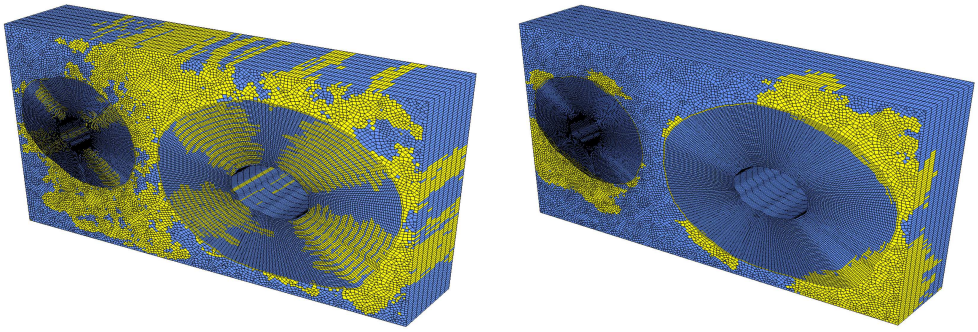

Figure 8.7: Damage patterns for an advanced state of loading. Left: radial compression. Right: axial compression. Damaged elements are in yellow.

model creation. In this 3D model we can predict the failure propagation in interstitial zone. To get these results is extremely relevant the influence of tissue orientation and the anisotropic behaviour of the material.

In Fig. 8.10 the resulting damage pattern with the realistic geometry model of Fig. 8.8 is shown. A good agreement with the experimental damage patterns is found with the numerical model. Since this model is much more realistic, we can observe the damage propagation in the interstitial tissue that has been defined as a lamellar structure with anisotropic properties.

Continuing with the simulations based on V. Ebacher *et al*. micrographs, in Ebacher *et al.* [2007] a study of strain redistribution and cracking behaviour of human bone during bending is performed. Epi-fluorescence images of the microdamage patterns after tests are shown. In order to model a sample with a different orientation of osteons from previous analysis, we have reproduced specifically the compression surface of a longitudinal section of cortical bone showing cross-hatching microdamage in the region of the sample subjected to the maximum bending moment of the standard beam specimens (Fig. 8.11).

From Fig. 8.11 we can notice diffuse microcracks developed in interstitial bone. They do not extend to the lamellae of neighboring osteons. The resulting cross-hatching pattern of the model is again in good agreement with the epi-fluorescence micrograph in the principal orientations of damage letting us to conclude that the damage in

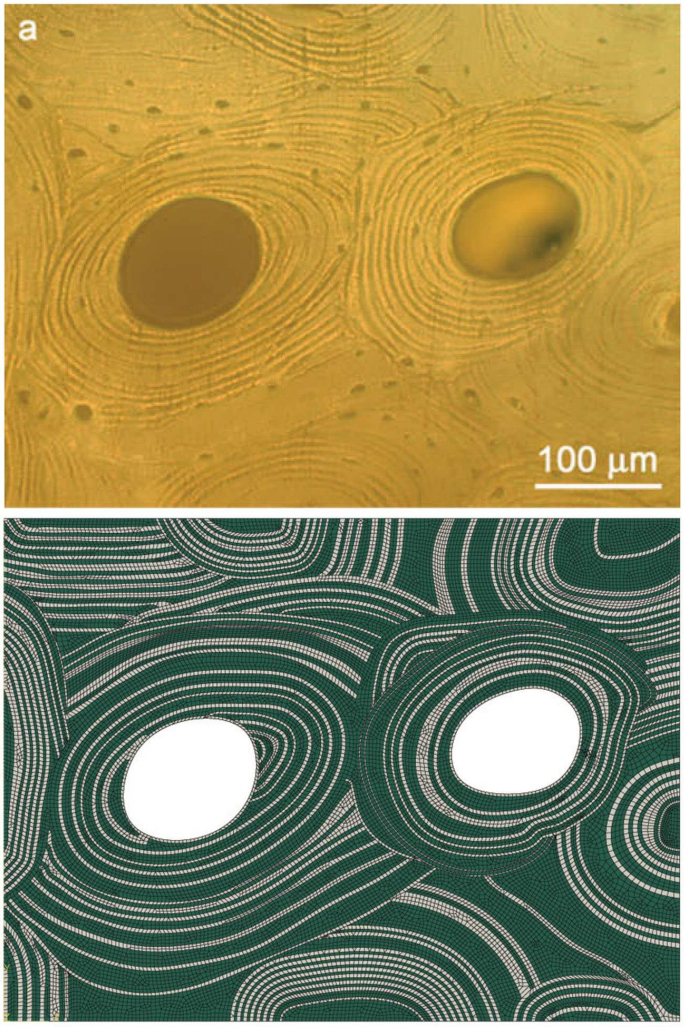

Figure 8.8: Realistic FE mesh in Abaqus (bottom) of the cortical bone micrograph with two osteons by Ebacher and Wang [2009] (top). The clear and dark colors show thick and thin lamellae.

Figure 8.9: 3D FE mesh of the cortical bone micrograph with two osteons by Ebacher and Wang [2009]. The clear and dark colors show thick and thin lamellae.

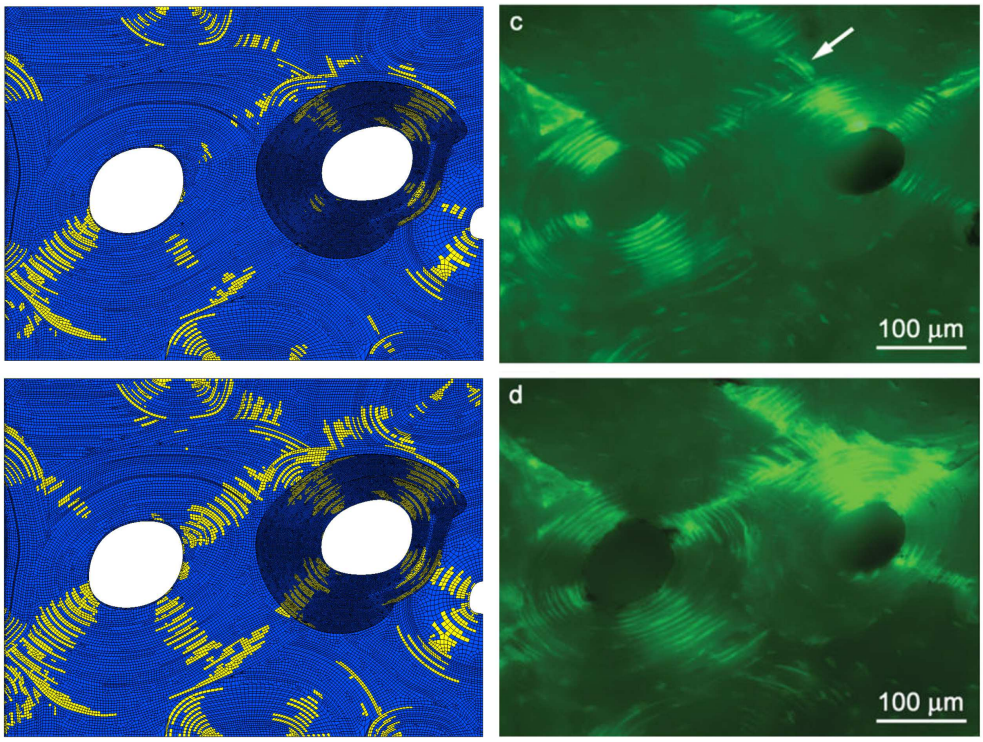

Figure 8.10: FE resulting pattern with damaged elements in light color (left) and epi-fluorescence (rigth) damage patterns of two osteons and interstitial tissue after a compression test by Ebacher and Wang [2009].

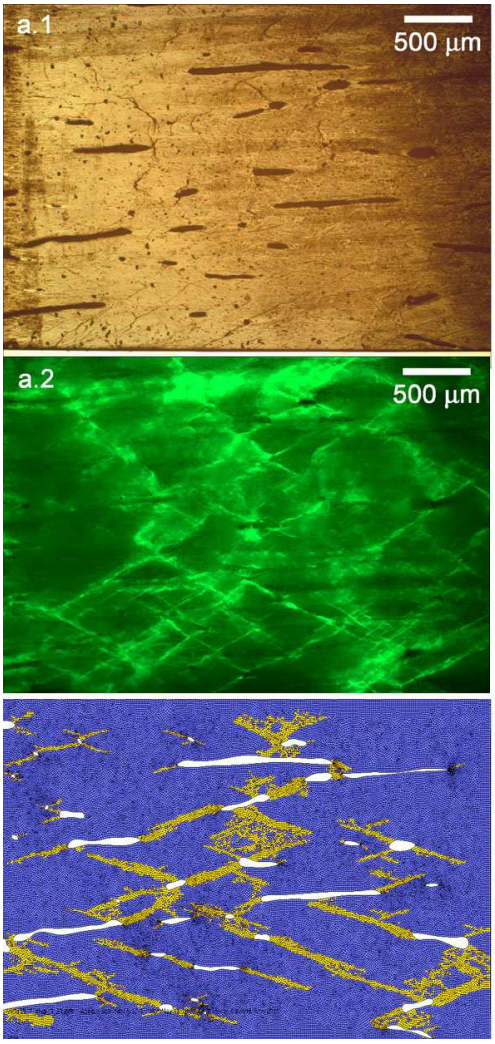

Figure 8.11: Top and middle: Microdamage morphologies under bright field (top) and epi-fluorescence (middle) modes in a compression surface showing cross-hatching microdamage by Ebacher *et al.* [2007], followed (bottom) by the damage pattern (in yellow) obtained in this Thesis by a FE model.

cortical bone at different load cases is mainly governed by shearing stresses under compression, which eventually leads to the delamination of osteons mainly starting at cement lines.

Chapter 9

Conclusions

- In this work a monoclinic homogenized stiffness tensor of mineralized collagen fibril is numerically obtained, where a staggered arrangement of crystals is supposed in fibril axial direction and parallel layers of crystals are considered in transverse fibril direction. This model at sub-micro scale is based on the observation of previous investigators.
- Homogenized stiffness tensor of lamellar bone is calculated using the same scheme that for mineralized collagen fibril. With the numerical model proposed in this work it is very easy to calculate the stiffness tensor when layer thickness and orientations change in different sublamellae of the same osteon. This procedure can also been used for other composite materials.
- From the elastic properties calculation models of Chapter 3 we can conclude that careful attention must be paid if Halpin–Tsai equations are used to estimate the elastic constants of the mineralized collagen fibril. This is because not all possible dimensions of the crystal included in the ranges reported by Rubin *et al.* [2003] lead to a positive definite stiffness matrix when using Halpin–Tsai equations with typical constituent properties, as those provided by Akiva *et al.* [1998].
- In this work, the 5–layer lamellar structure proposed by Weiner *et al.* [1999] has been also considered because it is in good agreement with the experimental

results, following Reisinger *et al.* [2011]. Since fibrils rotate in adjacent layers, the stiffness matrix exhibits an anisotropic behavior whose constants have been calculated. The elastic constants of lamellar bone calculated in this work can be compared with values reported in the literature. Elastic constants for cortical bone of Cowin are cited in Franzoso and Zysset [2009] and are summarized in Vercher *et al.* [2014].

In this work, a high influence of rotation angles ψ_1 and ψ_2 on the elastic constants estimation of lamellar bone has also been shown. This study makes it possible to calculate the 3D stiffness matrix of the lamellar bone using the proposed numerical model, considering different rotation angles of the crystals in successive layers and different layer thicknesses.

- In this work, unknown strength properties for cement lines and interstitial tissue are obtained from suggested relationships of fracture mechanics with reported data of specific fracture energies for osteons.
- Several finite element models with application of progressive damage through degradation of material properties have been proposed for cortical bone, having into account realistic geometries that have been modeled accurately. The damage patterns have been compared with experimental results of epi-fluorescence micrographs available in bibliography. The obtained damage patterns have been validated with the reference tests from other authors and we can conclude that shear stress states are the most relevant for microdamage triggering and crack propagation in lamellar structures. The applied methodology of progressive damage through FE user subroutines enables us to obtain satisfactory results of damage pattern prediction in anisotropic materials with a low computational cost compared with explicit crack models as XFEM. This makes feasible its application to three-dimensional models without increasing the complexity of subroutines.
- The damage method based on degradation of material properties implemented in this work using finite elements has proved to be a useful approach for microstructural models with realistic geometries. It makes it possible to analyze damage patterns in numerical models with less complexity than explicit crack methods. This method is useful for analyzing the mechanical behavior of the cortical bone microstructure and can be used as a practical tool for studying the failure patterns under different stress states.
- For the quasi-static models of radial compression of osteons analyzed in this work, the damage initiates at cement lines and tends to propagate through the interstitial tissue, being the osteon the last region in cortical bone that shows

concentrated damage zones. This is in agreement with literature evidencing that damage propagation in interstitial tissue is a mechanism of protection of the osteon (the basic structural unit containing the osteocytes). In these analyses is also relevant that thin lamellae inside osteons (with most fibrils aligned in the circumferential direction of the osteon) are the least affected and reach the failure when thick lamellae are in a very advanced stage of damage.

- For compression load zones in cortical bone, failure is mostly dominated by shear stresses. This is evidenced in diametral transversal sections of osteons (Figs. 8.7, 8.10) and for longitudinal sections with several osteons as well (Fig. 8.11). The finite element results presented in this work show the characteristic cross-hatched patterns that are in good agreement with epi-fluorescence images reported in the literature (Ebacher *et al.* [2007]; Ebacher and Wang [2009]).

Bibliography

U. Akiva, H. D. Wagner, and S. Weiner. Modelling the three–dimensional elastic constants of parallel–fibred and lamellar bone. *Journal of Materials Science*, 33(6):1497–1509, 1998.

O. Akkus. Elastic Deformation of Mineralized Collagen Fibrils: An Equivalent Inclusion Based Composite Model. *Journal of Biomechanical Engineering*, 127(3):383, jan 2005.

B. Aoubiza, J.M. Crolet, and A. Meunier. On the mechanical characterization of compact bone structure using the homogenization theory. *Journal of Biomechanics*, 29(12):1539–1547, dec 1996.

A. Ascenzi and E. Bonucci. The tensile properties of single osteons. *The Anatomical Record*, 158(4):375–386, aug 1967.

A. Ascenzi and E. Bonucci. The compressive properties of single osteons. *The Anatomical Record*, 161(3):377–391, jul 1968.

A. Ascenzi and E. Bonucci. The shearing properties of single osteons. *The Anatomical Record*, 172(3):499–510, mar 1972.

M-G. Ascenzi and A. Lomovtsev. Collagen orientation patterns in human secondary osteons, quantified in the radial direction by confocal microscopy. *Journal of Structural Biology*, 153(1):14–30, jan 2006.

A. Ascenzi, E. Bonucci, and A. Simkin. An approach to the mechanical properties of single osteonic lamellae. *Journal of Biomechanics*, 6(3):227–235, may 1973.

M-G. Ascenzi, M. Andreuzzi, and J.M. Kabo. Mathematical modeling of human secondary osteons. *Scanning*, 26(1):25–35, 2004.

M-G. Ascenzi, J. Gill, and A. Lomovtsev. Orientation of collagen at the osteocyte lacunae in human secondary osteons. *Journal of Biomechanics*, 41(16):3426–3435, dec 2008.

M-G. Ascenzi, N.P. Kawas, A. Lutz, D. Kardas, U. Nackenhorst, and J.H. Keyak. Individual-specific multi-scale finite element simulation of cortical bone of human proximal femur. *Journal of Computational Physics*, 244:298–311, jul 2013.

A. Ascenzi. The Micromechanics Versus the Macromechanics of Cortical Bone-A Comprehensive Presentation. *Journal of Biomechanical Engineering*, 110(4):357, 1988.

R.B. Ashman, S.C. Cowin, W.C. Van Buskirk, and J.C. Rice. A continuous wave technique for the measurement of the elastic properties of cortical bone. *Journal of Biomechanics*, 17(5):349–361, jan 1984.

S.D. Bain, T.M. Impeduglia, and C.T. Rubin. Cement Line Staining in Undecalcified Thin Sections of Cortical Bone. *Biotechnic & Histochemistry*, 65(4):159–163, jan 1990.

B. Bar-On and H.D. Wagner. Structural motifs and elastic properties of hierarchical biological tissues - A review. *Journal of Structural Biology*, 183(2):149–164, aug 2013.

B. Bar-On and H.D. Wagner. The emergence of an unusual stiffness profile in hierarchical biological tissues. *Acta Biomaterialia*, 9(9):8099–8109, sep 2013.

A. Barkaoui, A. Chamekh, T. Merzouki, R. Hambli, and A. Mkaddem. Multiscale approach including microfibril scale to assess elastic constants of cortical bone based on neural network computation and homogenization method. *International Journal for Numerical Methods in Biomedical Engineering*, 30(1):318–338, 2014.

Z.P. Bažant. Concrete fracture models: testing and practice. *Engineering Fracture Mechanics*, 69(2):165–205, jan 2002.

W. Bonfield and C.H. Li. Anisotropy of nonelastic flow in bone. *Journal of Applied Physics*, 38(6):2450, 1967.

J.C. Brewer and P.A. Lagace. Quadratic Stress Criterion for Initiation of Delamination. *Journal of Composite Materials*, 22(12):1141–1155, jan 1988.

E. Budyn and T. Hoc. Multiple scale modeling for cortical bone fracture in tension using X-FEM. *Revue européenne de mécanique numérique*, 16(2):213–236, mar 2007.

E. Budyn, T. Hoc, and J. Jonvaux. Fracture strength assessment and aging signs detection in human cortical bone using an X-FEM multiple scale approach. *Computational Mechanics*, 42(4):579–591, sep 2008.

K.J. Bundy. Determination of mineral-organic bonding effectiveness in bone-theoretical considerations. *Annals of Biomedical Engineering*, 13(2):119–135, mar 1985.

D.B. Burr, M.B. Schaffler, and R.G. Frederickson. Composition of the cement line and its possible mechanical role as a local interface in human compact bone. *Journal of Biomechanics*, 21(11):939–945, jan 1988.

B. Busse, M. Hahn, M. Soltau, J. Zustin, K. Püschel, G.N. Duda, and M. Amling. Increased calcium content and inhomogeneity of mineralization render bone toughness in osteoporosis: Mineralization, morphology and biomechanics of human single trabeculae. *Bone*, 45(6):1034–1043, dec 2009.

P.P. Camanho and F.L. Matthews. A Progressive Damage Model for Mechanically Fastened Joints in Composite Laminates. *Journal of Composite Materials*, 33(24):2248–2280, dec 1999.

K.S. Chan and D.P. Nicolella. Micromechanical modeling of R-curve behaviors in human cortical bone. *Journal of the Mechanical Behavior of Biomedical Materials*, 16:136–152, dec 2012.

F-K. Chang and K-Y. Chang. A Progressive Damage Model for Laminated Composites Containing Stress Concentrations. *Journal of Composite Materials*, 21(9):834–855, jan 1987.

K-Y. Chang, S. Llu, and F-K. Chang. Damage Tolerance of Laminated Composites Containing an Open Hole and Subjected to Tensile Loadings. *Journal of Composite Materials*, 25(3):274–301, mar 1991.

S.C. Cowin and W.C. Van Buskirk. Thermodynamic restrictions on the elastic constants of bone. *Journal of Biomechanics*, 19(1):85–87, jan 1986.

S.C. Cowin, L. Moss-Salentijn, and M.L. Moss. Candidates for the mechanosensory system in bone. *Journal of Biomechanical Engineering*, 113(2):191, may 1991.

Stephen C. Cowin. *Bone Mechanics Handbook, Second Edition*. CRC Press, Boca Raton, Fla, 2001.

B.N. Cox and Q. Yang. Cohesive zone models of localization and fracture in bone. *Engineering Fracture Mechanics*, 74(7):1079–1092, may 2007.

L.G.E. Cox, B. van Rietbergen, C.C. van Donkelaar, and K. Ito. Analysis of bone architecture sensitivity for changes in mechanical loading, cellular activity, mechanotransduction, and tissue properties. *Biomechanics and Modeling in Mechanobiology*, 10(5):701–712, oct 2011.

J.D. Currey. Strength of Bone. *Nature*, 195(4840):513–514, aug 1962.

S. Cusack and A. Miller. Determination of the elastic constants of collagen by Brillouin light scattering. *Journal of Molecular Biology*, 135(1):39–51, 1979.

I.M. Daniel. Failure of Composite Materials. *Strain*, 43(1):4–12, feb 2007.

A. Dasgupta and S.M. Bhandarkar. A generalized self-consistent Mori-Tanaka scheme for fiber-composites with multiple interphases. *Mechanics of Materials*, 14(1):67–82, nov 1992.

J.E. Davies. Bone bonding at natural and biomaterial surfaces. *Biomaterials*, 28(34):5058–5067, dec 2007.

X.N. Dong and X.E. Guo. Prediction of Cortical Bone Elastic Constants by a Two-Level Micromechanical Model Using a Generalized Self-Consistent Method. *Journal of Biomechanical Engineering*, 128(3):309, jun 2006.

V. Ebacher and R. Wang. A unique microcracking process associated with the inelastic deformation of haversian bone. *Advanced Functional Materials*, 19(1):57–66, jan 2009.

V. Ebacher, C. Tang, H. McKay, T.R. Oxland, P. Guy, and R. Wang. Strain redistribution and cracking behavior of human bone during bending. *Bone*, 40(5):1265–1275, 2007.

V. Ebacher, P. Guy, T.R. Oxland, and R. Wang. Sub-lamellar microcracking and roles of canaliculi in human cortical bone. *Acta Biomaterialia*, 8(3):1093–1100, mar 2012.

D. Erts, L.J. Gathercole, and E.D.T. Atkins. Scanning probe microscopy of intrafibrillar crystallites in calcified collagen. *Journal of Materials Science: Materials in Medicine*, 5(4):200–206, apr 1994.

A. Faingold, S.R. Cohen, and H.D. Wagner. Nanoindentation of osteonal bone lamellae. *Journal of the Mechanical Behavior of Biomedical Materials*, 9:198–206, may 2012.

H.T. Fawns and J.W. Landells. Histochemical Studies of Rheumatic Conditions: I. Observations on the Fine Structures of the Matrix of Normal Bone and Cartilage. *Annals of the Rheumatic Diseases*, 12(2):105–113, jun 1953.

G. Franzoso and P.K. Zysset. Elastic Anisotropy of Human Cortical Bone Secondary Osteons Measured by Nanoindentation. *Journal of Biomechanical Engineering*, 131(2):021001, dec 2009.

P. Frasca, R. Harper, and J.L. Katz. Strain and frequency dependence of shear storage modulus for human single osteons and cortical bone microsamples-Size and hydration effects. *Journal of Biomechanics*, 14(10):679–690, jan 1981.

H. Gao, B. Ji, I.L. Jager, E. Arzt, and P. Fratzl. Materials become insensitive to flaws at nanoscale: Lessons from nature. *Proceedings of the National Academy of Sciences*, 100(10):5597–5600, may 2003.

W. Gebhardt. Über funktionell wichtige Anordnungsweisen der feineren und gröberen Bauelemente des Wirbeltierknochens. *Archiv für Entwicklungsmechanik der Organismen*, 20(2):187–322, nov 1905.

E. Giner, N. Sukumar, J.E. Tarancón, and F.J. Fuenmayor. An Abaqus implementation of the extended finite element method. *Engineering Fracture Mechanics*, 76(3):347–368, feb 2009.

E. Giner, C. Arango, A. Vercher, and F.J. Fuenmayor. Numerical modelling of the mechanical behaviour of an osteon with microcracks. *Journal of the Mechanical Behavior of Biomedical Materials*, 37:109–124, sep 2014.

M.M. Giraud-Guille. Twisted plywood architecture of collagen fibrils in human compact bone osteons. *Calcified Tissue International*, 42(3):167–180, may 1988.

H.S. Gupta and P. Zioupos. Fracture of bone tissue: The 'hows' and the 'whys'. *Medical Engineering & Physics*, 30(10):1209–1226, dec 2008.

H.S. Gupta, J. Seto, W. Wagermaier, P. Zaslansky, P. Boesecke, and P. Fratzl. Cooperative deformation of mineral and collagen in bone at the nanoscale. *Proceedings of the National Academy of Sciences*, 103(47):17741–17746, nov 2006.

H.S. Gupta, S. Krauss, M. Kerschnitzki, A. Karunaratne, J.W.C. Dunlop, H. Barber, P. Boesecke, S.S. Funari, and P. Fratzl. Intrafibrillar plasticity through mineral/collagen sliding is the dominant mechanism for the extreme toughness of antler bone. *Journal of the mechanical behavior of biomedical materials*, 28:366–82, dec 2013.

M.E. Gurtin. The Linear Theory of Elasticity. In C Truesdell, editor, *Linear Theories of Elasticity and Thermoelasticity*, pages 1–295. Springer Berlin Heidelberg, Berlin, Heidelberg, 1973.

S.K. Ha, K.K. Jin, and Y. Huang. Micro-Mechanics of Failure (MMF) for Continuous Fiber Reinforced Composites. *Journal of Composite Materials*, 42(18):1873–1895, sep 2008.

J.C. Halpin. *Primer on composite materials analysis*. Technomic Pub. Co., Lancaster, Pa., 1984.

J.C. Halpin. *Primer on Composite Materials Analysis, Second Edition (revised)*. Taylor & Francis, 1992.

R. Hambli, A. Bettamer, and S. Allaoui. Finite element prediction of proximal femur fracture pattern based on orthotropic behaviour law coupled to quasi-brittle damage. *Medical Engineering & Physics*, 34(2):202–210, mar 2012.

R. Hambli. Micro-CT finite element model and experimental validation of trabecular bone damage and fracture. *Bone*, 56(2):363–374, oct 2013.

Z. Hashin and A. Rotem. A Fatigue Failure Criterion for Fiber Reinforced Materials. *Journal of Composite Materials*, 7(4):448–464, oct 1973.

L.P. Hiller, S.M. Stover, V.A. Gibson, J.C. Gibeling, C.S. Prater, S.J. Hazelwood, O.C. Yeh, and R.B. Martin. Osteon pullout in the equine third metacarpal bone: Effects of ex vivo fatigue. *Journal of Orthopaedic Research*, 21(3):481–488, may 2003.

H.A. Hogan. Micromechanics modeling of Haversian cortical bone properties. *Journal of Biomechanics*, 25(5):549–556, may 1992.

J. Hohe. A direct homogenisation approach for determination of the stiffness matrix for microheterogeneous plates with application to sandwich panels. *Composites Part B: Engineering*, 34(7):615–626, oct 2003.

J.P. Hou, N. Petrinic, C. Ruiz, and S.R. Hallett. Prediction of impact damage in composite plates. *Composites Science and Technology*, 60(2):273–281, feb 2000.

D.J. Hulmes, T.J. Wess, D.J. Prockop, and P. Fratzl. Radial packing, order, and disorder in collagen fibrils. *Biophysical Journal*, 68(5):1661–1670, may 1995.

I. Ichim, Q. Li, W. Li, M.V. Swain, and J. Kieser. Modelling of fracture behaviour in biomaterials. *Biomaterials*, 28(7):1317–1326, mar 2007.

I. Jäger and P. Fratzl. Mineralized Collagen Fibrils: A Mechanical Model with a Staggered Arrangement of Mineral Particles. *Biophysical Journal*, 79(4):1737–1746, oct 2000.

J. Klein-Nulend, R.G. Bacabac, and A.D. Bakker. Mechanical loading and how it affects bone cells: the role of the osteocyte cytoskeleton in maintaining our skeleton. *European cells & materials*, 24:278–91, jan 2012.

M.L. Knothe Tate, J.R. Adamson, A.E. Tami, and T.W. Bauer. The osteocyte. *The International Journal of Biochemistry & Cell Biology*, 36(1):1–8, jan 2004.

R.S. Lakes, J.L. Katz, and S.S. Sternstein. Viscoelastic properties of wet cortical bone-I. Torsional and biaxial studies. *Journal of Biomechanics*, 12(9):657–678, 1979.

W.J. Landis. An overview of vertebrate mineralization with emphasis on collagen-mineral interaction. *Gravitational and Space Research*, 2007.

I. Lapczyk and J.A. Hurtado. Progressive damage modeling in fiber-reinforced materials. *Composites Part A: Applied Science and Manufacturing*, 38(11):2333–2341, nov 2007.

M.E. Launey, M.J. Buehler, and R.O. Ritchie. On the Mechanistic Origins of Toughness in Bone. *Annual Review of Materials Research*, 40(1):25–53, jun 2010.

S.G. Lekhnitskii. *Of an anisotropic elastic body.* San Francisco: Holden-Day, 1963.

B.M. Lempriere. Poisson's ratio in orthotropic materials. *AIAA Journal*, 6(11):2226–2227, nov 1968.

S. Li, A. Abdel-Wahab, E. Demirci, and V.V. Silberschmidt. Fracture process in cortical bone: X-FEM analysis of microstructured models. *International Journal of Fracture*, 184(1-2):43–55, nov 2013.

J. Lusis, R.T. Woodhams, and M. Xanthos. The effect of flake aspect ratio on the flexural properties of mica reinforced plastics. *Polymer Engineering and Science*, 13(2):139–145, mar 1973.

G. Marotti and M.A. Muglia. The microscopic determinants of bone mechanical properties. *Italian Journal of Mineral & Electrolyte Metabolism*, 8(4):167–175, 1994.

G. Marotti, M. Ferretti, and C. Palumbo. The problem of bone lamellation: An attempt to explain different proposed models. *Journal of Morphology*, 274(5):543–550, 2013.

J. Martínez-Reina, J. Domínguez, and J.M. García-Aznar. Effect of porosity and mineral content on the elastic constants of cortical bone: a multiscale approach. *Biomechanics and Modeling in Mechanobiology*, 10(3):309–322, jul 2010.

J.S. Mayes and A.C. Hansen. A comparison of multicontinuum theory based failure simulation with experimental results. *Composites Science and Technology*, 64(3-4):517–527, mar 2004.

R.K. Nalla, J.H. Kinney, and R.O. Ritchie. Mechanistic fracture criteria for the failure of human cortical bone. *Nature Materials*, 2(3):164–168, mar 2003.

R.K. Nalla, J.J. Kruzic, J.H. Kinney, and R.O. Ritchie. Mechanistic aspects of fracture and R-curve behavior in human cortical bone. *Biomaterials*, 26(2):217–231, jan 2005.

D.P. Nicolella, D.E. Moravits, A.M. Gale, L.F. Bonewald, and J. Lankford. Osteocyte lacunae tissue strain in cortical bone. *Journal of Biomechanics*, 39(9):1735–1743, jan 2006.

D.P. Nicolella, Q. Ni, and K.S. Chan. Non-destructive characterization of microdamage in cortical bone using low field pulsed NMR. *Journal of the Mechanical Behavior of Biomedical Materials*, 4(3):383–391, apr 2011.

S. Nobakhti, G. Limbert, and P.J. Thurner. Cement lines and interlamellar areas in compact bone as strain amplifiers - Contributors to elasticity, fracture toughness and mechanotransduction. *Journal of the Mechanical Behavior of Biomedical Materials*, 29:235–251, jan 2014.

F.J. O'Brien, D. Taylor, and T.C. Lee. Microcrack accumulation at different intervals during fatigue testing of compact bone. *Journal of Biomechanics*, 36(7):973–980, jul 2003.

F.J. O'Brien, D. Taylor, and T.C. Lee. The effect of bone microstructure on the initiation and growth of microcracks. *Journal of Orthopaedic Research*, 23(2):475–480, mar 2005.

J.P.R.O. Orgel, A. Miller, T.C. Irving, R.F. Fischetti, A.P. Hammersley, and T.J. Wess. The In Situ Supermolecular Structure of Type I Collagen. *Structure*, 9(11):1061–1069, nov 2001.

G.E. Padawer and N. Beecher. On the strength and stiffness of planar reinforced plastic resins. *Polymer Engineering and Science*, 10(3):185–192, may 1970.

D.H. Pahr and P.K. Zysset. Influence of boundary conditions on computed apparent elastic properties of cancellous bone. *Biomechanics and Modeling in Mechanobiology*, 7(6):463–476, oct 2007.

H.C. Park and R.S. Lakes. Cosserat micromechanics of human bone: Strain redistribution by a hydration sensitive constituent. *Journal of Biomechanics*, 19(5):385–397, jan 1986.

P.J. Prendergast and R. Huiskes. Microdamage and osteocyte-lacuna strain in bone: a microstructural finite element analysis. *Journal of biomechanical engineering*, 118(2):240–6, may 1996.

A. Puck. Failure analysis of FRP laminates by means of physically based phenomenological models. *Composites Science and Technology*, 58(7):1045–1067, jul 1998.

A.G. Reisinger, D.H. Pahr, and P.K. Zysset. Sensitivity analysis and parametric study of elastic properties of an unidirectional mineralized bone fibril-array using mean field methods. *Biomechanics and Modeling in Mechanobiology*, 9(5):499–510, oct 2010.

A.G. Reisinger, D.H. Pahr, and P.K. Zysset. Elastic anisotropy of bone lamellae as a function of fibril orientation pattern. *Biomechanics and Modeling in Mechanobiology*, 10(1):67–77, feb 2011.

J.Y. Rho, T.Y. Tsui, and G.M. Pharr. Elastic properties of human cortical and trabecular lamellar bone measured by nanoindentation. *Biomaterials*, 18(20):1325–30, oct 1997.

J.Y. Rho, L. Kuhn-Spearing, and P. Zioupos. Mechanical properties and the hierarchical structure of bone. *Medical engineering & physics*, 20(2):92–102, mar 1998.

J.Y. Rho, J.D. Currey, P. Zioupos, and G.M. Pharr. The anisotropic Young's modulus of equine secondary osteones and interstitial bone determined by nanoindentation. *Journal of Experimental Biology*, 204(10):1775–1781, may 2001.

R.O. Ritchie, J.H. Kinney, J.J. Kruzic, and R.K. Nalla. A fracture mechanics and mechanistic approach to the failure of cortical bone. *Fatigue Fracture of Engineering Materials and Structures*, 28(4):345–371, apr 2005.

C. Rubin, A.S. Turner, R. Müller, E. Mittra, K. McLeod, W. Lin, and Y-X. Qin. Quantity and Quality of Trabecular Bone in the Femur Are Enhanced by a Strongly Anabolic, Noninvasive Mechanical Intervention. *Journal of Bone and Mineral Research*, 17(2):349–357, feb 2002.

M.A Rubin, I. Jasiuk, J. Taylor, J. Rubin, T. Ganey, and R.P. Apkarian. TEM analysis of the nanostructure of normal and osteoporotic human trabecular bone. *Bone*, 33(3):270–282, sep 2003.

M.B. Schaffler, K. Choi, and C. Milgrom. Aging and matrix microdamage accumulation in human compact bone. *Bone*, 17(6):521–525, dec 1995.

J.G. Skedros, J.L. Holmes, E.G. Vajda, and R.D. Bloebaum. Cement lines of secondary osteons in human bone are not mineral-deficient: New data in a historical perspective. *The Anatomical Record Part A: Discoveries in Molecular, Cellular, and Evolutionary Biology*, 286A(1):781–803, sep 2005.

B. Steinmann, P.M. Royce, and A. Superti-Furge. *Connective Tissue and Its Heritable Disorders*. John Wiley & Sons, Inc., Hoboken, NJ, USA, may 2002.

P.M. Suquet. Introduction. In *Homogenization Techniques for Composite Media*, pages 193–198. Springer Berlin Heidelberg, Berlin, Heidelberg, 1987.

Dassault Systemes. *ABAQUS/Standard User's Manual, V. 6.12*.

S.C. Tan and R.J. Nuismer. A Theory for Progressive Matrix Cracking in Composite Laminates. *Journal of Composite Materials*, 23(10):1029–1047, oct 1989.

S.C. Tan and J. Perez. Progressive Failure of Laminated Composites with a Hole under Compressive Loading. *Journal of Reinforced Plastics and Composites*, 12(10):1043–1057, oct 1993.

S.C. Tan. A Progressive Failure Model for Composite Laminates Containing Openings. *Journal of Composite Materials*, 25(5):556–577, may 1991.

T.E. Tay, V.B.C. Tan, and M. Deng. Element-failure concepts for dynamic fracture and delamination in low-velocity impact of composites. *International Journal of Solids and Structures*, 40(3):555–571, feb 2003.

T.E. Tay, G. Liu, V.B.C. Tan, X.S. Sun, and D.C. Pham. Progressive Failure Analysis of Composites. *Journal of Composite Materials*, 42(18):1921–1966, jul 2008.

T.E. Tay, M. Ridha, G. Liu, and V.B.C. Tan. Progressive Failure of Notched and Repaired Composites. *ICCM International Conferences on Composite Materials*, (Conference Paper), 2009.

D. Taylor, J.G. Hazenberg, and T.C. Lee. Living with cracks: Damage and repair in human bone. *Nature Materials*, 6(4):263–268, apr 2007.

V. Tomar. Insights into the effects of tensile and compressive loadings on microstructure dependent fracture of trabecular bone. *Engineering Fracture Mechanics*, 76(7):884–897, may 2009.

S.W. Tsai and E.M. Wu. A General Theory of Strength for Anisotropic Materials. *Journal of Composite Materials*, 5(1):58–80, jan 1971.

A. Turon, C.G. Dávila, P.P. Camanho, and J. Costa. An engineering solution for mesh size effects in the simulation of delamination using cohesive zone models. *Engineering Fracture Mechanics*, 74(10):1665–1682, jul 2007.

A. Ural and D. Vashishth. Cohesive finite element modeling of age-related toughness loss in human cortical bone. *Journal of Biomechanics*, 39(16):2974–2982, jan 2006.

A. Ural. Prediction of Colles fracture load in human radius using cohesive finite element modeling. *Journal of Biomechanics*, 42(1):22–28, jan 2009.

D. Vashishth. Hierarchy of bone microdamage at multiple length scales. *International Journal of Fatigue*, 29(6):1024–1033, jun 2007.

A. Vercher, E. Giner, C. Arango, J.E. Tarancón, and F.J. Fuenmayor. Homogenized stiffness matrices for mineralized collagen fibrils and lamellar bone using unit cell finite element models. *Biomechanics and Modeling in Mechanobiology*, 13(2):437–449, apr 2014.

A. Vercher-Martínez, E. Giner, C. Arango, and F.J. Fuenmayor. Influence of the mineral staggering on the elastic properties of the mineralized collagen fibril in lamellar bone. *Journal of the Mechanical Behavior of Biomedical Materials*, 42:243–256, feb 2015.

E. Verhulp, B. van Rietbergen, R. Müller, and R. Huiskes. Indirect determination of trabecular bone effective tissue failure properties using micro-finite element simulations. *Journal of Biomechanics*, 41(7):1479–1485, jan 2008.

W. Wagermaier, H.S. Gupta, A. Gourrier, M. Burghammer, P. Roschger, and P. Fratzl. Spiral twisting of fiber orientation inside bone lamellae. *Biointerphases*, 1(1):1, 2006.

H.D. Wagner and S. Weiner. On the relationship between the microstructure of bone and its mechanical stiffness. *Journal of Biomechanics*, 25(11):1311–1320, nov 1992.

S. Weiner and H.D. Wagner. THE MATERIAL BONE: Structure-Mechanical Function Relations. *Annual Review of Materials Science*, 28(1):271–298, aug 1998.

S. Weiner, T. Arad, and W. Traub. Crystal organization in rat bone lamellae. *FEBS Letters*, 285(1):49–54, jul 1991.

S. Weiner, W. Traub, and H.D. Wagner. Lamellar Bone: Structure-Function Relations. *Journal of Structural Biology*, 126(3):241–255, jun 1999.

Q.D. Yang, B.N. Cox, R.K. Nalla, and R.O. Ritchie. Fracture length scales in human cortical bone: The necessity of nonlinear fracture models. *Biomaterials*, 27(9):2095–2113, mar 2006.

H. Yao, L. Ouyang, and W-Y. Ching. Ab Initio Calculation of Elastic Constants of Ceramic Crystals. *Journal of the American Ceramic Society*, 90(10):3194–3204, oct 2007.

Y.J. Yoon and S.C. Cowin. The estimated elastic constants for a single bone osteonal lamella. *Biomechanics and modeling in mechanobiology*, 7(1):1–11, feb 2008.

F. Yuan, S.R. Stock, D.R. Haeffner, J.D. Almer, D.C. Dunand, and L.C Brinson. A new model to simulate the elastic properties of mineralized collagen fibril. *Biomechanics and Modeling in Mechanobiology*, 10(2):147–160, apr 2011.

P.K. Zysset, X. Edward Guo, C. Edward Hoffler, K.E. Moore, and S.A. Goldstein. Elastic modulus and hardness of cortical and trabecular bone lamellae measured by nanoindentation in the human femur. *Journal of Biomechanics*, 32(10):1005–1012, oct 1999.